이학박사학위논문

First-Principles Study of Electronic and Magnetic Properties of Perovskite-Type Metal-Organic Framework $[C(NH_2)_3]M(HCOO)_3$ (M = Cr, Cu)

페로브스카이트형 금속-유기 골격체 $[C(NH_2)_3]M(HCOO)_3$ (M = Cr, Cu)의 전기 및 자기적 특성에 대한 제일원리 계산 연구

2023년 2월

서울대학교 대학원

물리천문학부

야나노세 구니히로

First-Principles Study of Electronic and Magnetic Properties of Perovskite-Type Metal-Organic Framework $[C(NH_2)_3]M(HCOO)_3$ (M = Cr, Cu)

페로브스카이트형 금속-유기 골격체 $[C(NH_2)_3]M(HCOO)_3$ (M = Cr, Cu)의 전기 및 자기적 특성에 대한 제일원리 계산 연구

지도교수 유 재 준

이 논문을 이학박사 학위논문으로 제출함

2022년 12월

서울대학교 대학원

물리천문학부

야나노세 구니히로

야나노세구니히로의 이학박사 학위논문을 인준함

2022년 12월

위 원 장	이 탁 희	(인)
부위원장	유 재 준	(인)
위 원	민 홍 기	(인)
위 원	김 기 훈	(인)
위 원	Alessandro Stroppa	(인)

First-Principles Study of Electronic and Magnetic Properties of Perovskite-Type Metal-Organic Framework $[C(NH_2)_3]M(HCOO)_3$ (M = Cr, Cu)

by

Kunihiro Yananose

A Dissertation Submitted to the Faculty of the Graduate School of Seoul National University in Partial Fulfillment of the Requirements for the Degree of Doctor of Philosophy

December 2022

Advisory Committee:

Professor Takhee Lee, Chair
Professor Jaejun Yu, Advisor
Professor Hongki Min
Professor Kee Hoon Kim
Professor Alessandro Stroppa

Abstract

First-Principles Study of Electronic and Magnetic Properties of Perovskite-Type Metal-Organic Framework $[C(NH_2)_3]M(HCOO)_3$ (M = Cr, Cu)

Kunihiro Yananose

Department of Physics and Astronomy

The Graduate School

Seoul National University

Hybrid materials are composed of both inorganic and organic constituents, thus exhibiting the properties of both, or sometimes interplay of them. Therefore, one can expect a distinct property from conventional inorganic materials. For example, hybrid organic-inorganic perovskites have an ABX_3 perovskite structure with molecular ions at A- or X-sites. They are known as promising solar cell materials. On the other hand, metal-organic frameworks (MOFs) are crystals where organic linkers interconnect the metal ions. MOFs can adopt various types of structures, such as porous, layered, or perovskite structures. In this thesis, we are focusing on multiferroic perovskite-type MOFs metal guanidinium formates $[C(NH_2)_3]M(HCOO)_3$ (M = Cr, Cu). By means of the first-principles calculation based on the density functional theory, we investigated the multiferroic properties of $[C(NH_2)_3]M(HCOO)_3$, i.e., electronic and magnetic properties and their coupling to the structural properties. In particular, a group theoretical method is used to analyze the structural deformation. It is known that the $[C(NH_2)_3]M(HCOO)_3$ exhibits the hybrid improper ferroelectricity, where the polar mode is induced by the combination of two non-

polar modes (hybrid mode). However, we found that the hybrid mode induces a dominant purely electronic polarization in the $[C(NH_2)_3]M(HCOO)_3$. As opposed to an intuitive picture, the polar mode rather compensates for this purely electronic polarization. We provide microscopic origin and macroscopic analysis for this property. In addition, we found that the orbital magnetic moment is the dominant contribution to the total magnetic moment in the $[C(NH_2)_3]Cu(HCOO)_3$. We established the model for the orbital magnetic moment based on the perturbation theory combined with the Jahn-Teller effective Hamiltonian, thus revealing the key role of the Jahn-Teller effect.

Keywords: Density functional theory, Metal-organic framework, Electric polarization, Magnetism, Jahn-Teller effect, hybrid improper ferroelectricity, orbital magnetism

Student number: 2016-20299

Contents

List of Figures

List of Tables

1 Introduction

Beyond the traditional classification of organic and inorganic materials, a large number of hybrid materials, which are composed of both inorganic and organic constituents, have been studied in both fields of the fundamental sciences and functional applications. Hybrid materials exhibit both inorganic and organic properties, or sometimes interplay of them. Therefore, one can expect a distinct property from conventional inorganic materials.

For example, hybrid organic-inorganic perovskites (HOIPs), such as methylammonium lead iodide ($MAPbI_3$), have an ABX_3 perovskite structure with molecular ions at A- or X-sites. They are known as promising solar cell materials [1, 2]. The inclusion of a polar molecule leads to studies on their effects, for example, macroscopic polarization [3], entropy effect [4], Rashba-Dresselhaus effect [5, 6], etc.

On the other hand, metal-organic frameworks (MOFs) are materials in which the metal ions are connected with each other by organic molecules. The choice of organic linkers allows not only the variety in their crystal structure types, such as porous, layered, or perovskite structures, but also control of their length scales. One of its classes, the porous MOFs, hold a large portion of cavities in them. Their tunable porosity enables applications in gas storage, catalysis, etc., thus widely studied [7, 8]. On the other hand, dense MOFs hold much smaller cavities in comparison to porous MOFs. Instead, their cations

are closer together and can play a significant role in the emergence of their functional properties [9–11]. The combination of organic-inorganic features can induce both magnetism and ferroelectricity simultaneously, i.e., multiferroicity, which is of importance in both fundamental physics and application. In particular, a possibility of cross-control of magnetic and electric properties has been extensively studied in inorganic multiferroics [12–16]. Thus, both the magnetic and electric ferroic orders, their coupling, and the role of the structural deformation are important interests of dense MOFs [17, 24–31, 18–23].

There is an advantage of MOFs as multiferroics over inorganic materials. For the inorganic materials, there are several well-known obstructions to the realization of the cross-control, such as the incompatible origins of the magnetism (partially filled d-shell) and ferroelectricity (d^0) and weak coupling due to the distinct origins (*e.g.*, $BiMnO_3$) [14]. Improper ferroelectricity is a bypass mechanism around these obstructions, where the ferroelectric order is not a primary order parameter, but instead, it appears by coupling to a non-polar primary order parameter [32, 33]. A strong magneto-electric coupling can arise when this primary order parameter is the magnetic ordering or accompanies it. In some cases, the ferroelectric order can couple with more than one primary order parameter, which is referred to as hybrid improper ferroelectricity (HIFE) [34]. However, the deformations and rotations of an octahedron in the inorganic perovskite are closely correlated with those of neighboring octahedra. Thus, the symmetry lowering by a complex structural coupling, which is necessary for the HIFE, is incompatible with the original perovskite structure. This is why most of the inorganic HIFE materials are found in layered structures, such as Ruddlesden–Popper $A_{n+1}B_nO_{3n+1}$ [34–36]. However, it turned out that the MOFs can exhibit HIFE in its full 3-dimensional

ABX_3 structure [26, 37], thus emphasizing the ability of MOFs to exhibit functionality not possible in their direct perovskite analogs.

Among the MOFs, the perovskite-type (ABX_3 structure) metal guanidinium formates $[C(NH_2)_3]M(HCOO)_3$ ($M = \mathrm{Cr, Mn, Fe, Co, Ni, Cu,}$ and Zn) series [38, 26] consist of the A-site guanidinium (Gua) cation $[C(NH_2)_3]^+$, B-site $3d$ transition metal ions M^{2+}, and X-site formate $HCOO^-$ anion. These materials show the magnetic ordering by M^{2+} ions. When the transition metal ion M is a Jahn-Teller (JT) active ion Cr^{2+} (d^4) or Cu^{2+} (d^9), the HIFE was theoretically predicted for the first time in ABX_3 perovskite structures [26]. In these materials, electronic polarization[1] is coupled with the JT distortion and A-site molecule rotation. We will denote them as Cr-MOF and Cu-MOF, respectively, as used in previous studies [17, 26].

On the other hand, weak ferromagnetism (WFM), the canting of antiferromagnetically ordered spins leaving a finite uncompensated magnetic moment, is reported for the Cu-MOF theoretically [17, 29] and experimentally [38, 29] and for the Cr-MOF theoretically [26]. Since the spin canting in Cr-/Cu-MOFs originates from the JT-distortion-induced orbital ordering, the WFM moment is coupled with JT distortion, which is also coupled with the polarization. Therefore, Cr-/Cu-MOFs are magneto-electric coupled multiferroics, which is confirmed in the Cu-MOF case by the experiment [29].

In this thesis, we focus on the yet unexplored electronic and magnetic properties of the Cr-MOF and Cu-MOF, which arise from the coupling to the

[1]For briefness, we will often refer to the electric polarization moment or its density as 'polarization' in the rest of this paper, whereas we will not refer to the magnetic moment as the polarization to avoid confusion.

structural properties, such as JT distortion. For this purpose, we performed the first-principles calculations based on the density functional theory, as well as the structure analysis based on the group theoretical methods. In particular, we will show a counter-intuitive characteristic of the HIFE in Cr-/Cu-MOFs. In an intuitive sense, the polarization is nearly proportional to the polar distortion mode. However, in Cr-/Cu-MOFs, the purely electronic polarization is induced by the hybrid mode, which is coexisting two non-polar modes. It is rather a dominant contribution to the total polarization, and the polar mode actually compensates for it. It leads to a counter-intuitive result that the reversal of the polar mode does not invert the total polarization but rather enhances it. We identified its microscopic origin associated with the molecular cation and suggested a macroscopic analysis based on the Landau free energy model.

On the other hand, we also found that the orbital magnetic moment is a dominant contributor to the total magnetic moment of the Cu-MOF. In a transition metal compound with an octahedral environment, the orbital magnetic moment is usually quenched, thus often neglected as the previous theoretical studies of Cr-/Cu-MOFs [17, 26]. Even if the orbital magnetic moment is quenched, however, spin-orbit coupling (SOC) can induce a small orbital magnetic moment. In the Cu-MOF, this orbital moment is also small but larger than the WFM spin magnetic moment. We constructed a model to explain the orbital magnetic moment in the Cr-/Cu-MOF based on the second-order perturbation theory and the JT effective Hamiltonian.

The thesis is organized as follows. In Chapter 2, theoretical backgrounds for these works – the density functional theory and the theories related to ferroelectrics – are briefly introduced. Chapter 3 first briefs the known structural, electronic, and magnetic properties of the Cr-/Cu-MOFs. Next, it introduces

structural interpolations. Then, it shows the parameter settings and basic results of the DFT calculations along the structural paths. The main concerns of this thesis will be presented in this chapter. In Chapter 4, we will analyze the unusual ferroelectric properties of the Cr-/Cu-MOFs. Microscopic origin will be identified, and the macroscopic description model will be suggested. A comparison to an inorganic case will also be shown. In Chapter 5, we will first revise the analysis of the magnetism of the Cr-MOF done in the previous work [26]. Then we will develop the model to explain the orbital magnetic moment in the Cr-/Cu-MOFs. We will summarize this thesis and discuss the possible directions of further studies in Chapter 6.

2 Theoretical Backgrounds

This chapter introduces the theoretical backgrounds on which the calculations and analysis performed for this thesis are based. First, we will review the fundamentals of the density functional theory (DFT). Second, various theoretical methods of ferroelectricity will be briefly reviewed.

2.1 Density Functional Theory

Over the last half-century, DFT has been a solid ground for explaining and predicting the properties of condensed matters at the quantum mechanics level. Nowadays, DFT is widely used not only in the fundamental sciences but also in the applied sciences.

2.1.1 Hohenberg-Kohn theorem

DFT provides an efficient way of reducing the fundamental many-body quantum mechanical problem, which is practically unsolvable as it is for most of the interesting systems, into a relatively feasible problem. In particular, the ground state property of a many-electron system can be obtained by the DFT. This mapping is guaranteed by Hohenberg-Kohn (HK) theorem, which states that the ground state electronic density uniquely determines the ground state energy and electronic wavefunction, even for the interacting many-electron systems [39, 40]. Let us start with the following theorem.

The external potential is univocally determined by the electronic density, besides a trivial additive constant.

This can be shown by reduction to absurdity, i.e., firstly assume the opposite of the proposition, then show it leads to a contradiction. Assume that there exist two inequivalent potentials v and v' such that their ground state density ρ is the same. The Hamiltonians are given as $\hat{H} = \hat{T} + \hat{V}_{\text{ext}} + \hat{U}_{\text{ee}}$, where $\hat{T}$ is kinetic energy operator, $\hat{V}_{\text{ext}}$ is external potential operator given by v, and $\hat{U}_{\text{ee}}$ is electron-electron Coulomb interaction operator, and $\hat{H}'$ given by v'. The ground state wavefunction Φ (Φ') and energy $E_0 = \langle\Phi|\hat{H}|\Phi\rangle$ ($E_0' = \langle\Phi'|\hat{H}'|\Phi'\rangle$) will be given accordingly. When we consider the ground state energy E_0, variational principle dictates for the 'non-ground state' wavefunction $\Phi' \neq \Phi$ that

$$\begin{aligned} E_0 < \langle\Phi'|\hat{H}|\Phi'\rangle &= \langle\Phi'|\hat{H}'|\Phi'\rangle + \langle\Phi'|\hat{H} - \hat{H}'|\Phi'\rangle \\ &= E_0' + \int d\mathbf{r}\rho(\mathbf{r}) \left[v_{\text{ext}}(\mathbf{r}) - v_{\text{ext}}'(\mathbf{r})\right]. \end{aligned} \tag{2.1}$$

On the other hand, the following is also true.

$$\begin{aligned} E_0' < \langle\Phi|\hat{H}'|\Phi\rangle &= \langle\Phi|\hat{H}|\Phi\rangle + \langle\Phi|\hat{H}' - \hat{H}|\Phi\rangle \\ &= E_0 + \int d\mathbf{r}\rho(\mathbf{r}) \left[v_{\text{ext}}'(\mathbf{r}) - v_{\text{ext}}(\mathbf{r})\right]. \end{aligned} \tag{2.2}$$

By adding above Eq. (2.1) and Eq. (2.2), we obtain $E_0 + E_0' < E_0' + E_0$, which is definitely a contradiction. Therefore, the initial assumption is disproved, i.e., for a given ground state electron density ρ, the external potential $v_{\text{ext}}(\mathbf{r})$ that generates the ρ is uniquely determined besides an additive constant.

As a corollary, the ground state wavefunction Φ is also univocally determined from the ground state density ρ. This is straightforward from a consecutive determination $\rho \to v \to \hat{H} \to \Phi$. Note that the ρ can also be determined from Φ, thus implying a self-consistency of this formulation.

HK theorem leads to a definition of an energy functional that maps a density $\tilde{\rho}$ to the variational energy E_v:

$$E_v[\tilde{\rho}] = F[\tilde{\rho}] + \int d\mathbf{r}\tilde{\rho}(\mathbf{r})v_{\text{ext}}(\mathbf{r}) \tag{2.3}$$

with the universal functional, which is independent of v_{ext},

$$F[\tilde{\rho}] = \left\langle \Phi[\tilde{\rho}] \middle| \hat{T} + \hat{U}_{\text{ee}} \middle| \Phi[\tilde{\rho}] \right\rangle, \tag{2.4}$$

where $\Phi[\tilde{\rho}]$ is the ground state wavefunction of a potential given by $\tilde{\rho}$ as its ground state density.

2.1.2 Kohn-Sham equation

HK theorem provided a justification of the DFT but not a practical way of it. Kohn-Sham (KS) approach based on an effective single-particle problem is the very practical methodology of the DFT [41, 40]. In the KS approach, we assume a non-interacting system whose ground state density is the same as that of the interacting system. This 'reference' system is described by the Hamiltonian

$$\hat{H}_r = \sum_{i=1}^{N} \left[-\frac{\hbar^2}{2m}\nabla_i^2 + v_r(\mathbf{r}_i) \right], \tag{2.5}$$

where N is the number of electrons. Our goal becomes to find the correct formulation of the reference potential $v_r(\mathbf{r})$.

Let us consider the spinless case for convenience. The wavefunction of Eq. (2.5) is a Slater determinant of N single-particle wavefunctions,

$$\Phi(\mathbf{r}) = \frac{1}{\sqrt{N!}}\text{SD}[\phi_1(\mathbf{r}_1)\phi_2(\mathbf{r}_2)...\phi_N(\mathbf{r}_N)]. \tag{2.6}$$

KS Hamiltonian is the one-electron Hamiltonian which has the single particle 'KS orbitals' $\{\phi_i\}$ as its eigenstates, i.e.,

$$\hat{H}_{\mathrm{KS}}\phi_i = \varepsilon_i\phi_i, \text{ where } \quad \hat{H}_{\mathrm{KS}} = -\frac{\hbar^2}{2m}\nabla^2 + v_r(\mathbf{r}). \tag{2.7}$$

It follows that the density is written as

$$\rho(\mathbf{r}) = \sum_{i=1}^{N} \left|\phi_i(\mathbf{r})\right|^2 \tag{2.8}$$

and that the kinetic energy is

$$T_r[\rho] = -\frac{\hbar^2}{2m}\left\langle \phi_i|\nabla^2|\phi_i\right\rangle. \tag{2.9}$$

Then the universal functional Eq. (2.4) is rewritten in the KS context,

$$F[\rho] = T_r[\rho] + \frac{1}{2}\int\int d\mathbf{r}d\mathbf{r}'\frac{\rho(\mathbf{r})\rho(\mathbf{r}')}{|\mathbf{r}-\mathbf{r}'|} + E_{\mathrm{XC}}[\rho], \tag{2.10}$$

where $E_{\mathrm{XC}}[\rho]$ is the exchange-correlation (XC) energy functional, which comes from the antisymmetric nature of the wavefunction and the electron-electron interactions. The KS total energy functional can be defined as

$$E_{\mathrm{KS}}[\rho] = F[\rho] + \int d\mathbf{r}\rho(\mathbf{r})v_{\mathrm{ext}}(\mathbf{r}). \tag{2.11}$$

Since we have to find a ground state density ρ, the variational principle with respect to ρ will lead to the information of v_r. In this case, there must be a constraint on ρ that its integral should be the number of electrons, i.e., $\int d\mathbf{r}\rho(\mathbf{r}) = N$. Including this constraint with a Lagrange multiplier μ, a functional derivative of Eq. (2.11) with respect to ρ is given as

$$\frac{\delta}{\delta\rho(\mathbf{r})}\left(E_{\mathrm{KS}}[\rho] - \mu\int d\mathbf{r}\rho(\mathbf{r})\right) = 0. \tag{2.12}$$

After some of the functional analysis and physical consideration [40], the reference potential is obtained as

$$v_r(\mathbf{r}) = v_{\text{ext}}(\mathbf{r}) + \int d\mathbf{r}' \frac{\rho(\mathbf{r})}{|\mathbf{r} - \mathbf{r}'|} + \mu_{\text{XC}}[\rho](\mathbf{r}), \tag{2.13}$$

where

$$\mu_{\text{XC}}[\rho](\mathbf{r}) = \frac{\delta E_{\text{XC}}[\rho]}{\delta \rho(\mathbf{r})} \tag{2.14}$$

is the XC potential.

A practical DFT calculation is an iterative solving of the KS equation. From an initial density guess ρ_0, KS equation Eq. (2.7) is constructed via Eq. (2.13). By solving the initial KS equation, one can obtain a set of eigenstates $\{\phi_i^1\}$. A new density ρ_1 is then obtained from $\{\phi_i^1\}$, which, however, can differ from ρ_0. The new density ρ_1 defines a new KS equation, new eigenstates, and a new density ρ_2 again. Repeating this procedure, one can obtain the converged ρ as a ground state density. This iterative way is called the self-consistent field (SCF) method.

However, the explicit form of the XC functional Eq. (2.14) is unknown. Thus, various approximations on $\mu_{\text{XC}}[\rho]$ have been suggested. The simplest one is the local-density approximation (LDA) [42], which assumes that an infinitesimal volume of the electron density contributes to XC energy as much as that of the uniform electron gas of the same density contributes. Next, the generalized gradient approximation (GGA) [43], which takes the gradient of the electron density into account, was suggested. Furthermore, methodologies that include the correction of the on-site Coulomb repulsion energies by hand (DFT+U methods [44, 45]) or that adopt the exact exchange energy from the Hartree-Fock method in part (hybrid functional [46]) have been suggested.

An appropriate choice of the XC functional is also an important part of the practical DFT.

2.2 Ferroelectricity

Ferroelectricity is a property in which a reversible electric polarization spontaneously appears in the material even without an external electric field. Reversibility is an essential feature that distinguishes ferroelectricity from pyroelectricity. It is straightforward that there must be a non-polar intermediate state in the middle of the polarization reversal path. The crystal structure of this non-polar state would have a higher symmetry than the ferroelectric structure. Therefore, this structure might be preferred at a high temperature, where the entropy effect becomes more significant. The ferroelectric phase transition is a transition from this high-symmetric structure, or paraelectric structure, into the ferroelectric structure below the critical temperature T_c. Landau established a simple but powerful theory to describe the ferroelectric phase transition [47].

2.2.1 Landau free energy theory

Landau theory assumes that around the critical temperature T_c, the free energy of a system can be written as a Taylor expansion of an order parameter, in this case, macroscopic polarization P. This particular case of ferroelectricity is also known as Landau-Devonshire theory [47, 48]. For example, free energy can be written as

$$F = \frac{1}{2}a(T - T_c)P^2 + \frac{1}{4}bP^4 + \frac{1}{6}cP^6 - EP, \tag{2.15}$$

where a and c are positive, T is temperature, and E is an external electric field. In the absence of E, F is an even function of P, which is consistent with a switchability of the ferroelectricity. By definition, the spontaneous polarization P^* is the P that makes the free energy F minimum. In the case of $T \gg T_c$, it is straightforward that $P^* = 0$, i.e., the spontaneous polarization vanishes, which corresponds to the paraelectric phase. In the case of $T \ll T_c$, the two minima of the symmetric double well type F located at $P \neq 0$ corresponds to P^*. They can be obtained from the derivative of F [Eq. (2.15)] with respect to P ($E = 0$ case is considered),

$$\frac{\partial F}{\partial P} = a(T - T_c)P + bP^3 + cP^5 = 0. \tag{2.16}$$

By truncating the P^5 term and assuming $b > 0$, one can obtain the spontaneous polarization,

$$P^* = \pm\sqrt{\tfrac{a}{b}(T_c - T)}. \tag{2.17}$$

This corresponds to the second-order phase transition. On the other hand, when we assume $b < 0$, the free energy can describe the first-order phase transition.

Although the Landau free energy theory is initially introduced to describe the phase transition, it is also useful as a descriptor of the couplings between the order parameters, energy, and external fields. Hereafter, we will omit the temperature dependence of the free energy and only focus on the couplings between other physical parameters. For example, the minimal descriptor version of Eq. (2.15) in the ferroelectric phase is

$$F = \alpha P^2 + \tfrac{1}{2}\beta P^4 \quad (\alpha < 0 \text{ and } \beta > 0) \tag{2.18}$$

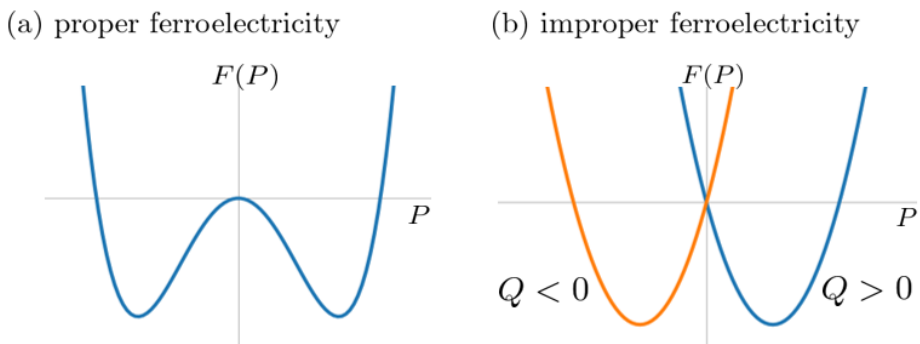

Figure 2.1 Schematic free energy profiles of the (a) proper ferroelectricity and (b) improper ferroelectricity cases. In (b), whether the minimum position is on the positive side or the negative side depends on Q.

as schematically depicted in Fig. 2.1 (a), with the spontaneous polarization

$$P^* = \pm\sqrt{-\frac{\alpha}{\beta}}. \tag{2.19}$$

In this case, polarization P is the only order parameter. In other words, P drives the phase transition as a primary order parameter. This is the definition of proper ferroelectricity.

Interestingly, ferroelectric order can appear by coupling to another order parameter [32, 33]. Let us assume a non-polar primary order parameter Q, which is also described by free energy analogous to Eq. (2.15) or Eq. (2.18), f. Then the minimal description of the free energy is

$$F = f(Q^2, Q^4) + \alpha P^2 + \gamma QP \quad (\alpha > 0) \tag{2.20}$$

with the spontaneous polarization

$$P^* = -\frac{\gamma}{2\alpha}Q. \tag{2.21}$$

The free energy profile is a single well shape with respect to P, as depicted in Fig. 2.1 (b). This case is referred to as improper ferroelectricity. In the absence

of Q, P does not appear. The ferroelectric switching is not a sole switching of the P but induced by the switching of the primary order parameter Q.

Furthermore, P can couple with more than one order parameter. Let us consider the case that P couples with two order parameters, Q_{X_1} and Q_{X_2}, where X_1 and X_2 are the irreducible representations that each mode corresponds to. The free energy can be written as

$$F = f(\{Q_{X_i}^{2n}\}) + \alpha P^2 + \gamma Q_{X_1} Q_{X_2} P \quad (\alpha > 0) \tag{2.22}$$

with the spontaneous polarization

$$P^* = -\frac{\gamma}{2\alpha} Q_{X_1} Q_{X_2}. \tag{2.23}$$

It defines the hybrid improper ferroelectricity (HIFE) [34]. Similarly to the previous case, the presence of Q_{X_1} and Q_{X_2} is necessary for the appearance of P. It exhibits an interesting switching rule: P is inverted when either of Q_{X_1} or Q_{X_2} is inverted, but not both.

2.2.2 Structure analysis: A group theoretical method

As mentioned before, a ferroelectric phase transition occurs between the high-symmetric non-polar and low-symmetric polar systems. The non-polar system is also called pseudosymmetric as the structure is hypothetical. When the space group of the polar phase (low symmetry) is H, there exist supergroups $G > H$ that have higher symmetry than H. In this case, the following coset decomposition is possible.

$$G = H + g_2 H + g_3 H + ... + g_n H, \tag{2.24}$$

where $g_i \in G$ are coset representatives which $g_i \notin H$, and n is the index of H in G. For the H of a given polar system, with the consideration of the Wyckoff position splittings, the candidates of the pseudosymmetry can be specified among the supergroup G's [49, 50]. For a set of atomic positions S_1 corresponding to H, $n-1$ hypothetical structures $S_i = g_i S_1$ can be obtained from the coset representatives $\{g_i \in G | i = 2, ..., n\}$. When the hypothetical high-symmetric structure invariant under G is S_0, we can write $S_i = S_0 + U_i$, where U_i is a small distortion relating two phases. Then we can define $\Delta U_i = S_i - S_1 = g_i U_1 - U_1$. If all ΔU_i are sufficiently small, for example, under a specific criterion, we can say that S_0 is a pseudosymmetric structure of the system.

The displacement vector $\mathbf{u}$ can be defined as the difference vector from the pseudosymmetric structure to the polar structure. This is also considered the 'soft' phonon mode of the pseudosymmetric structure. One can label the $\mathbf{u}$ with an irreducible representation (*irrep*) of the point group defined in G at a specific k-point or decompose it into several orthogonal modes according to irreps [51]. Note that the modulation through the lattice is determined by the Bloch phase factor $e^{i\mathbf{k}\cdot\mathbf{r}}$.

In general, the basis function(s) of an irrep Γ of a group G can be extracted from an arbitrary function F by the projector

$$\hat{P}^{\Gamma} = \frac{l}{h} \sum_{g \in G} \chi_g^{\Gamma *} g, \tag{2.25}$$

where χ_g^{Γ} is the character of symmetry operator $g \in G$ in the irrep Γ, h is the number of symmetry operators in G, and l is the dimensionality of irrep Γ [51]. Then, $\hat{P}^{\Gamma} F = \sum_k f_k^{\Gamma} |\Gamma k\rangle$, where $|\Gamma k\rangle$ is the k-th basis ($k = 1, ..., l$) of Γ. In this way, $\mathbf{u}$ can also be labeled with or decomposed according to the irreps.

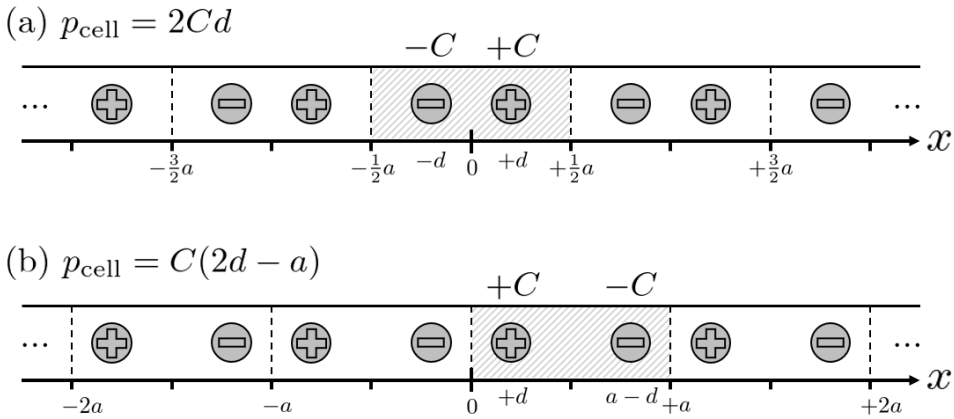

Figure 2.2 The ambiguity of the dipole moment per unit cell is schematically shown. In both (a) and (b), charged ions are placed identically with a lattice constant a. However, the dipole moments p_{cell} depend on the unit cell conventions, which are marked by oblique lines.

2.2.3 First-principles approach: Berry phase method

Contrary to the simple and intuitive concept of electric polarization, an actual formulation of it in an extended system, such as a periodic crystal, suffers from ambiguities. For example, imagine a one-dimensional array of a unit cell with lattice constant a containing two $\pm C$ charged ions at $\pm d$. Depending on the definition of the unit cell, the dipole moment per unit cell can be either $2Cd$ or $C(2d - a)$, as shown in Fig. 2.2. This implies that a direct extension of the definition of the electric dipole to the electric polarization density of a periodic crystal,

$$\mathbf{P} = \frac{-e}{\Omega_{\text{cell}}} \int_{\text{cell}} d\mathbf{r}\ \mathbf{r}\rho(\mathbf{r}) \tag{2.26}$$

is an ill-defined quantity.

The key to resolving this ambiguity is to redefine the macroscopic polarization as a change of the polarization from a non-polar reference system to a polar system [52, 53], which is rather compatible with experimental measurement

of it. During this change, a current density $\mathbf{j}(t) = d\mathbf{P}(t)/dt$ will adiabatically flow. From this context, macroscopic polarization is written as

$$\Delta\mathbf{P} = \mathbf{P}(\Delta t) - \mathbf{P}(0) = \int_0^{\Delta t} dt\, \mathbf{j}(t) = \int_0^1 d\lambda \frac{d\mathbf{P}}{d\lambda}, \tag{2.27}$$

where $\lambda = 0$ is the non-polar reference system and $\lambda = 1$ is the polar system.

In terms of quantum mechanics, an adiabatic change is recorded in a Bloch wavefunction $\psi_{n\mathbf{k}}(\mathbf{r}) = e^{i\mathbf{k}\cdot\mathbf{r}} u_{n\mathbf{k}}(\mathbf{r})$ as

$$|\delta\psi_{n\mathbf{k}}\rangle = -i\hbar\dot{\lambda} \sum_{m\neq n} \frac{\langle\psi_{m\mathbf{k}}|\partial_\lambda\psi_{n\mathbf{k}}\rangle}{E_{n\mathbf{k}} - E_{m\mathbf{k}}} |\psi_{m\mathbf{k}}\rangle \tag{2.28}$$

in the first-order correction, where n is a band index, $\mathbf{k}$ is a crystal momentum, and $\dot{\lambda} = d\lambda/dt$. Note that $H|\psi_{n\mathbf{k}}\rangle = E_{n\mathbf{k}}|\psi_{n\mathbf{k}}\rangle$ and $H_{\mathbf{k}}|u_{n\mathbf{k}}\rangle = E_{n\mathbf{k}}|u_{n\mathbf{k}}\rangle$, where $H_{\mathbf{k}} = e^{-i\mathbf{k}\cdot\mathbf{r}} H e^{i\mathbf{k}\cdot\mathbf{r}}$. The corresponding current density is

$$\mathbf{j}_n = \frac{d\mathbf{P}_n}{dt} = \frac{i\hbar e\dot{\lambda}}{(2\pi)^3 m_e} \sum_{m\neq n} \int d\mathbf{k} \frac{\langle\psi_{n\mathbf{k}}|\mathbf{p}|\psi_{m\mathbf{k}}\rangle \langle\psi_{m\mathbf{k}}|\partial_\lambda\psi_{n\mathbf{k}}\rangle}{E_{n\mathbf{k}} - E_{m\mathbf{k}}} + c.c. \tag{2.29}$$

From a perturbation theory, this can be modified to

$$\frac{d\mathbf{P}_n}{d\lambda} = \frac{ie}{(2\pi)^3} \int d\mathbf{k} \langle\nabla_{\mathbf{k}} u_{n\mathbf{k}}|\partial_\lambda u_{n\mathbf{k}}\rangle + c.c. \tag{2.30}$$

Inserting Eq. (2.30) to Eq. (2.27), the electronic contribution of the polarization is given as

$$\mathbf{P}_{\text{ele.}} = \frac{e}{(2\pi)^3} \operatorname{Im} \sum_n \int d\mathbf{k} \langle u_{n\mathbf{k}}|\nabla_{\mathbf{k}}|u_{n\mathbf{k}}\rangle . \tag{2.31}$$

Finally, the total polarization is $\mathbf{P} = \mathbf{P}_{\text{ele.}} + \mathbf{P}_{\text{core}}$ with the core contribution from the nuclei charges (in practice, including core electrons)

$$\mathbf{P}_{\text{core}} = \frac{e}{\Omega_{\text{cell}}} \sum_s Z_s^{\text{core}} \mathbf{r}_s. \tag{2.32}$$

Since the mathematical form of $\mathbf{P}_{\text{ele.}}$ is that of the Berry phase in k-space, this formalism is referred to as the Berry phase method [52]. However, in a

strict sense, this corresponds to the Zak phase [54], not a Berry phase, because a path defined in Eq. (2.31) is not a closed loop. Hence, the value of $\mathbf{P}_{\text{ele.}}$ depends on the origin of the coordinate system. However, this dependency is canceled with the opposite dependence of the $\mathbf{P}_{\text{core}}$, thus leaving the total polarization $\mathbf{P}$ invariant under the origin shift, i.e., the $\mathbf{P}$ is unambiguously determined.

Moreover, since the phase is defined modulo 2π, Eq. (2.31) is also determined with the corresponding modulation, or polarization quantum e/A, where A is the projected unit cell area on the normal plane to a specific polarization direction. Nevertheless, when we construct a gradual structural path from a reference non-polar structure and calculate Eq. (2.31) along the path, the final polarization can be determined unambiguously.

The Berry phase method is also naturally connected with the point charge picture by the Wannier function [53]. The Wannier function is obtained from a Bloch wavefunction by the following transformation.

$$|w_{n\mathbf{R}}\rangle = \frac{\Omega_{\text{cell}}}{(2\pi)^3} \int d\mathbf{k} e^{i\mathbf{k}\cdot\mathbf{R}} |\psi_{n\mathbf{k}}\rangle \tag{2.33}$$

Since the Wannier function is localized around the cell $\mathbf{R}$, the position expectation value of the Wannier function, i.e., the Wannier center, naturally represents the localized point charge.

$$\mathbf{r}_{n\mathbf{R}} = \langle w_{n\mathbf{R}}|\mathbf{r}|w_{n\mathbf{R}}\rangle = \frac{\Omega_{\text{cell}}}{e}\mathbf{P}_n + \mathbf{R}, \tag{2.34}$$

where the $\mathbf{P}_n$ is the polarization corresponding to $|w_{n\mathbf{R}}\rangle$. The modulation of the polarization is also naturally given by $\mathbf{R}$.

Interestingly, the Berry phase method can recover the correct formula of the isolated electric dipole case. Let us assume that there is a polar molecule in a

very large periodic cell (lattice constant L), so that we can still define the crystal momentum k, but there is no interaction between the neighboring molecules. In this case, k-dependence in the Bloch wavefunction ψ vanishes. However, by definition, the periodic part $u_k(x) = e^{-ikx}\psi(x)$ still has a k-dependence (for simplicity, we assume a 1D single-band case). The electronic polarization is given as

$$\begin{aligned} P_{\text{ele.}} &= \frac{e}{2\pi} \operatorname{Im} \int dk \left\langle u_k(x) \middle| \partial_k \middle| u_k(x) \right\rangle \\ &= \frac{e}{2\pi} \operatorname{Im} \frac{2\pi}{L} \left\langle \psi(x) \middle| -ix \middle| \psi(x) \right\rangle = \frac{-e}{L} \int dx \; x\rho(x). \end{aligned} \tag{2.35}$$

The polarization density written with the usual dipole formula is restored. This justifies the use of the Berry phase method for the polarization along a non-periodic direction in a periodic cell with a vacuum, which is common in practical DFT calculations, such as the out-of-plane direction of 2D materials [55].

3 Cr- and Cu-MOFs: Basics and DFT Results

In this chapter, we will briefly review the known properties of the metal guanidinium formates $[C(NH_2)_3]M(HCOO)_3$ (M = Cr, Cu; Cr-MOF and Cu-MOF) from the previous studies [38, 17, 26, 29]. Then we will introduce the definition of the structural interpolations. After the detailed computational parameters used in this thesis are described, finally, we will show the basic DFT results, which we will analyze in the later chapters.

3.1 Known Electronic and Magnetic Properties

Cr-/Cu-MOFs have a perovskite-type ABX_3 structure, as shown in Fig. 3.1 for the Cu case. A B-site cation Cr^{2+}/Cu^{2+} is surrounded by six oxygen atoms from six surrounding X-site molecular anions $HCOO^-$ (formate), thus forming MO_6 octahedron. In addition, guanidinium (Gua) ions $[C(NH_2)_3]^+$ occupy the A-site positions [38].

In the O_6 octahedron cage, d-orbitals are energetically separated into lower energy t_{2g} orbitals (d_{yz}, d_{zx}, d_{xy}) and higher energy e_g orbitals ($d_{x^2-y^2}, d_{z^2}$) by the crystal field splitting. Since the Cr^{2+} and Cu^{2+} have d^4 (high spin) and d^9 electron configurations, respectively, two e_g orbitals are degenerated unless the symmetry is further reduced. When the octahedron is deformed so that the symmetry is reduced, the degeneracy is split, which gives rise to the energy

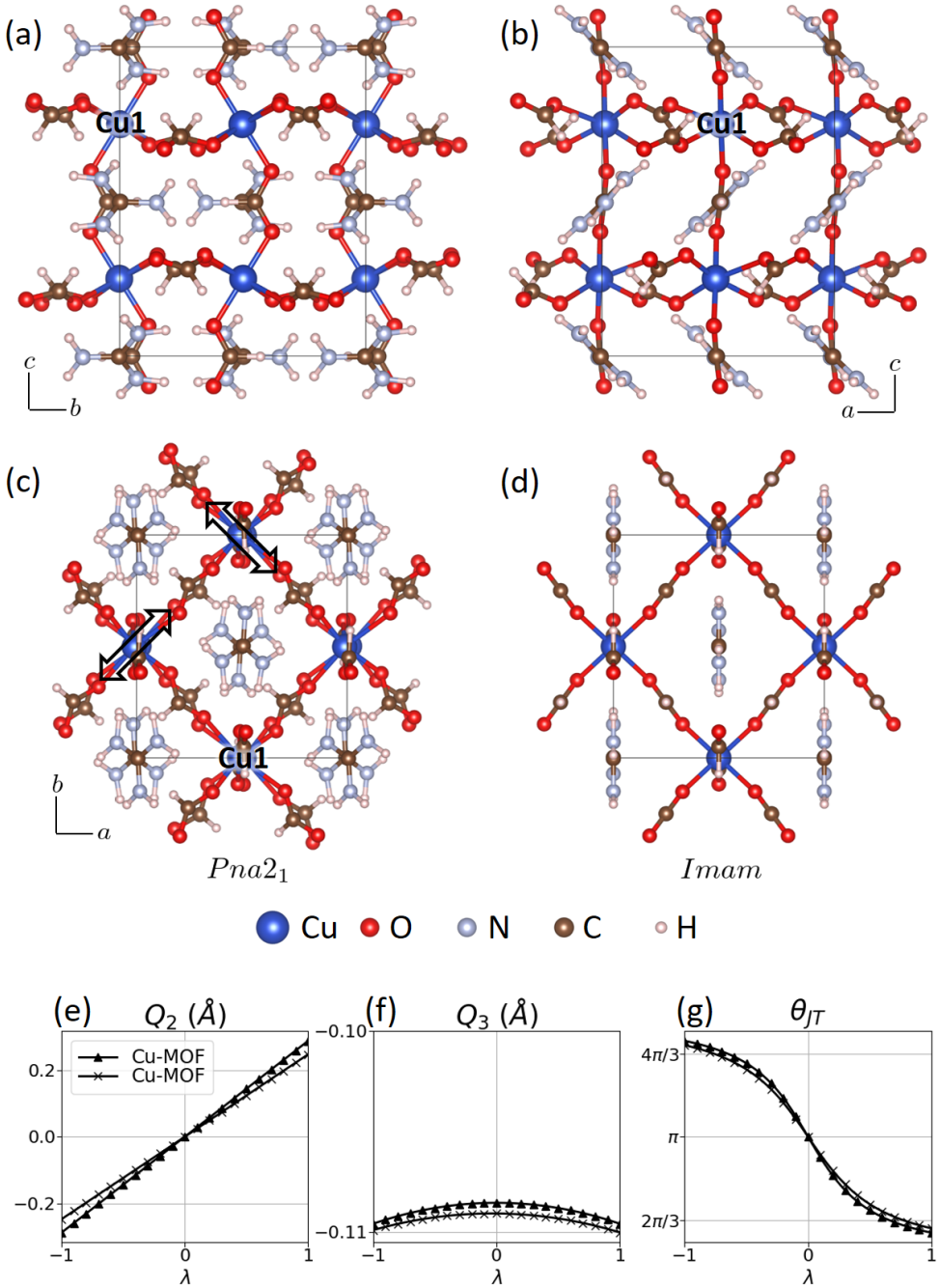

Figure 3.1 (a-c) $Pna2_1$ structure Cu-MOF ($\lambda = 1$). The reference Cu1 is labeled. In (c), elongated directions are drawn by double-arrows. (d) $Imam$ structure Cu-MOF. JT modes (e) Q_2 and (f) Q_3 of the reference Cu1 and Cr1 and their (g) JT phase are shown with respect to λ.

lowering because only the lower level among the two split levels is occupied. In other words, the octahedron spontaneously deforms itself to stabilize the energy when there exists degeneracy, which is referred to as the Jahn-Teller (JT) effect [56, 57].

The basic octahedral tilting in $[C(NH_2)_3]M(HCOO)_3$ series is $a^-a^-c^-$ in the Glazer notation. In addition, JT distortion induces the octahedral elongations of which the elongation axes are alternating in ab-plane in Cr-/Cu-MOFs [38, 26]. This antiferro-distortive (AFD) ordering of O_6 octahedra induces the orbital ordering [17, 26]: The lobe of the e_g orbital heads for the perpendicular direction of the lobes of the neighboring e_g orbitals. In other words, a cooperative JT effect determines the orbital structure. In this case, the Goodenough-Kanamori-Anderson rule [58, 57] predicts the ferromagnetic (FM) interaction between the in-plane neighboring ions and antiferromagnetic (AFM) interaction between the out-of-plane neighboring ions. It results in the A-type AFM. The theoretically predicted AFM alignment axis is crystallographic c-axis for Cu-MOF and a-axis for Cr-MOF [17, 26].

On the other hand, antiferromagnetically ordered spins exhibit additional canting toward a specific direction, called weak ferromagnetism (WFM). In Cr-MOF, spins are canted toward c-direction [26], whereas in Cu-MOF, a-direction [17]. Usually, the spin canting is attributed to two origins, Dzyaloshinskii-Moriya interaction (DMI) [59, 60] and magnetic single-ion anisotropy (MSIA), both of which are in fact the results of the spin-orbit coupling (SOC). However, the previous work excluded the possibility of DMI according to the symmetry analysis. It was shown that the MSIA can induce the spin canting on the basis of the perturbation theory on the SOC considering the JT orbital ordering. The WFM in Cu-MOF is also experimentally confirmed [38, 29].

This AFD JT distortion also results in that the Cr-/Cu-MOFs have a polar space group $Pna2_1$ (No. 33), whereas the other non-JT-active members of the series have a non-polar space group $Pnan$ (No. 52, $Pnna$ in standard settings) [38]. Therefore, if we restore the JT distortion in Cr-/Cu-MOFs, we can obtain the $Pnan$ structure, which is a pseudosymmetric structure of Cr-/Cu-MOFs. The ferroelectric switching path can be constructed between the $Pna2_1$ and $Pnan$. Along the reversal of this path, the previous theoretical works [17, 26] show the double well type total energy profile and the ferroelectric polarization switching. Moreover, reversal of the WFM moment is observed along with the ferroelectric switching, i.e., Cr-/Cu-MOFs are electromagnetic coupled multiferroics. The electromagnetic coupling was experimentally realized for the Cu-MOF [29].

Furthermore, it was shown that the ferroelectricity of the Cr-/Cu-MOFs can be classified as the hybrid improper ferroelectricity (HIFE) [26]. This can be shown from another pseudosymmetric structure $Imam$ (No. 74, $Imma$), which has a higher symmetry than $Pnan$. In this structure, all Gua ions are aligned parallel to each other in comparison to the $Pnan$ structure. The displacements from $Imam$ structure to $Pna2_1$ structure can be decomposed into three orthogonal modes labeled after the irreducible representations Γ_4^-, X_1^-, and X_4^+. Γ_4^- mode is a polar mode. If only the Γ_4^- mode is present, the structure has a $Ima2$ space group (No. 46). X_1^- mode corresponds to the rotation of Gua ions, resulting in the $Pnan$ space group. X_4^+ mode mainly corresponds to the distortion of MO_6 octahedra (JT distortion) and includes a small distortion of the Gua ion, resulting in $Pnam$ space group (No. 62, $Pnma$). If only one non-polar mode solely exists, either X_1^- or X_4^+, the total energy decreases, i.e., X_1^- and X_4^+ are unstable modes. On the other hand, if

only the polar mode Γ_4^- exists, the total energy increases, i.e., stable mode. The presence of two non-polar modes is necessary for the polar mode to appear. This defines the HIFE.

Based on the knowledge described so far, we will explore further interesting electronic and magnetic properties of the Cr-/Cu-MOFs in this thesis: A counterintuitive ferroelectric property from a purely electronic polarization and a robust orbital weak ferromagnetism. As a preliminary, we will show the basic computational results in the rest of this chapter.

3.2 Structure Interpolations

In this chapter, we will define the structural interpolation starting from the pseudosymmetric structures, which is also used in the previous works [17, 26]. First, we will consider the case that the pseudosymmetry is $Pnan$. Let us write the atomic displacements from the $Pnan$ structure to the original $Pna2_1$ structure by the vector $\mathbf{u}$. When we write the atomic positions at $Pnan$ as $\mathbf{r}_{Pnan}$, the $Pna2_1$ structure is $\mathbf{r}_{Pnan}+\mathbf{u}$. By introducing the linear interpolation parameter λ, we can define a structure interpolation $\mathbf{r}_1(\lambda) = \mathbf{r}_{Pnan}+\lambda\mathbf{u}$ ($\lambda = 0$ for the $Pnan$ and $\lambda = 1$ for the original $Pna2_1$ structure). This displacement is labeled by single mode Γ_4^-. We will denote these interpolated structures as $Pnan$-path in this thesis. The previous studies [17, 26] showed the ferroelectric and WFM switching along the path from $\lambda = 1$ to $\lambda = -1$.

Secondly, let us consider the case that the pseudosymmetry is $Imam$, which we will call $Imam$-path. The atomic displacement from the $Imam$ to $Pna2_1$ can be decomposed into three orthogonal modes, i.e., $\mathbf{u}_2 = \mathbf{u}_{\Gamma_4^-} + \mathbf{u}_{X_1^-} + \mathbf{u}_{X_4^+}$, where the subscript at each mode is the irrep label. The structure interpolation

can be defined in terms of three linear interpolation parameters for each modes, $\mathbf{r}_2(\lambda_{\Gamma_4^-}, \lambda_{X_1^-}, \lambda_{X_4^+}) = \mathbf{r}_{Imam} + \lambda_{\Gamma_4^-}\mathbf{u}_{\Gamma_4^-} + \lambda_{X_1^-}\mathbf{u}_{X_1^-} + \lambda_{X_4^+}\mathbf{u}_{X_4^+}$. From $\mathbf{r}_2(\lambda_{\Gamma_4^-}, \lambda_{X_1^-}, \lambda_{X_4^+})$, we can construct hypothetical structures, which can be used to investigate the effects of each mode. For example, the combination of X_1^- and X_4^+ modes without Γ_4^- mode is $\mathbf{r}_2(0, 1, 1)$. Interestingly, this structure is already $Pna2_1$, even though neither of X_1^- and X_4^+ modes is a polar mode. We denote this combined mode $\mathbf{u}_{X_1^-} + \mathbf{u}_{X_4^+}$ as $X_1^- \oplus X_4^+$ hybrid mode.

3.3 Computational Details

We performed the first-principles DFT calculation to obtain the total energy and electric and magnetic properties at a structure given by the structure interpolation defined in the previous section. In particular, we used the Vienna Ab initio Simulation Package (VASP) [61]. To include SOC, we performed a non-collinear spin DFT calculations. We adopted the generalized gradient approximation of Perdew-Burke-Ernzerhof (GGA-PBE) for the exchange-correlation functional [43]. The projector augmented wave pseudo-potentials [62] were used. The plane wave energy cut-off was chosen to be 500 eV. $4 \times 4 \times 4$ regular k-space grid was used. It is noteworthy that the orbital magnetic moment was calculated within the atom-centered approximation [63]: The Bloch wavefunction is projected on the atomic orbitals, and the orbital angular momentum is calculated via the atomic angular momentum operators with the projected wavefunction. The atom-centered approximation is sufficient for the Cr-/Cu-MOF because the Cr/Cu preserves its atomic characters in these materials, i.e., no need for the 'modern theory' of the orbital angular momentum [64]. When we examined the spin model, we included the cases

where we performed the DFT+$U + J$ calculations, which consider the on-site Coulomb energy correction, whereas we did not consider it for other cases. To obtain the electric polarization moment in the periodic crystal, we used the Berry phase method [52].

For the lattice constants, experimental values of Cu-MOF $a = 8.5212$ Å, $b = 9.0321$ Å, and $c = 11.3497$ Å from Ref. [38] were used for both Cr- and Cu-MOF for consistency with the previous theoretical works [17, 26]. For a given ferroelectric structure, the corresponding paraelectric pseudosymmetric structures were obtained by the group-theoretic method implemented in PSEUDO of the Bilbao Crystallography server [50]. Atomic displacements from the higher symmetry structure to the lower symmetry structure were decomposed into orthogonal modes labeled after the irreps by using AMPLIMODE of Bilbao Crystallography server [65].

3.4 DFT Results

This section shows the change of total energy, polarization, and magnetization calculated from the DFT along the structure interpolation paths, *Pnan*-path and *Imam*-path. Their analysis based on the physical models will be in following chapters.

3.4.1 *Pnan*-path

The results on the *Pnan*-path, from $\lambda = -1$ to $\lambda = +1$ of $\mathbf{r}_1(\lambda)$, are shown in Fig. 3.2. Overall behaviors shown in the previous studies [17, 26] are reproduced. In both Cr-/Cu-MOFs, the energy profiles are double well-type [Fig. 3.2 (a)], and the polarizations along the c-axis are inverted [Fig. 3.2 (b)], i.e., ferroelectric

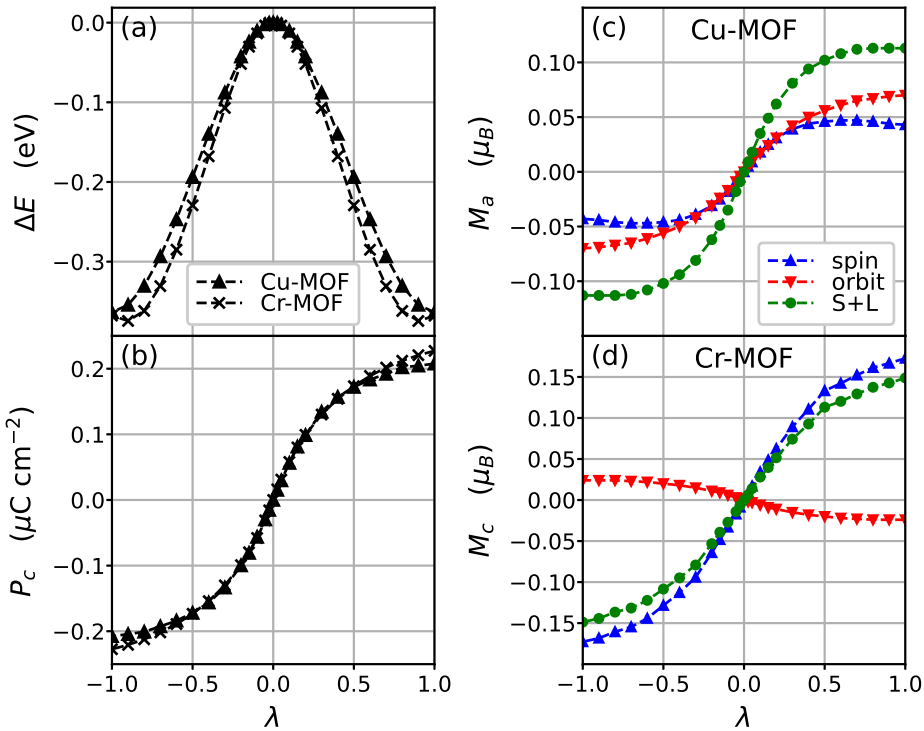

Figure 3.2 (a) Change of the energy and (b) electric polarization of the Cu-/Cr-MOF with respect to the structure parameter λ. Spin, orbital, and total (spin+orbital; S+L) magnetic moment of (c) Cu-MOF and (d) Cr-MOF with respect to λ of *Pnan*-path.

transition. The polarization densities are 0.21 μC/cm^2 for Cu-MOF and 0.23 μC/cm^2 for Cr-MOF.

For the magnetic property, WFM moments appear along the c-axis for Cr-MOF (0.172 μ_B per unit cell) and a-axis for Cu-MOF (0.043 μ_B) and are also inverted along the path [Fig. 3.2 (c) and (d)]. However, we found that the calculated total spin magnetic moment in the Cr-MOF (0.04 μ_B per each Cr corresponding to the canting angle 0.63°) is significantly smaller than that of the previous work (1 μ_B, 14.5°) [26]. We guess that the previous calculations were trapped near the initial conditioning due to very weak spin anisotropy

energy. This is rather consistent with the recently reported experimental observation [66].

We also calculated the orbital magnetic moment, which was overlooked in the previous studies [17, 26]. Interestingly, in the Cu-MOF, the orbital magnetic moment is comparable to the spin magnetic moment in the same direction. In the large $|\lambda|$ range, the orbital contribution is larger than the spin contribution. On the other hand, for the Cr-MOF, the orbital moment is much smaller in comparison with the spin moment in the opposite direction to it. This is consistent with the fact that the spin and orbital moments are opposed to each other when the d-orbitals are less than half-filled but aligned when the d-orbitals are more than half-filled. The experimentally observed effective magnetic moment of the Cu-MOF is notably higher than its spin-only moment [38]. We will analyze this orbital magnetic moment later.

3.4.2 *Imam*-path

Now we will consider the DFT results along the various structure paths defined in the *Imam*-path, $\mathbf{r}_2(\lambda_{\Gamma_4^-}, \lambda_{X_1^-}, \lambda_{X_4^+})$. First of all, the cases in which only a single mode exists are considered, i.e.,$\mathbf{r}_2(\lambda, 0, 0)$, $\mathbf{r}_2(0, \lambda, 0)$, and $\mathbf{r}_2(0, 0, \lambda)$ with λ from -1 to $+1$. In Fig. 3.3, the changes of the energy, polarization, and magnetic moments of Cu-MOF with respect to each distortion mode are shown. The first row of Fig. 3.3 shows changes in energy. X_1^- and X_4^+ modes are unstable modes which means that the mode reduces the energy of the system, i.e., the system is stabilized. But the Γ_4^- mode is a stable mode that raises the energy. The second row shows the electric polarization. Polar mode Γ_4^- induces the electric polarization linear to the mode as shown in Fig. 3.3 (d). However, its sign is opposite to the polarization of the final $Pna2_1$ structure [Fig. 3.2

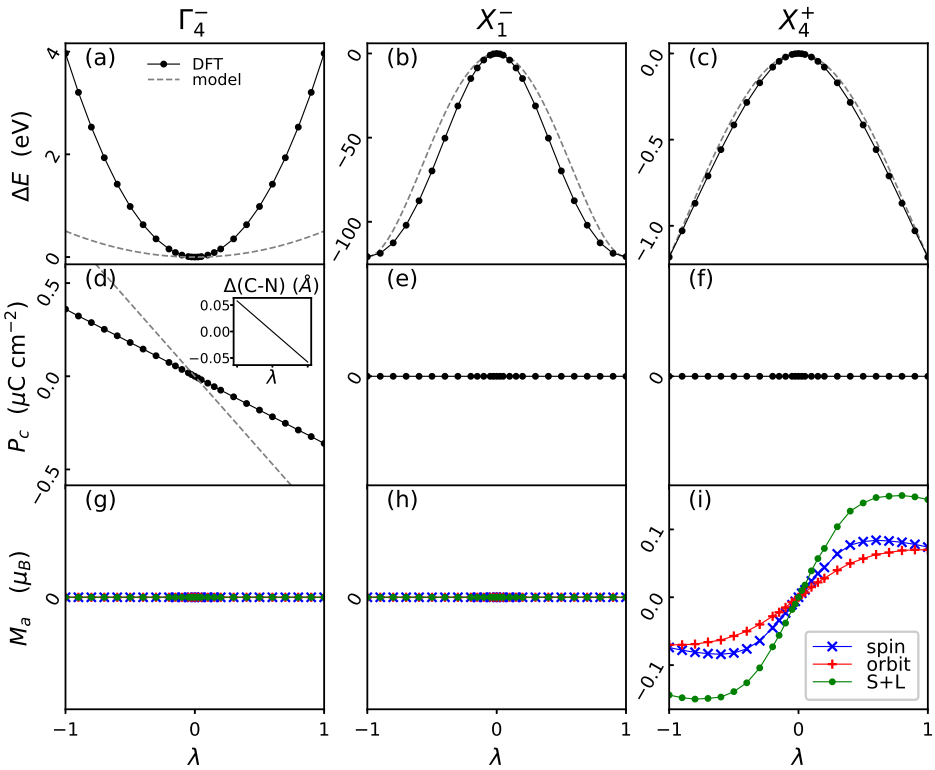

Figure 3.3 (a-c) Change of energy, (d-f) electric polarization, and (g-i) magnetic moments of Cu-MOF when only one of distortion mode among Γ_4^-, X_1^-, and X_4^+ exists. Each of the columns is the quantities changing with respect to the distortion mode labeled by the irrep on top of the column. In (a-d), quantities obtained from the free energy model are shown in the grey dashed lines. Inset in (d) is the C-N bond length difference of the Gua ion Δ(C-N) $= l^{\text{C-N}}_{\text{lower}} - l^{\text{C-N}}_{\text{upper}}$.

(b)]. This discrepancy led us to further investigations. On the other hand, non-polar mode X_1^- and X_4^+ do not induce polarization. The last row shows the magnetic moments. Only the X_4^+ mode representing the JT distortion induces a non-zero total magnetic moment [Fig. 3.3 (i)]. It means that the spin canting is coupled with the JT phase.

Motivated by the discrepancy in polarization, in the following step, we examined the paths defined by more than one mode. In particular, the structure

path from $(\lambda_{\Gamma_4^-}, \lambda_{X_1^-}, \lambda_{X_4^+}) = (0, -1, -1)$ to $(0, 1, 1)$ and from $(0, 1, 1)$ to $(\pm 1, 1, 1)$ are examined. The former represents the hybrid mode $X_1^- \oplus X_4^+$. The latter represents the addition of the polar mode Γ_4^- in the proper direction $(+1)$ and the inverted direction (-1). The results are shown in Fig. 3.4 with the parameter λ_1 for $X_1^- \oplus X_4^+$ mode and $\pm\lambda_2$ for $\pm\Gamma_4^-$ mode. The energy of the system decreases by the combination of two unstable modes, $X_1^- \oplus X_4^+$, as shown in Fig. 3.4 (a). The change in energy is symmetric between the positive and negative sides of λ_1. In the presence of the $X_1^- \oplus X_4^+$ modes, Γ_4^- mode, which was a stable mode in the absence of it, now reduces the energy [Fig. 3.4 (b)]. It defines the HIFE, i.e., polar Γ_4^- mode appears via the coupling with the $X_1^- \oplus X_4^+$ hybrid mode [26]. On the other hand, the inverted Γ_4^- mode increases the energy. It implies that $\mathbf{r}_2(1, 1, 1)$ and $\mathbf{r}_2(-1, 1, 1)$ structures are neither energetically equivalent nor related by symmetry. In fact, $\mathbf{r}_2(\lambda, 1, \lambda)$ structure in the $Imam$-path corresponds to $\mathbf{r}_1(\lambda)$ structure of $Pnan$-path, i.e., in addition to the Γ_4^-, X_4^+ mode also has to be inverted to obtain $\mathbf{r}_1(-\lambda)$. This is an important feature of the HIFE mechanism [34].

Interestingly, the $X_1^- \oplus X_4^+$ hybrid mode, which consists of two non-polar modes, induces electric polarization even without the polar Γ_4^- mode as shown in Fig. 3.4 (c). At first glance, this seems to be a contradiction. However, since the symmetry of the system becomes the polar space group $Pna2_1$ by the $X_1^- \oplus X_4^+$ hybrid mode, this does not violate the symmetry. The polarization is also symmetric between the positive and negative sides of λ_1. It means that the polarization is not switched when we switch both of the X_1^- and X_4^+ modes, as HIFE mechanism argues [34]. As shown in Fig. 3.4 (d), linear behavior and the sign of the additional polarization by $\pm\Gamma_4^-$ mode is consistent with the Γ_4^- mode only case [Fig. 3.3 (d)]. Γ_4^- mode induces the polarization opposite to

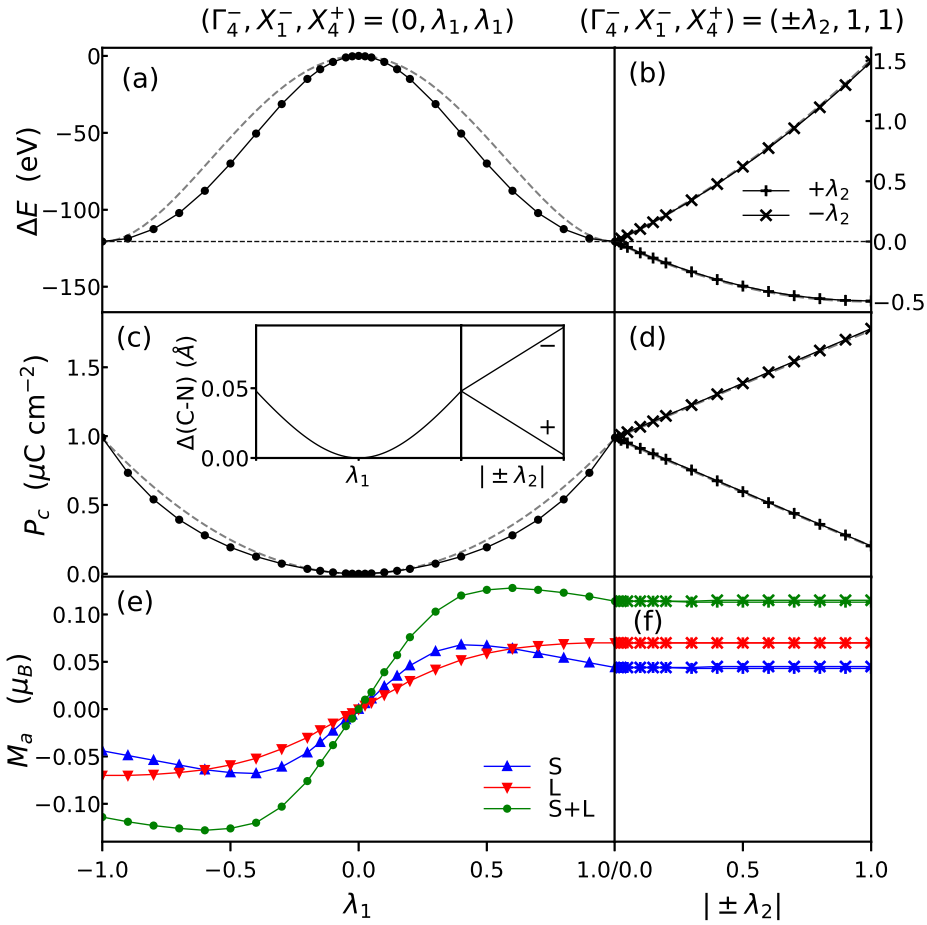

Figure 3.4 (a,b) Change of energy, (c,d) electric polarization, and (e,f) magnetic moments of Cu-MOF along the parameter path $(\lambda_{\Gamma_4^-}, \lambda_{X_1^-}, \lambda_{X_4^+}) = (0, \lambda_1, \lambda_1)$ and $(\lambda_{\Gamma_4^-}, \lambda_{X_1^-}, \lambda_{X_4^+}) = (\pm\lambda_2, 1, 1)$. Be aware of the difference in the axis scale between (a) and (b). Inset in (c) is the C-N bond length difference of the Gua ion Δ(C-N). Gray lines which show the free energy model derived values are perfectly overlapped with the DFT value in (b) and (d).

the total polarization, i.e., the main contribution of the electric polarization is $X_1^- \oplus X_4^+$ hybrid mode and polar Γ_4^- mode rather reduces it, thus resolving the discrepancy. It leads to an interesting result, the inversion of the polar Γ_4^- mode does not invert the electric polarization but rather enhances it. We confirmed the same properties in the Cr-MOF.

Magnetic moments by the $X_1^- \oplus X_4^+$ mode shown in Fig. 3.4 (e) exhibit a similar tendency with the X_4^+ mode only case. The spin magnetic moment is slightly reduced in the presence of X_1^- mode. Γ_4^- mode has no effect on the magnetic moment [Fig. 3.4 (f)].

4 Electronic Properties

In this chapter, we analyze the counterintuitive ferroelectric properties shown in the previous chapter and propose a model that is consistent with the DFT results.

4.1 Origin of Counterintuitive Polarization

As we saw from the DFT results, a combination of the two non-polar modes (hybrid mode) induces polarization. In this section, we will characterize it and explore its origin. Since the hybrid mode consists of the two non-polar modes X_1^- and X_4^+, there is no core contribution to the polarization, i.e., the polarization is purely electronic. The core contribution comes from a change in the dipole moment of the nuclei, which is written as Eq. (2.32), with respect to the reference structure. By definition, an atomic displacement in each non-polar mode has a counterpart, or counterparts, which cancels out each other so that their summation becomes non-polar. This is still true even when two non-polar modes coexist. As a result, only the electronic contribution remains in the sole presence of the hybrid mode. By contrast, polar Γ_4^- mode has both core and electronic contributions.

In fact, purely electronic polarization has been known from an early study on HIFE. The perovskite $LaGaO_3/YGaO_3$ superlattice is an inorganic HIFE

material. It was reported that a small polarization is induced even without the polar distortion but in the presence of the two non-polar modes, i.e., a purely electronic polarization [35]. Including this case and the Cr-/Cu-MOF cases, in HIFE materials, the space group is already polar when the two non-polar modes coexist [34, 35]. Therefore, the purely electronic polarization arising from the structural asymmetry can be thought of as a general property of the HIFE.

Next, let us examine the microscopic origin of the purely electronic polarization in Cr-/Cu-MOFs. Tian, *et al.*, showed how the Gua ions induce polarization in the viewpoint of the Lewis formalism [29]. A Gua^+ ion has one double bond out of three carbon-nitrogen (C-N) bonds as a resonance structure. A localized positive charge is considered at the N connected by the double bond. In this picture, the shorter bond takes the higher probability that the double bond is placed at it. As a result, the C-N bond length difference of the Gua ion induces polarization. The microscopic origin of the purely electronic polarization is also attributed to this mechanism. The bond length difference between the Gua's lower and upper C-N bonds with respect to c-axis, $\Delta(\text{C-N}) = l^{\text{C-N}}_{\text{lower}} - l^{\text{C-N}}_{\text{upper}}$, is consistent with the polarization. The Δ(C-N) is shown in the inset of Fig. 3.4 (c). Two bonds are equivalent in the $Imam$ phase, so the system is non-polar. In the presence of the distortion, the Δ(C-N) is nearly quadratic and symmetric to λ_1 and linear to λ_2. It is exactly the characteristic of the corresponding polarization. Moreover, the same is also true for the Γ_4^- mode-only case, in which the Δ(C-N) is shown in the inset of Fig. 3.3 (d). It is natural that the Γ_4^- mode is stable when it increases and, to the contrary unstable when it reduces, Δ(C-N) because too large Δ(C-N) must be energetically unfavored.

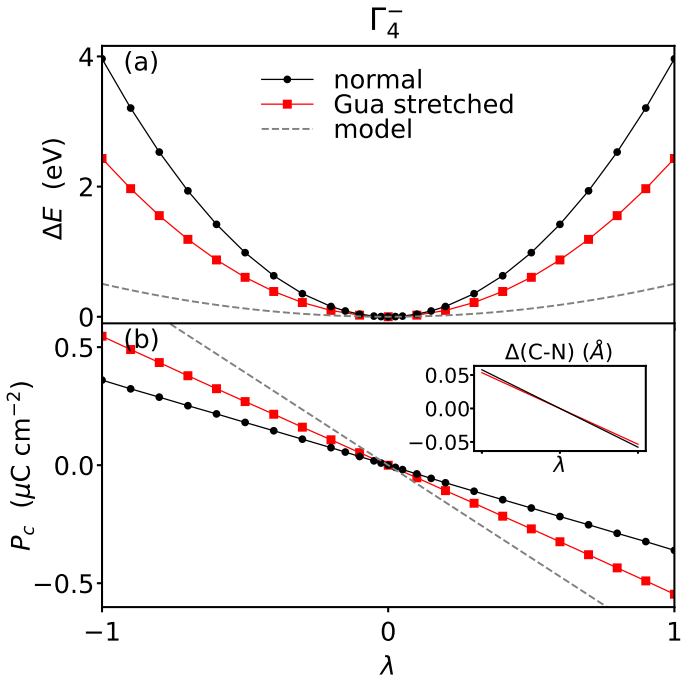

Figure 4.1 Change of (a) energy and (b) polarization by Γ_4^- mode when the bond lengths of Gua of the Cu-MOF ion are stretched (red lines). This corresponds to Fig. 3.3 (a) and (d) and the data therein are shown again for comparison.

On the other hand, in the Γ_4^- mode-only case in which $\lambda_{X_1^-} = 0$, we have to carefully consider the unnaturally short bonds of Gua ion. Since the symmetry operation-based method searching for the pseudo symmetry structure is weak at capturing the rotation of molecules, the bond lengths of Gua are significantly shortened in the *Imam* structure. This must have affected the polarization involved with Δ(C-N). We examined the cases in which the bond lengths of Gua are stretched to reasonable values. Such Gua structure was adopted from the Supporting Information of the Ref. [26]. Gua stretching in the *Imam* structure corresponds to Γ_1^+ mode, which leaves the symmetry of the system unchanged. It decreases the energy by about 71.17 eV per unit cell with respect

to the unstretched case, which is almost half the energy change by the Gua rotating X_1^- mode. The Γ_4^- mode with the stretched Gua bond length results in smaller energy change and larger polarization as shown by the red lines in Fig. 4.1 (a) and (b), but does not alter the tendencies. This is consistent with the fact that the polarization is closely related to the Gua ions: The larger the distance, the larger the dipole moment.

In either X_1^- or X_4^+ mode-only cases, Δ(C-N) remains zero. Each of these modes contains the alternating rotation of Gua ions, rotation around b-axis by X_1^- mode and around c-axis by X_4^+. Note that they are not ideal rotations, so the bond lengths change. By single non-polar mode, N atoms move symmetrically with respect to the C atom, so the Δ(C-N) is unchanged. However, if two modes coexist, the combined displacement of N is no longer symmetric to the C atom as depicted in Fig. 4.2 (a). As a result, Δ(C-N) becomes finite. In this way, the combination of the two non-polar modes can give rise to a polar space group.

We further analyze the purely electronic polarization by the $X_1^- \oplus X_4^+$ mode. The HIFE mechanism states that the switching of either X_1^- or X_4^+ mode, but not both, inverts polarization. Ref. [34] exhibits that the presence of the hybrid mode softens the polar mode. But they also suggested the possibility of the ferroelectric state by the hybrid mode only. We calculate the polarization without the polar Γ_4^- mode in the $(\lambda_{\Gamma_4^-}, \lambda_{X_1^-}, \lambda_{X_4^+}) = (0, \lambda, 1)$ and $(0, 1, \lambda)$ paths as shown in Fig. 4.2 (b) and (c), respectively. In both cases, the polarization is inverted by switching one of the non-polar modes. Again, Δ(C-N) is consistent with the polarization in these cases. On the other hand, Fig. 3.4 (c) already showed that the switching of both modes does not invert the polarization. These observations imply that the purely electronic polarization without the polar Γ_4^-

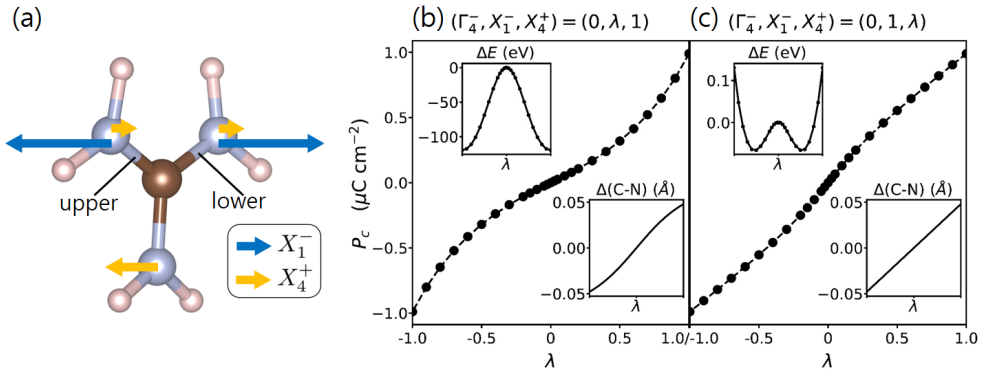

Figure 4.2 (a) Schematic picture of the displacements of N atoms relative to the C atom in Gua of the Cu-MOF by the X_1^- and X_4^+ modes. Polarization without Γ_4^- mode in the (b) $(\lambda_{\Gamma_4^-}, \lambda_{X_1^-}, \lambda_{X_4^+}) = (0, \lambda, 1)$ path and (c) $(\lambda_{\Gamma_4^-}, \lambda_{X_1^-}, \lambda_{X_4^+}) = (0, 1, \lambda)$ path. In (b) and (c), upper insets are energy changes, and lower insets are the C-N bond length difference of the Gua ion Δ(C-N).

mode is attributed to the HIFE mechanism. The same argument is also applied to the freezing of the Γ_4^- mode, i.e., the structures energetically equivalent to $\mathbf{r}_2(1,1,1)$ are $\mathbf{r}_2(-1,-1,1)$, $\mathbf{r}_2(-1,1,-1)$, and $\mathbf{r}_2(1,-1,-1)$. Then we can say that two *distinct* physical quantities, the purely electronic polarization and the polar distortion Γ_4^- mode, are simultaneously coupled with two non-polar modes X_1^- or X_4^+.

4.2 Free Energy Model

The coupling between the polarization and the distortion mode can be represented by Landau theory [47]. As discussed in Sec. 2.2.1, for the HIFE mechanism in Cr-/Cu-MOFs, polarization P dependent part of the free energy is written as $F(P) = \alpha P^2 + \gamma Q_{X_1^-} Q_{X_4^+} P$. However, the spontaneous polarization written as $P = -\gamma Q_{X_1^-} Q_{X_4^+}/2\alpha$ does not fully explain the DFT results. Usually, the way of showing HIFE is to show that the polar mode amplitude

corresponding to the total energy minimum gradually increases as the hybrid mode amplitude increases [34]. In fact, this can only prove the appearance of the polar mode by the hybrid mode. The spontaneous polarization above is consistent with this way only when we assume an intuitive picture where the polarization is proportional to the polar mode. However, our DFT results violate this intuitive picture.

To resolve this situation, we construct the free energy for Cr-/Cu-MOFs in which the polarization P and the polar Γ_4^- mode are described separately. Because the polarization and the polar distortion mode respect the same symmetry, both of them can have terms of the same order. In addition, a linear coupling of them $PQ_{\Gamma_4^-}$ can be included, which actually has the same symmetry as P^2. The P and $Q_{\Gamma_4^-}$ dependent part of the free energy is

$$\begin{aligned} F(P, Q_{\Gamma_4^-}) = \alpha P^2 + \alpha' Q_{\Gamma_4^-}^2 + \beta P Q_{\Gamma_4^-} \\ + \gamma Q_{X_1^-} Q_{X_4^+} P + \gamma' Q_{X_1^-} Q_{X_4^+} Q_{\Gamma_4^-} \end{aligned} \tag{4.1}$$

where $\alpha > 0$ and $\alpha' > 0$ are assumed. In addition to the P dependent terms, the free energy also includes the elastic energies of the non-polar modes, which we will consider in the later section. The spontaneous polarization is

$$P^* = -\frac{\beta}{2\alpha} Q_{\Gamma_4^-} - \frac{\gamma}{2\alpha} Q_{X_1^-} Q_{X_4^+}. \tag{4.2}$$

The first term newly appears compared to the usual formula. If $\beta > 0$, $\gamma < 0$, and $\beta/\alpha < -\gamma/\alpha$, the DFT results in Fig. 3.3 (d) and Fig. 3.4 (c,d) can be explained, i.e., P^* is linear to $Q_{\Gamma_4^-} \sim \lambda_{(2)}$ and quadratic to λ_1 ($Q_{X_1^-} Q_{X_4^+} \sim \lambda_1^2$). If we replace the P in Eq. (4.1) with the Eq. (4.2), we can check the polar

mode dependence of the free energy,

$$
\begin{aligned}
F(Q_{\Gamma_4^-}) = & -\frac{\gamma^2}{4\alpha}(Q_{X_1^-}Q_{X_4^+})^2 \\
& + (\gamma' - \frac{\beta\gamma}{2\alpha})Q_{X_1^-}Q_{X_4^+}Q_{\Gamma_4^-} + (\alpha' - \frac{\beta^2}{4\alpha})Q^2_{\Gamma_4^-}.
\end{aligned}
\tag{4.3}
$$

When $(\gamma' - \beta\gamma/2\alpha) < 0$ and $(\alpha' - \beta^2/4\alpha) > 0$, freezing of the Γ_4^- mode shown in Fig. 3.4 (b) is also reproduced. Finally, the total energies and polarization derived from the model with fitted parameters obtained at the later sections 4.3 and 4.4 are shown together in Fig. 3.3 and 3.4 by gray dashed lines, which are well consistent with the DFT result.

This model would provide a hint for manipulating the order parameters of Cr-/Cu-MOFs. For example, since what directly couples with the electric field is P, the coupling between the polar mode and the field might be renormalized. In contrast, manipulation of a non-polar mode, for example, by strain, may directly affect polarization, not via the polar mode.

As a summary, let us construct a detailed argument on the HIFE and magneto-electric coupling in the Cr-/Cu-MOF. The polarization can be decomposed into two parts, the hybrid mode ($X_1^- \oplus X_4^+$) part and the polar mode (Γ_4^-) part. From the *Imam* structure, $X_1^- \oplus X_4^+$ mode first appears and induces both the WFM and electric polarization. Next, the Γ_4^- mode appears to compensate for the polarization partially and further stabilize the energy. This is why reversing the polar mode rather enhances the polarization. Δ(C-N) is a key parameter in this mechanism. The X_4^+ mode clearly explains the magneto-electric coupling observed by experiments [29] because both electric and magnetic properties vary with X_4^+ mode. We will show in the later chapter that the orbital angular momentum is explicitly coupled with the JT distortion represented by X_4^+ mode.

4.3 Determination of Model Parameters

This section shows the determination of the coefficients of the free energy model defined in the previous section, Eq. (4.1), for the Cu-MOF. To determine the values of the parameters in free energy, let us set rules for the units. (1) The free energy is measured in eV per unit cell. For simplicity, we use the DFT total energy values as free energy. (2) Polarization is written as the polarization density in the μC/cm^2 unit. (3) Distortion mode amplitudes are replaced with the dimensionless ratio normalized to their values in equilibrium in $Pna2_1$ structure, i.e., Q_X becomes equivalent to λ_X. For the Γ_4^- mode related parameters, two different data can be used to determine the same parameters, from $(\lambda_{\Gamma_4^-}, \lambda_{X_1^-}, \lambda_{X_4^+}) = (\lambda, 0, 0)$ path and from $(\lambda_{\Gamma_4^-}, \lambda_{X_1^-}, \lambda_{X_4^+}) = (\lambda, 1, 1)$ path. However, the resulting parameters from the two data are incompatible. In such cases, we choose the data from the structure which is closer to the equilibrium $Pna2_1$ structure, i.e., $(\lambda, 1, 1)$ path. Instead, this choice brings about a relatively large error in $(\lambda, 0, 0)$ path shown in Fig. 3.3 (a) and (d), which must be the effect of the higher order terms in the free energy neglected from the model.

From the polarization values, we get

$$-\frac{\gamma}{2\alpha} = 0.99\ \mu C/\text{cm}^2 \tag{4.4}$$

with $(\lambda_{\Gamma_4^-}, \lambda_{X_1^-}, \lambda_{X_4^+}) = (0, \lambda, \lambda)$ path of Fig. 3.4 (c) and

$$-\frac{\beta}{2\alpha} = -0.79\ \mu C/\text{cm}^2 \tag{4.5}$$

with $(\lambda_{\Gamma_4^-}, \lambda_{X_1^-}, \lambda_{X_4^+}) = (\lambda, 1, 1)$ path of Fig. 3.4 (d). From the energy change in $(\lambda_{\Gamma_4^-}, \lambda_{X_1^-}, \lambda_{X_4^+}) = (\lambda, 1, 1)$ path of Fig. 3.4 (b), we get

$$\begin{aligned} (\gamma' - \frac{\beta\gamma}{2\alpha}) + (\alpha' - \frac{\beta^2}{4\alpha}) &= -0.493470 \text{ eV} \\ -(\gamma' - \frac{\beta\gamma}{2\alpha}) + (\alpha' - \frac{\beta^2}{4\alpha}) &= 1.49337 \text{ eV}. \end{aligned} \tag{4.6}$$

However, we have four equations for five parameters. It is impossible to determine the parameters from the given data.

Instead, we estimate the α value from the separate calculations. The α represents the energy from the polarization, and it is highly attributed to Gua ions. Therefore, we estimate α by applying external electric field $\mathcal{E}$ to isolated symmetric Gua$^+$ ions and calculating the energy and induced dipole moment p. In the calculation by using VASP, an external electric field is added by sawtooth-type potential, and the +1 oxidation number is realized by reducing one electron with the NELECT option. The energy of such system depending on p and $\mathcal{E}$ is written as $E(p, \mathcal{E}) = ap^2 - p\mathcal{E}$. By fitting to the calculated values shown in Fig. 4.3, we obtain $a = 1.175$ eV/(eÅ)^2. Because Cr-/Cu-MOF has four Gua$^+$ ions in a unit cell, the relation between a and α can be given as $\alpha(p/v)^2 = 4ap^2$ where $v = 873.522$ Å^3 is the volume of the unit cell. As a result, we get

$$\begin{aligned} \alpha &= 1.40 \text{ (eV}/[\mu C/\text{cm}^2]^2) \\ \alpha' &= 1.37 \text{ (eV)} \\ \beta &= 2.20 \text{ (eV}/[\mu C/\text{cm}^2]) \\ \gamma &= -2.76 \text{ (eV}/[\mu C/\text{cm}^2]) \\ \gamma' &= -3.17 \text{ (eV)}. \end{aligned} \tag{4.7}$$

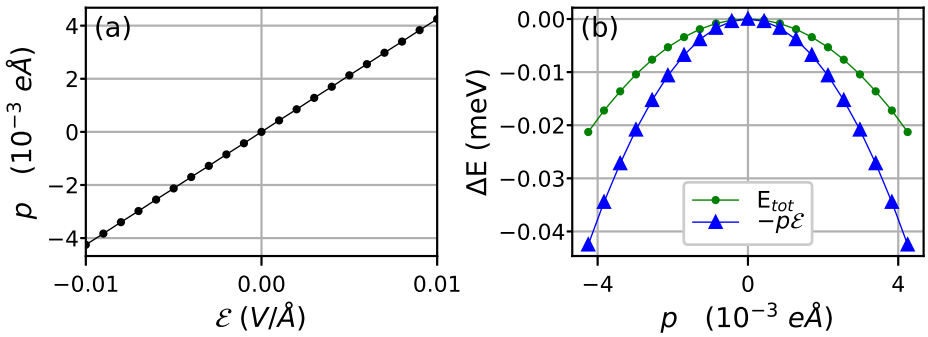

Figure 4.3 (a) Induced dipole moment in isolated Gua$^+$ ion by external electric field $\mathcal{E}$. (b) Total energy change and dipole-field interaction energy.

4.4 Estimation of Ferroelectric Switching Field

In the presence of the external field h, free energy for a second order phase transition as a function of order parameter x can be written as $f(x) = \alpha x^2 + \beta x^4 - xh$, where $\alpha < 0$ and $\beta > 0$. When this free energy has minima $-y_0$ at $\pm x_0$, $\alpha = -2y_0/x_0^2$, $\beta = y_0/x_0^4$, and the switching field strength is $|h_c| = 4|\alpha|^{3/2}/(3\sqrt{6\beta}) = 8y_0/(3\sqrt{3}x_0)$. In this way, we will estimate the field strength needed to switch the polarization of Cu-MOF. However, note that this approach is very simplified, neglecting the possible complex deformations of Gua ions. It also assumes ordered Gua ions rather than thermally disordered configuration.

The free energy of the Cu-MOF including external electric field $\mathcal{E}$ is

$$F(P, Q_{\Gamma_4^-}, \mathcal{E}') = \alpha P^2 + \alpha' Q_{\Gamma_4^-}^2 + \beta P Q_{\Gamma_4^-} + \gamma Q_{X_1^-} Q_{X_4^+} P + \gamma' Q_{X_1^-} Q_{X_4^+} Q_{\Gamma_4^-} - P\mathcal{E}', \tag{4.8}$$

where $\mathcal{E}' = v\mathcal{E}$. Note that only P couples directly with $\mathcal{E}$. The resultant polarization is

$$P^* = -\frac{\beta}{2\alpha} Q_{\Gamma_4^-} - \frac{\gamma}{2\alpha} Q_{X_1^-} Q_{X_4^+} + \frac{1}{2\alpha}\mathcal{E}'. \tag{4.9}$$

When it is substituted to Eq. (4.8),

$$F(P^*, Q_{\Gamma_4^-}, \mathcal{E}') = -\frac{\gamma^2}{4\alpha}(Q_{X_1^-}Q_{X_4^+})^2 + (\gamma' - \frac{\beta\gamma}{2\alpha})Q_{X_1^-}Q_{X_4^+}Q_{\Gamma_4^-} + (\alpha' - \frac{\beta^2}{4\alpha})Q^2_{\Gamma_4^-} + \frac{\gamma}{2\alpha}Q_{X_1^-}Q_{X_4^+}\mathcal{E}' + \frac{\beta}{2\alpha}Q_{\Gamma_4^-}\mathcal{E}' - \frac{1}{4\alpha}\mathcal{E}'^2. \tag{4.10}$$

Let us assume that $Q_{\Gamma_4^-}$ is determined by the given $Q_{X_1^-}$ and $Q_{X_4^+}$,

$$Q^*_{\Gamma_4^-} = -\frac{(\gamma' - \frac{\beta\gamma}{2\alpha})}{2(\alpha' - \frac{\beta^2}{4\alpha})}Q_{X_1^-}Q_{X_4^+} - \frac{\beta}{4\alpha(\alpha' - \frac{\beta^2}{4\alpha})}\mathcal{E}' \equiv \frac{E_1}{2E_2}Q_{X_1^-}Q_{X_4^+} - \frac{P_2}{2E_2}\mathcal{E}', \tag{4.11}$$

where $P_1 \equiv -\frac{\gamma}{2\alpha}$, $P_2 \equiv \frac{\beta}{2\alpha}$, $E_1 \equiv -(\gamma' - \frac{\beta\gamma}{2\alpha})$, and $E_2 \equiv (\alpha' - \frac{\beta^2}{4\alpha})$. It is then inserted into Eq. (4.10).

$$F(P^*, Q^*_{\Gamma_4^-}, \mathcal{E}') \equiv \mathcal{A}(Q_{X_1^-}Q_{X_4^+})^2 + \mathcal{B}Q_{X_1^-}Q_{X_4^+}\mathcal{E}' + \mathcal{C}\mathcal{E}'^2, \tag{4.12}$$

where

$$\begin{aligned} \mathcal{A} &= -\alpha P_1^2 - \frac{E_1^2}{4E_2} = -1.86 \text{ eV} \\ \mathcal{B} &= -P_1 + \frac{E_1 P_2}{2E_2} = -0.21\ \mu C/\text{cm}^2 \\ \mathcal{C} &= -\frac{P_2^2}{4E_2} - \frac{1}{4\alpha} = -0.49\ [\mu C/\text{cm}^2]^2/\text{eV}. \end{aligned} \tag{4.13}$$

It implies that non-polar modes $Q_{X_1^-}$ and $Q_{X_4^+}$ are also indirectly coupled with the external field and each other by the HIFE mechanism.

In order to determine the switching field strength, elastic energy contributions from the non-polar modes are considered.

$$F_{\text{non-polar}}(Q_{X_1^-}, Q_{X_4^+}) = \eta Q^2_{X_1^-} + \eta' Q^2_{X_4^+} + \lambda Q^4_{X_1^-} + \lambda' Q^4_{X_4^+} + \xi Q^2_{X_1^-}Q^2_{X_4^+}, \tag{4.14}$$

where $\eta, \eta' < 0$ and $\lambda, \lambda' > 0$. The ξ represents an elastic coupling between $Q_{X_1^-}$ and $Q_{X_4^+}$. When P^* and $Q^*_{\Gamma_4^-}$ are determined by $Q_{X_1^-}$ and $Q_{X_4^+}$, total free energy is

$$\begin{aligned} F(Q_{X_1^-}, Q_{X_4^+}, \mathcal{E}') = \eta Q^2_{X_1^-} + \eta' Q^2_{X_4^+} + \lambda Q^4_{X_1^-} + \lambda' Q^4_{X_4^+} \\ + (\xi + \mathcal{A}) Q^2_{X_1^-} Q^2_{X_4^+} + \mathcal{B} Q_{X_1^-} Q_{X_4^+} \mathcal{E}' + \mathcal{C}\mathcal{E}'^2. \end{aligned} \tag{4.15}$$

Let us denote the total energy of the system with the structure given by $(Q_{\Gamma_4^-}, Q_{X_1^-}, Q_{X_4^+})$ as $E(Q_{\Gamma_4^-}, Q_{X_1^-}, Q_{X_4^+})$.

$$\begin{aligned} \eta + \xi + \mathcal{A} = -2E_3 \\ \lambda = E_3, \end{aligned} \tag{4.16}$$

where $E_3 \equiv E(0,0,1) - E(1,1,1) = 119.943874\ eV$. Note that when $Q_{X_1^-} = 0$ or $Q_{X_4^+} = 0$, $Q^*_{\Gamma_4^-} = 0$.

$$\begin{aligned} \eta' + \xi + \mathcal{A} = -2E_4 \\ \lambda' = E_4, \end{aligned} \tag{4.17}$$

where $E_4 \equiv E(0,1,0) - E(1,1,1) = 0.362790 eV$.

$$\eta + \eta' + \lambda + \lambda' + \xi + \mathcal{A} = -E_5 \equiv -(E(0,0,0) - E(1,1,1)) = \ -121.125702 eV \tag{4.18}$$

As a result,

$$\begin{aligned} \lambda &= 120 \text{ eV} \\ \lambda' &= 0.36 \text{ eV} \\ \eta &= -241 \text{ eV} \\ \eta' &= -1.54 \text{ eV} \\ \xi &= 2.68 \text{ eV} \end{aligned} \tag{4.19}$$

One can see that the coefficients for X_1^- mode (η and λ) are much larger than others. Therefore, it would be desirable to consider the FE switching of $Q_{X_4^+}$ mode, whereas we can assume the fixed value of $Q_{X_1^-} = 1$ during the FE switching. Furthermore, it switches both the polarization and magnetic moment. Free energy as a function of $Q_{X_4^+}$ is

$$F(Q_{X_4^+}) = (\eta' + \xi + \mathcal{A})Q_{X_4^+}^2 + \lambda' Q_{X_4^+}^4 + \mathcal{B}\mathcal{E}' Q_{X_4^+} \tag{4.20}$$

The switching field strength can be obtained by the following.

$$\begin{aligned} |\mathcal{B}|v|\mathcal{E}_c| &= \frac{4}{3}|\eta' + \xi + \mathcal{A}|^{\frac{3}{2}} \frac{1}{\sqrt{6\lambda}} = \frac{8}{3\sqrt{3}} E_4 \\ |\mathcal{E}_c| &= \frac{8E_4}{3\sqrt{3}v|\mathcal{B}|} = 4.95 \text{ V/Å} \end{aligned} \tag{4.21}$$

We can compare this with the value from a much simpler approach, which considers the polarization P as a primary order parameter. In this case, we can use the parameters from the $Pnan$-path. The free energy gain at the equilibrium value of the polarization $P_0 = 0.21\ \mu C/\text{cm}^2$ is $E_{Pnan} = 0.363556$ eV.

$$|\mathcal{E}_c^{\text{simple}}| = \frac{8E_{Pnan}}{3\sqrt{3}vP_0} = 4.95 \text{ V/Å} \tag{4.22}$$

It is the same as $|\mathcal{E}_c|$ within the digits we are showing. In the ideal case, when both two non-polar modes $Q_{X_4^+}$ and $Q_{X_1^-}$ are 1, the equilibrium value of the $Q^*_{\Gamma_4^-}$ without an external field should be 1. Eq. (4.11) implies that $E_1 = 2E_2$ is the condition for the ideal case. This leads to $\mathcal{B} = -P_1 + P_2 = -P_0$ since both $P_1 - P_2$ and P_0 are the polarization of stable structure $\mathbf{r}_1(1) = \mathbf{r}_2(1,1,1)$. Moreover, $E_{Pnan} \approx E_4$ since $\mathbf{r}_1(0) \approx \mathbf{r}_2(0,1,0)$. Thus, two expressions are equivalent in these assumptions. Note that when η and λ are comparable to η' and λ', which means releasing the assumption $Q_{X_1^-} = 1$, switching field estimation can differ from that of the simple approach. On the other hand,

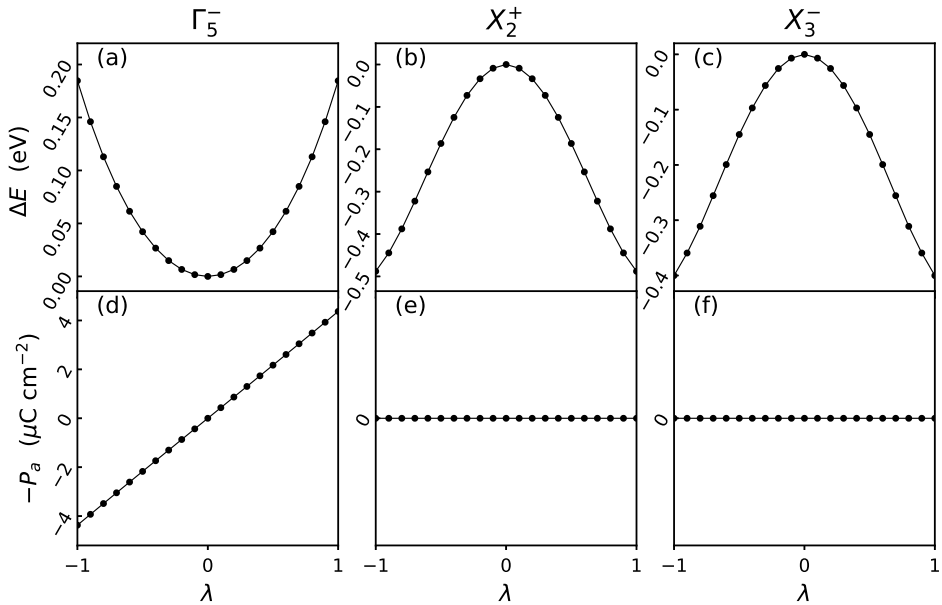

Figure 4.4 The case of $Ca_3Mn_2O_7$. (a-c) Change of energy and (d-f) electric polarization when only one distortion mode among Γ_5^-, X_2^+, and X_3^- exists.

the above field strengths are too large to be realized. Therefore, polarization switching by an external electric field will be impossible in practice.

4.5 Revisit of Inorganic Perovskite $Ca_3Mn_2O_7$

We can examine how the HIFE in MOFs and that in inorganics differ. For this purpose, we revisited the prototypical inorganic perovskite HIFE material, Ruddlesden-Popper $Ca_3Mn_2O_7$ [34], in the viewpoint of the free energy model we constructed in Sec. 4.2. For the DFT calculations of $Ca_3Mn_2O_7$, we adopt PBEsol+U functional and $4 \times 4 \times 4$ k-space grid within the primitive cell. Since we focus on the electric property, SOC is neglected. Other DFT parameters are the same as ref. [34]. The polar structure and the corresponding non-polar structure have $A2_1am$ and $I4/mmm$ space groups, respectively. These

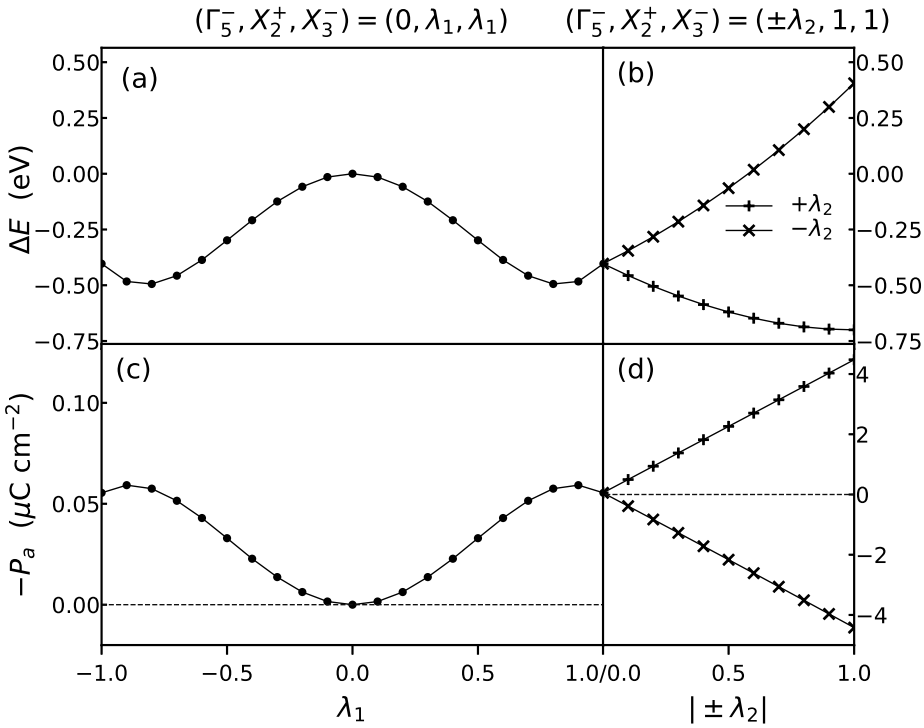

Figure 4.5 The case of $Ca_3Mn_2O_7$. (a,b) Change of energy and (c,d) electric polarization along the parameter path $(\lambda_{\Gamma_5^-}, \lambda_{X_2^+}, \lambda_{X_3^-}) = (0, \lambda_1, \lambda_1)$ and $(\lambda_{\Gamma_5^-}, \lambda_{X_2^+}, \lambda_{X_3^-}) = (\pm\lambda_2, 1, 1)$. Be aware of the difference in the axis scale between (c) and (d).

structures are connected by three distortion modes labeled by irreps Γ_5^-, X_2^+, and X_3^-. Γ_5^- mode is an alternating displacements of A-site Ca^{2+} cations along the a-direction, thus inducing a polarization in the a-direction. X_2^+ and X_3^- modes are related to the rotation and tilt of the oxygen octahedra, respectively. For the $A2_1am$ structure, experimental conventional cell lattice constants $a = 5.2347$ Å, $b = 5.2421$ Å, and $c = 19.4177$ Å are adopted [67]. For the $I4/mmm$ structure, DFT optimized lattice constant $a = b = 5.2320$ Å and the same c as $A2_1am$ structure are adopted. We assumed the linear interpolation of a (b) with respect to the Γ_5^- (X_3^-) mode.

In Fig. 4.4 and 4.5, the total energy and polarization of $Ca_3Mn_2O_7$ with respect to the distortion modes are shown. In Fig. 4.4, each single-mode-only case shows the same behavior as the Cu-MOF case shown in Fig. 3.3. The polar mode Γ_5^- is stable and induces polarization. Two non-polar modes, X_2^+ and X_3^-, are unstable and induce no polarization. Fig. 4.5, which shows the effect of the hybrid mode $X_2^+ \oplus X_3^-$, reveals the differences from Cu-MOF shown in Fig. 3.4. The behavior of the total energy is similar. However, the hybrid mode induces only a small portion of the total polarization, which is smaller by two orders in comparison to the polar mode. In addition, the direction of the polarization by the hybrid mode and polar mode are the same. Thus, the switching of the polar mode inverts the sign of total polarization. One can say that the polarization of the $Ca_3Mn_2O_7$ behaves in an 'intuitive' way. On the other hand, a large purely electronic polarization can be thought of a unique feature of the HIFE in MOFs. These differences can be attributed to the difference between organic and inorganic natures, or covalence and ionic natures.

The viewpoint of the Landau theory provides a systematic comparison. The parameters of the free energy described in the form of Eq. (4.1) for the $Ca_3Mn_2O_7$ are determined in the same way except for α. The α is determined by applying the external electric field to the crystal up to ± 0.001 V/Å via the method of Nunes and Gonze [68]. Note that this method could not be applied for Cu-MOF due to a convergence issue. The obtained parameters are

as follows.

$$
\begin{aligned}
\alpha &= 1.62 \times 10^{-3}\ (\mathrm{eV}/[\mu C/\mathrm{cm}^2]^2) \\
\alpha' &= 2.88 \times 10^{-1}\ (\mathrm{eV}) \\
\beta &= 1.43 \times 10^{-2}\ (\mathrm{eV}/[\mu C/\mathrm{cm}^2]) \\
\gamma &= 1.80 \times 10^{-4}\ (\mathrm{eV}/[\mu C/\mathrm{cm}^2]) \\
\gamma' &= -5.52 \times 10^{-1}\ (\mathrm{eV}).
\end{aligned}
\tag{4.23}
$$

The β and γ represent the scales of the polarization induced by the polar mode and hybrid mode, respectively. In the Cu-MOF case, $\beta\gamma < 0$ and $|\beta|/|\gamma| \approx 0.8 < 1$, whereas in the $Ca_3Mn_2O_7$, $\beta\gamma > 0$ and $|\beta|/|\gamma| \approx 80 \gg 1$. When the sign of $\beta\gamma$ is positive (negative), the polarization directions by the hybrid mode and the polar mode are the same (opposite). The ratio $|\beta|/|\gamma|$ tells us which mode contributes to the polarization larger. If this ratio is larger (smaller) than 1, the polar (hybrid) mode contribution is larger. Hence, the case of $|\beta|/|\gamma| \gg 1$ corresponds to the case where the intuitive picture works well.

5 Magnetic Properties

This chapter shows the theoretical advances in the magnetism of Cr-/Cu-MOFs.

5.1 Revisit of Magnetism of Cr-MOF

5.1.1 Symmetries and spin model

As shown in Sec. 3.4, the new calculations in this thesis obtained a much smaller net magnetic moment of the Cr-MOF in comparison to the previous work [26]. Therefore, this section shows the justification of our new calculations and updates the spin-model analysis shown in Ref. [26].

First of all, let us have a look at the magnetic space group symmetry of the system. The Cr-/Cu-MOFs have four magnetic ions in a unit cell. The paramagnetic space group of the Cr-/Cu-MOFs, which has no local magnetic moment, is $Pna2_11'$. In the presence of a local magnetic moment at each Cr/Cu, four magnetic order parameters can be defined. **M** is a FM order parameter where all magnetic moments are aligned in the same direction. There are three AFM order parameters. The A-type AFM order parameter is **A**, where the neighboring moments in ab-plane are parallel (in the same direction), whereas the c-direction neighboring moments are antiparallel (the opposite direction). On the other hand, C-type AFM order (**C**) has the moments parallel to their

out-of-plane (c-axis) neighbors but antiparallel to the ab-plane neighbors. In G-type AFM order (**G**), a moment is antiparallel to all its neighbors.

Assuming that the primary order parameter is **A**, the following three cases are compatible with the symmetry properties [26, 66].

$$\begin{aligned} Pna2_1 &: \{A_b; G_a, C_c\} \\ Pn'a'2_1 &: \{A_a; G_b, M_c\} \\ Pna'2_1' &: \{A_c; C_b, M_a\} \end{aligned} \tag{5.1}$$

The $Pn'a'2_1$ and $Pna'2_1'$ are compatible with WFM components (parallel to c and a axes), where the prime means that the symmetry operation is accompanied by the time-reversal operation. The previous studies found that the symmetries of the ground states are $Pn'a'2_1$ for the Cr-MOF [26] and $Pna'2_1'$ for the Cu-MOF [17], with the A-type AFM primary order for both. These are confirmed again by our DFT calculations. However, the previous work on the Cr-MOF [26] considered only A_a and M_c. Thus, we will include the previously ignored order parameter G_b into our consideration.

Now, let us briefly review the spin model approach, which includes the MSIA that induces the spin canting [26, 66]. The primary effect that leads to the AFM-A ground state is the exchange interaction described via an isotropic 3D Heisenberg model for classical spins (with $S = 2$):

$$H_{\text{iso}} = \frac{1}{2} \sum_{ij} J_{ij} \, \boldsymbol{S}_i \cdot \boldsymbol{S}_j \tag{5.2}$$

The bond-anisotropic exchange interactions are given by $J_c > 0$ (AFM interaction) for the c-direction exchange coupling and $J_{ab} < 0$ (FM interaction) within ab-planes. The MSIA, which originates from the JT orbital ordering,

can be described by the following term in a local reference frame.

$$H_{\mathrm{sia}} = E \sum_i \left[(\boldsymbol{S}_i \cdot \boldsymbol{e}_i^s)^2 - (\boldsymbol{S}_i \cdot \boldsymbol{e}_i^l)^2 \right] + D \sum_i (\boldsymbol{S}_i \cdot \boldsymbol{e}_i^m)^2, \tag{5.3}$$

where E and D denoting the principal values of the MSIA tensor and $\boldsymbol{e}_i^l$, $\boldsymbol{e}_i^m$, and $\boldsymbol{e}_i^s$ denoting the long, medium and short M-O bonds of the JT-distorted MO_6 octahedra. In practice, H_{sia} should be properly rotated at each tilted octahedra in order to be consistent with the global spin of H_{iso} [26]. In addition, the AFD orbital ordering results in alternating sign changes of E in Eq. (5.3).

From the total spin Hamiltonian $H_{\mathrm{iso}} + H_{\mathrm{sia}}$, the mean-field energy is obtained as follows [66].

$$\begin{aligned} E(\delta, \epsilon) = & -J_c \cos 2\epsilon - 2|J_{ab}| \left[1 + \cos^2 \epsilon (\cos 2\delta - 1) \right] + D \cos^2 \theta_{\mathrm{t}} \sin^2 \epsilon \\ & + \frac{D}{2} \sin^2 \theta_{\mathrm{t}} \cos^2 \epsilon (1 - \cos 2\delta) - 2E \cos \theta_{\mathrm{t}} \cos^2 \epsilon \sin 2\delta \\ & + \sin \theta_{\mathrm{t}} \sin 2\epsilon \left(D \cos \theta_{\mathrm{t}} \sin \delta + E \cos \delta \right), \end{aligned} \tag{5.4}$$

where δ and ϵ are the spin canting angle of the secondary G-type (G_b) and ferromagnetic (M_c) order deviated from AFM-A configuration (A_a) of Cr-MOF, respectively. The canting angles can be determined by minimizing Eq. (5.4) with respect to both δ and ϵ. Simple analytical formulas are obtained assuming $\delta = 0$ or $\epsilon = 0$, giving respectively (Note a corrected sign for ϵ to Ref. [26]):

$$\tan 2\epsilon = -\frac{2E \sin \theta_{\mathrm{t}}}{2J_c + D \cos^2 \theta_{\mathrm{t}}} \tag{5.5}$$

$$\tan 2\delta = \frac{2E \cos \theta_{\mathrm{t}}}{2|J_{ab}| + D \sin^2 \theta_{\mathrm{t}}}, \tag{5.6}$$

where θ_{t} is a tilting angle of MO_6 octahedra from the c-axis. Since we usually expect the spin anisotropy energy to be smaller than the exchange coupling energy, a small canting angle is expected.

Before proceeding to the computational results, let us check the possibility of the Dzyaloshinskii-Moriya interaction (DMI) with the complete consideration of the magnetic order parameters. In the previous work [26], it was shown that the DMI is incompatible with $\{A_a; M_c\}$ or $\{A_c; M_a\}$ spin orderings. When we consider two Cr ions neighboring along c-direction with either of those two spin orderings, the octahedra tilting implies that the DM vector is parallel to a-axis ($\boldsymbol{D} \parallel \hat{a}$). On the other hand, the cross-product of two spins is parallel to the b-axis ($\boldsymbol{S}_1 \times \boldsymbol{S}_2 \parallel \hat{b}$). Since the DMI term in the Hamiltonian is usually described in the form of $\boldsymbol{D} \cdot (\boldsymbol{S}_1 \times \boldsymbol{S}_2)$, which vanishes in the above two cases, it can not affect the spin canting.

However, this is not the case in the presence of the G_b or C_b orders. Let us first consider the $\{A_a; G_b, M_c\}$ case ($Pn'a'2_1$). As a first-order expansion, we can write $\boldsymbol{S}_1 = S(1, \delta, \epsilon)$ and $\boldsymbol{S}_2 = S(-1, -\delta, \epsilon)$, which give $\boldsymbol{S}_1 \times \boldsymbol{S}_2 = S^2(2\delta\epsilon, -2\epsilon, 0)$. When we write $\boldsymbol{D} = (D, 0, 0)$, the DMI energy is $\boldsymbol{D} \cdot (\boldsymbol{S}_1 \times \boldsymbol{S}_2) = 2DS^2\delta\epsilon$, which is no longer zero. Hence, we can not strictly rule out the DMI as an origin of the spin canting. Nevertheless, we can ignore the DMI in practice because the DMI energy $2DS^2\delta\epsilon$ is quadratic to the small canting angles. On the other hand, in the case of $\{A_c; C_b, M_a\}$ ($Pna'2_1'$), we can write $\boldsymbol{S}_1 = S(\epsilon, \delta, 1)$ and $\boldsymbol{S}_2 = S(\epsilon, \delta, -1)$ (in this case, ϵ for M_a and δ for C_b). It leads to $\boldsymbol{S}_1 \times \boldsymbol{S}_2 = S^2(-2\delta, 2\epsilon, 0)$ and $\boldsymbol{D} \cdot (\boldsymbol{S}_1 \times \boldsymbol{S}_2) = -2DS^2\delta$. The DMI is linear to δ, which does not induce a net WFM moment. Therefore, the original argument of dismissing the DMI is still valid for $Pna'2_1'$, which corresponds to the Cu-MOF.

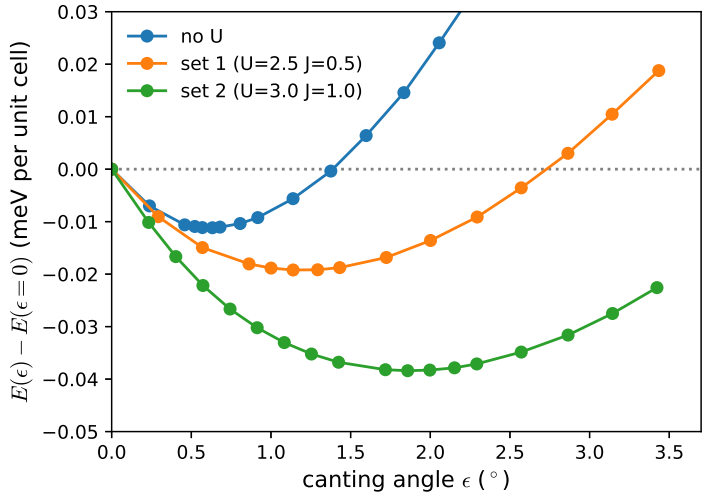

Figure 5.1 DFT total energies of Cr-MOF depending on the canting angle ϵ in *ac*-plane. Without the U and J corrections (no U), the total energy is minimum at $\epsilon = 0.63°$. With the DFT+$U + J$ correction, the minima are at $\epsilon = 1.19°$ and $\epsilon = 1.86°$ for the parameter set 1 (2.5,0.5) and set 2 (3,1), respectively.

5.1.2 Computation results

An ideal DFT calculation will converge to the ground state where the spin directions minimize the mean-field energy Eq. (5.4) when we give a reasonable initial guess, which will be the pure AFM-A spin configuration or that with a guess of small canting. The Cu-MOF is nearly such a case. However, we note that the Cr-MOF suffers from the convergence problem at the last stage of the SCF when the SOC is included. The spin canting direction is easily trapped near the initial guess, and the magnetic symmetry is slightly broken. Hence, we performed constrained spin calculations for the Cr-MOF in order to find a correct ground state. First, the total energies of the Cr-MOF with respect to increasing ϵ and fixed $\delta = 0$ ($\{A_a; M_c\}$) were calculated, as shown in Fig. 5.1 ("no U" data). The total energy is minimum at $\epsilon = 0.63°$, which is a much

smaller angle than the previous work [26]. In a similar way, we also examined the $\{A_a; G_b\}$ case, in which the total moment vanishes, by varying δ and fixing $\epsilon = 0$. We found that $\delta = 2.01°$ minimizes the total energy, which gives the alternating b-axis local moments of 0.127 μ_{B} per each Cr. The initial guesses for the DFT calculations of the $Pnan$-path in Fig. 3.2 were interpolated from the obtained ϵ and δ.

In fact, this small canting angle $\epsilon = 0.63°$ is very hard to detect experimentally. This is consistent with the recent experiment for the powder sample of Cr-MOF [66], which actually could not observe the WFM. On the other hand, the experiment observed that the critical temperature of the magnetic ordering is $T_c \approx 8$ K [66], which is much smaller than the previous theoretical estimation $T_c^{\mathrm{th}} \approx 40$ K [26]. Therefore, we also revised the T_c^{th} estimation of the Cr-MOF.

The T_c^{th} can be predicted by Monte Carlo (MC) simulation adopting a standard Metropolis algorithm for the spin Hamiltonian given by Eq. (5.2) and Eq. (5.3). Model parameters of the spin Hamiltonian can be estimated by total energy mapping of DFT computations. The J_{ab} and J_c can be obtained from the total energies with each pure M_c, A_c, C_c, and G_c spin configurations. Let us take the M_c as an example. A spin of each Cr atom interacts with two c-axis neighbors by J_c and four ab-plane neighbors by J_{ab}. Since there are four Cr atoms per unit-cell, and the parallel spins give $\boldsymbol{S}_i \cdot \boldsymbol{S}_j = S^2$, the total energy contribution per unit-cell given by H_{iso} [Eq. (5.2)] is $E_M|_{\mathrm{iso}} = (1/2) \times 4 \times (2J_c + 4J_{ab})S^2$. Similarly, $E_A|_{\mathrm{iso}} = (1/2) \times 4 \times (-2J_c + 4J_{ab})S^2$, $E_C|_{\mathrm{iso}} = (1/2) \times 4 \times (2J_c - 4J_{ab})S^2$, and $E_G|_{\mathrm{iso}} = (1/2) \times 4 \times (-2J_c - 4J_{ab})S^2$.

From these, the followings are derived with $|\mathbf{S}| = 2$.

$$\begin{aligned} J_c &= \frac{1}{64}(E_M + E_C - E_G - E_A) \\ J_{ab} &= \frac{1}{128}(E_M + E_A - E_G - E_C). \end{aligned} \tag{5.7}$$

Let us consider the octahedral tilting of Cr-MOF to construct the DFT total energy mapping to the spin anisotropy energy. Starting from an octahedron with (x, y, z) as local coordinates, which coincides with the crystal axes (a, b, c). First, rotate the octahedron by $-45°$ around the c-axis. Then, rotate it by $-\theta_{\mathrm{t}}$ around the a-axis. In this case, the spin components (S_x, S_y, S_z) in the octahedral coordinates (x, y, z) of the spin $\mathbf{S}$ parallel to each crystallographic direction are written as follows.

$$\begin{aligned} \mathbf{S} \parallel \hat{\mathbf{a}} &: (S_x, S_y, S_z) = S(1/\sqrt{2}, 1/\sqrt{2}, 0) \\ \mathbf{S} \parallel \hat{\mathbf{b}} &: (S_x, S_y, S_z) = S(-\cos\theta_{\mathrm{t}}/\sqrt{2}, \cos\theta_{\mathrm{t}}/\sqrt{2}, \sin\theta_{\mathrm{t}}) \\ \mathbf{S} \parallel \hat{\mathbf{c}} &: (S_x, S_y, S_z) = S(\sin\theta_{\mathrm{t}}/\sqrt{2}, -\sin\theta_{\mathrm{t}}/\sqrt{2}, \cos\theta_{\mathrm{t}}) \end{aligned} \tag{5.8}$$

From the above, in the cases of the AFM-A spin configurations along each crystal axes, the total energy contributions per unit-cell from the H_{sia} [Eq. (5.3)] are $E(A_a)|_{\mathrm{sia}} = 0$, $E(A_b)|_{\mathrm{sia}} = 4DS^2 \sin^2\theta_{\mathrm{t}}$, and $E(A_c)|_{\mathrm{sia}} = 4DS^2 \cos^2\theta_{\mathrm{t}}$. Therefore, $D = [E(A_b) + E(A_c) - 2E(A_a)]/16$. For the θ_{t}, we have two possibilities. One is to use the value measured from the structure as it is. Another is to use the value compatible with the DFT total energy mapping to the model. Namely, $\theta_{\mathrm{t}} = \arctan\left(\sqrt{E(A_b) - E(A_a)}/\sqrt{E(A_c) - E(A_a)}\right)$, which is adopted in the previous work [26]. Then the E can be obtained from J_c, θ_{t} and D via Eq. (5.5).

First, we computed the spin model parameters from the DFT total energy with the constrained spin conditions. As shown in the first row of Table 5.1 for

the parameters obtained in the previous work [26] and the second row for the present calculations, the new calculations obtained the results compatible with the previous work, except for the spin anisotropy parameter E. This deviation must have originated from the erroneously large canting angle ϵ in the previous work via Eq. (5.5). However, this correction could not drastically improve the T_c^{th} estimation.

Next, we took the on-site Coulomb interaction correction into account by the DFT+$U + J$ method [45]. Specifically, we assumed two sets of parameters with fixed $U - J = 2$ eV, $(U, J) = (2.5, 0.5)$ or $(U, J) = (3, 1)$, which we denote set 1 and set 2, respectively. As shown in Fig. 5.1, these two parameter sets result in larger canting angles than the previous calculations without the U and J corrections, $\epsilon = 1.19°$ and $\epsilon = 1.86°$ for the set 1 and set 2, respectively. The parameters extracted from the DFT calculations with these parameter sets are listed in the third and fourth row of Table 5.1. Interestingly, the U

	(U, J)	J_c	J_{ab}	D	E	θ_{t}
no U (Ref. [26])	$(0, 0)$	0.824	-0.453	0.113	0.745	30.8
no U (this work)	$(0, 0)$	0.837	-0.459	0.092	0.035	33.6
					(0.036)	(31.9)
set 1	$(2.5, 0.5)$	0.475	-0.111	0.115	0.038	33.8
					(0.041)	(31.9)
set 2	$(3.0, 1.0)$	0.453	-0.042	0.149	0.059	33.8
					(0.062)	(31.9)

Table 5.1 Model parameters (all couplings in meV, tilting angle in degrees) used in the Monte Carlo simulations for the Cr-MOF, with and without the $+U + J$ corrections. The parameters in the previous work [26] are also shown for comparison. The angle θ_{t} has been estimated from magnetic anisotropy energies. The two sets give the same angles, which is a non-trivial result. Such estimations are also in good agreement with the structural tilting angle (given in brackets). The values in brackets for the parameter E were obtained by using the structural tilting angle, showing small deviations that are found not to affect the results significantly.

	(U, J) (eV)	spin moment	orbital moment	$\lvert M_{\mathrm{orb}}\rvert$
Cr-MOF	$(0, 0)$	0.172	-0.024	0.031
Cr-MOF	$(2.5, 0.5)$	0.327	-0.031	0.035
Cr-MOF	$(3.0, 1.0)$	0.514	-0.032	0.035
Cu-MOF	$(0, 0)$	0.043	0.070	0.055
Cu-MOF	$(4.5, 0.5)$	0.054	0.096	0.077
Cu-MOF	$(5.0, 1.0)$	0.041	0.092	0.075

Table 5.2 DFT parameter dependence of the calculated magnetic moments. Units are Bohr magneton μ_B. $|M_{\mathrm{orb}}|$ is the magnitude of orbital magnetic moment of single Cr/Cu ion.

and J corrections reduce the exchange coupling strength (J_c and J_{ab}) and increase the spin anisotropy energies (D and E). The T_c^{th} estimated from these parameters via MC simulations [66] are about 14.5 K for set1 and 9.5 K for set 2, which are in good agreement with the experimental value $T_c \approx 8$ K [66]. This result implies that the on-site coulomb energy correction U and J are necessary to estimate the T_c of Cr-MOF.

We close this section with the U and J dependence of the calculated magnetic moments of Cr-/Cu-MOFs. Table 5.2 shows the net spin and orbital magnetic moments per unit cell (4 f.u.) and the magnitude of the orbital magnetic moment of a single Cr/Cu ion. One can see that the orbital magnetic moments are enhanced by the inclusion of the $+U + J$ correction.

5.2 Robust Orbital Weak Ferromagnetism in Cu-MOF

In general, magnetic moment originates from spin and orbital angular momenta. Usually for the transition metals, the orbital magnetic moment is small in comparison with the spin magnetic moment. For a transition metal ion in an octahedral environment, the orbital magnetic moment is quenched when the t_{2g} d-orbitals are fully- or half-filled. This is why it is often neglected,

including in the previous theoretical studies of Cr-/Cu-MOF [17, 26]. Even if the orbital magnetic moment is quenched, however, spin-orbit coupling (SOC) can induce a small orbital magnetic moment. In the case of the Cu-MOF, the spin contribution is also small as it is WFM. Therefore, the small orbital contribution may not be negligible, as shown in Sec. 3.4. This section will show our analysis and a model study on the orbital magnetic moments of the Cr-/Cu-MOFs.

5.2.1 Spin-Orbit coupling and Jahn-Teller distortion

In order to explain the orbital magnetic moment in Cr-/Cu-MOF, we focused on the SOC and the orbital ordering by the Jahn-Teller (JT) distortion. In particular, we established the model in which the perturbation method on the SOC is combined with the JT effective Hamiltonian within a single ion description. The perturbation approach for the SOC to consider the orbital angular momentum and MSIA in a solid is basically Bruno theory [69, 70], but we ignore the k-space dispersion for simplicity. The SOC Hamiltonian is written as $H_{\mathrm{SOC}} = \zeta \mathbf{S} \cdot \mathbf{L}$, where $\mathbf{S}$ and $\mathbf{L}$ are spin and orbital angular momentum operator, respectively. We will consider only d-orbitals here [71].

Let us first review the JT effective Hamiltonian. As introduced in Sec. 3.1, an $M\mathrm{O}_6$ octahedron is distorted in the d^4 and d^9 cases by the JT effect. This deformation is represented by two distortion modes $Q_2 = (1/\sqrt{2})(l_x - l_y)$ and $Q_3 = (1/\sqrt{6})(2l_z - l_x - l_y)$, where the l_i means the distance from the center to the oxygen on the i-axis. Then the JT distorted structure is expressed with the JT phase θ_{JT} as $|\theta_{\mathrm{JT}}\rangle = \cos\theta_{\mathrm{JT}} |Q_3\rangle + \sin\theta_{\mathrm{JT}} |Q_2\rangle$ and $\tan\theta_{\mathrm{JT}} = Q_2/Q_3$. The JT effective Hamiltonian taking the e_g orbitals $(d_{x^2-y^2}, d_{z^2})$ as a basis is

given by

$$H_{\mathrm{JT}} = \gamma \begin{pmatrix} q_1 & q_2 \\ q_2 & -q_1 \end{pmatrix} + \frac{1}{2} C q^2 \mathbf{I}_2 \tag{5.9}$$

where $q_1 = q\cos\theta_{\mathrm{JT}}$, $q_2 = q\sin\theta_{\mathrm{JT}}$, and $\mathbf{I}_2$ is 2×2 identity matrix [72]. The energy eigenvalues are $E_{\pm} = \pm\gamma q + \frac{1}{2}Cq^2$ and eigenstates are

$$\begin{aligned} \left|d_-(\theta_{\mathrm{JT}})\right\rangle &= -\sin\left(\theta_{\mathrm{JT}}/2\right)\left|d_{x^2-y^2}\right\rangle + \cos\left(\theta_{\mathrm{JT}}/2\right)\left|d_{z^2}\right\rangle \\ \left|d_+(\theta_{\mathrm{JT}})\right\rangle &= \cos\left(\theta_{\mathrm{JT}}/2\right)\left|d_{x^2-y^2}\right\rangle + \sin\left(\theta_{\mathrm{JT}}/2\right)\left|d_{z^2}\right\rangle . \end{aligned} \tag{5.10}$$

It represents the orbital-JT phase locking.

These unitary rotated, or the JT-transformed e_g-orbitals define the unitary matrix

$$U_0 = \begin{pmatrix} -\sin\left(\frac{\theta_{\mathrm{JT}}}{2}\right) & \cos\left(\frac{\theta_{\mathrm{JT}}}{2}\right) \\ \cos\left(\frac{\theta_{\mathrm{JT}}}{2}\right) & \sin\left(\frac{\theta_{\mathrm{JT}}}{2}\right) \end{pmatrix} \text{ and } U = \begin{pmatrix} \mathbf{I}_3 & \mathbf{0} \\ \mathbf{0} & U_0 \end{pmatrix}, \tag{5.11}$$

where U is the unitary matrix for the whole d-orbitals basis in $\{d_{yz}, d_{zx}, d_{xy}, d_{x^2-y^2}, d_{z^2}\}$ order. This redefines the orbital angular momentum operator $\mathbf{L}$, i.e., $(L_i^d)^{\mathrm{new}} = U^\dagger (L_i^d)^{\mathrm{old}} U$. Therefore, the SOC in the JT distorted system can be described via $(L_i^d)^{\mathrm{new}}$.

In order to express the SOC Hamiltonian $H_{\mathrm{SOC}} = \zeta \mathbf{S}\cdot\mathbf{L}$, let us denote the local coordinate unit vectors for spin operator as $(\mathbf{x}', \mathbf{y}', \mathbf{z}')$, and those for orbital angular momentum as $(\mathbf{x}, \mathbf{y}, \mathbf{z})$. H_{SOC} is parametrized by polar angle θ and azimuthal angle ϕ which describes the relative rotation of the spin coordinates, or simply the spin direction, with respect to the orbital coordinates, *i.e.*, $s_x = \sin\theta\cos\phi$, $s_y = \sin\theta\sin\phi$, and $s_z = \cos\theta$. We rotate the primed coordinates with respect to the unprimed coordinates. Then the primed coordinate unit vectors are $\mathbf{x}' = \cos\theta\cos\phi\mathbf{x} + \cos\theta\sin\phi\mathbf{y} - \sin\theta\mathbf{z}$,

$\mathbf{y}' = -\sin\phi\mathbf{x} + \cos\phi\mathbf{y}$, and $\mathbf{z}' = \sin\theta\cos\phi\mathbf{x} + \sin\theta\sin\phi\mathbf{y} + \cos\theta\mathbf{z}$. The SOC Hamiltonian is written as [71]

$$\begin{aligned} H_{\mathrm{SOC}} = \zeta\mathbf{S}\cdot\mathbf{L} = \frac{\zeta}{2}&\begin{pmatrix} \sin\theta\cos\phi & \cos\theta\cos\phi + i\sin\phi \\ \cos\theta\cos\phi - i\sin\phi & -\sin\theta\cos\phi \end{pmatrix} L_x \\ + \frac{\zeta}{2}&\begin{pmatrix} \sin\theta\sin\phi & \cos\theta\sin\phi - i\cos\phi \\ \cos\theta\sin\phi + i\cos\phi & -\sin\theta\sin\phi \end{pmatrix} L_y \\ + \frac{\zeta}{2}&\begin{pmatrix} \cos\theta & -\sin\theta \\ -\sin\theta & -\cos\theta \end{pmatrix} L_z. \end{aligned} \tag{5.12}$$

The matrix representation for the orbital angular momentum operator is determined by the quantum mechanical relations for the angular momentum states $L_z\,|l,m\rangle = m\,|l,m\rangle$ and $L_\pm\,|l,m\rangle = \sqrt{(l\mp m)(l\pm m+1)}\,|l,m\pm 1\rangle$. We take d-orbitals ($l = 2$) in the real spherical harmonics form as a basis: $|yz\rangle = (i/\sqrt{2})(|2,-1\rangle + |2,+1\rangle)$, $|zx\rangle = (1/\sqrt{2})(|2,-1\rangle - |2,+1\rangle)$, $|xy\rangle = (i/\sqrt{2})(|2,-2\rangle - |2,2\rangle)$, $\left|x^2 - y^2\right\rangle = (1/\sqrt{2})(|2,-2\rangle + |2,+2\rangle)$, and $\left|z^2\right\rangle = |2,0\rangle$. The matrix representations of L_i's for d-orbitals are as follows in atomic units ($\hbar = 1$).

$$L_x^d = \begin{pmatrix} 0 & 0 & 0 & -i & -i\sqrt{3} \\ 0 & 0 & i & 0 & 0 \\ 0 & -i & 0 & 0 & 0 \\ i & 0 & 0 & 0 & 0 \\ i\sqrt{3} & 0 & 0 & 0 & 0 \end{pmatrix} \tag{5.13}$$

$$L_y^d = \begin{pmatrix} 0 & 0 & -i & 0 & 0 \\ 0 & 0 & 0 & -i & i\sqrt{3} \\ i & 0 & 0 & 0 & 0 \\ 0 & i & 0 & 0 & 0 \\ 0 & -i\sqrt{3} & 0 & 0 & 0 \end{pmatrix} \tag{5.14}$$

$$L_z^d = \begin{pmatrix} 0 & i & 0 & 0 & 0 \\ -i & 0 & 0 & 0 & 0 \\ 0 & 0 & 0 & 2i & 0 \\ 0 & 0 & -2i & 0 & 0 \\ 0 & 0 & 0 & 0 & 0 \end{pmatrix} \tag{5.15}$$

By transforming these matrices via $(L_i^d)^{\text{new}} = U^\dagger (L_i^d)^{\text{old}} U$ with Eq. (5.11), we

can obtain the JT-transformed orbital angular momentum operator.

$$(L_x^d)^{\text{new}} = \begin{pmatrix} 0 & 0 & 0 & i\sin\left(\frac{\theta_{\text{JT}}}{2}\right) - i\sqrt{3}\cos\left(\frac{\theta_{\text{JT}}}{2}\right) & -i\cos\left(\frac{\theta_{\text{JT}}}{2}\right) - i\sqrt{3}\sin\left(\frac{\theta_{\text{JT}}}{2}\right) \\ & 0 & i & 0 & 0 \\ & & 0 & 0 & 0 \\ & & & 0 & 0 \\ h.c. & & & & 0 \end{pmatrix} \tag{5.16}$$

$$(L_y^d)^{\text{new}} =$$

$$\begin{pmatrix} 0 & 0 & -i & 0 & 0 \\ & 0 & 0 & i\sin\left(\frac{\theta_{\text{JT}}}{2}\right) + i\sqrt{3}\cos\left(\frac{\theta_{\text{JT}}}{2}\right) & -i\cos\left(\frac{\theta_{\text{JT}}}{2}\right) + i\sqrt{3}\sin\left(\frac{\theta_{\text{JT}}}{2}\right) \\ & & 0 & 0 & 0 \\ & & & 0 & 0 \\ h.c. & & & & 0 \end{pmatrix} \tag{5.17}$$

$$(L_z^d)^{\text{new}} = \begin{pmatrix} 0 & i & 0 & 0 & 0 \\ & 0 & 0 & 0 & 0 \\ & & 0 & -2i\sin\left(\frac{\theta_{\text{JT}}}{2}\right) & 2i\cos\left(\frac{\theta_{\text{JT}}}{2}\right) \\ & & & 0 & 0 \\ h.c. & & & & 0 \end{pmatrix} \tag{5.18}$$

The SOC in the JT distorted system can be expressed by using these operators. Hereafter, we omit the superscripts 'd' and 'new' of L_i for simplicity.

5.2.2 Perturbation theory

The perturbation theory is applied to obtain the orbital angular momentum by the SOC. The d-orbitals with the 'JT transformed' e_g-orbitals [Eq. (5.10)] are taken as the unperturbed basis $\left|d_{n\sigma}^0\right\rangle$ where $n = \{yz, zx, xy, -, +\}$ and $\sigma =\uparrow$ or $\downarrow$ spins. The first order corrected d-orbitals are

$$|d_\alpha\rangle = \left|d_\alpha^0\right\rangle + \sum_{\beta\neq\alpha} \frac{\left\langle d_\beta^0 \middle| H_{SOC} \middle| d_\alpha^0 \right\rangle}{E_\alpha^0 - E_\beta^0} \left|d_\beta^0\right\rangle \tag{5.19}$$

where the α and β are combined indices of orbital species and spin. We can obtain the orbital angular momentum of transition metal ion in the JT distorted O_6 cage by calculating $\langle L_i\rangle = \sum_{\alpha\in\text{occ}} \langle d_\alpha|L_i|d_\alpha\rangle$ up to first order in ζ, where

the summation is over the occupied orbitals and L_i is the JT-transformed operators $(L_i^d)^{\text{new}}$. The orbital angular momentum expectation value for a perturbed d-orbital $d_{n\uparrow}$ is

$$\begin{aligned}\left\langle d_{n\uparrow}\middle|L_i\middle|d_{n\uparrow}\right\rangle = &\left\langle d^0_{n\uparrow}\middle|L_i\middle|d^0_{n\uparrow}\right\rangle \\ &+\sum_{m\neq n}\left[\frac{\left\langle d^0_{m\uparrow}\middle|H_{SOC}\middle|d^0_{n\uparrow}\right\rangle}{E^0_{n\uparrow}-E^0_{m\uparrow}}\left\langle d^0_{n\uparrow}\middle|L_i\middle|d^0_{m\uparrow}\right\rangle + c.c.\right] \\ &+\sum_{\text{all } m}\left[\frac{\left\langle d^0_{m\downarrow}\middle|H_{SOC}\middle|d^0_{n\uparrow}\right\rangle}{E^0_{n\uparrow}-E^0_{m\downarrow}}\left\langle d^0_{n\uparrow}\middle|L_i\middle|d^0_{m\downarrow}\right\rangle + c.c.\right] \\ &+O(\zeta^2).\end{aligned} \tag{5.20}$$

Because $\left\langle d^0_{n\uparrow}\middle|L_i\middle|d^0_{n\uparrow}\right\rangle = \left\langle d^0_{n\uparrow}\middle|L_i\middle|d^0_{m\downarrow}\right\rangle = 0$, only the second term remains up to the first order in ζ.

For calculating the summation over the expectations values corresponding to Eq. (5.20) of occupied orbitals, the following property can be exploited. If we sum up all the orbital angular momentum expectation values of the perturbed d-orbitals with up-spin,

$$\sum_n \left\langle d_{n\uparrow}\middle|L_i\middle|d_{n\uparrow}\right\rangle = \sum_n\sum_{m\neq n}\left[\frac{\left\langle d^0_{m\uparrow}\middle|H_{SOC}\middle|d^0_{n\uparrow}\right\rangle}{E^0_{n\uparrow}-E^0_{m\uparrow}}\left\langle d^0_{n\uparrow}\middle|L_i\middle|d^0_{m\uparrow}\right\rangle + c.c.\right] = 0 \tag{5.21}$$

because each of the terms is canceled with the term whose n and m are exchanged. The same holds for down spin. It makes it easy to calculate the orbital angular momentum for d^4 and d^9. For the spin-up high spin configuration of the Cr^{2+} ion (d^4), occupied d-orbitals are $\{d_{yz\uparrow}, d_{zx\uparrow}, d_{xy\uparrow}, d_{-\uparrow}\}$. Therefore, $\langle L_i\rangle_{d^4} = -\left\langle d_{+\uparrow}\middle|L_i\middle|d_{+\uparrow}\right\rangle$ for d^4. For the Cu^{2+} ion (d^9), only $d_{+\downarrow}$ is unoccupied. For d^9, by using $\left\langle d^0_{n\uparrow}\middle|L_i\middle|d^0_{m\downarrow}\right\rangle = 0$ and $\left\langle d^0_{m\uparrow}\middle|H_{SOC}\middle|d^0_{n\uparrow}\right\rangle = -\left\langle d^0_{m\downarrow}\middle|H_{SOC}\middle|d^0_{n\downarrow}\right\rangle$ derived from Eq. (5.12), $\langle L_i\rangle_{d^9} = -\left\langle d_{+\downarrow}\middle|L_i\middle|d_{+\downarrow}\right\rangle = -\langle L_i\rangle_{d^4}$.

The perturbed $|d_+\rangle$ is

$$
\begin{aligned}
|d_+\rangle = \left|d_+^0\right\rangle &+ \left(\frac{\zeta}{2}\right) \frac{\sin\theta\cos\phi\left(-i\cos\left(\frac{\theta_{\mathrm{JT}}}{2}\right) - i\sqrt{3}\sin\left(\frac{\theta_{\mathrm{JT}}}{2}\right)\right)}{E_+^0 - E_{yz}^0} \left|d_{yz}^0\right\rangle \\
&+ \left(\frac{\zeta}{2}\right) \frac{\sin\theta\sin\phi\left(-i\cos\left(\frac{\theta_{\mathrm{JT}}}{2}\right) + i\sqrt{3}\sin\left(\frac{\theta_{\mathrm{JT}}}{2}\right)\right)}{E_+^0 - E_{zx}^0} \left|d_{zx}^0\right\rangle \\
&+ \left(\frac{\zeta}{2}\right) \frac{2i\cos\theta\cos\left(\frac{\theta_{\mathrm{JT}}}{2}\right)}{E_+^0 - E_{xy}^0} \left|d_{xy}^0\right\rangle .
\end{aligned}
\tag{5.22}
$$

The t_{2g} orbital components are included in this expression. This is why the orbital angular momentum can appear. In the d^4 configuration,

$$
\begin{aligned}
\langle L_i\rangle_{d^4} &= -\langle d_+|L_i|d_+\rangle \\
&= -\left\langle d_+^0\middle|L_i\middle|d_+^0\right\rangle \\
&- \left(\frac{\zeta}{2}\right) \frac{\sin\theta\cos\phi\left(-i\cos\left(\frac{\theta_{\mathrm{JT}}}{2}\right) - i\sqrt{3}\sin\left(\frac{\theta_{\mathrm{JT}}}{2}\right)\right)}{E_+^0 - E_{yz}^0} \left\langle d_+^0\middle|L_i\middle|d_{yz}^0\right\rangle + c.c. \\
&- \left(\frac{\zeta}{2}\right) \frac{\sin\theta\sin\phi\left(-i\cos\left(\frac{\theta_{\mathrm{JT}}}{2}\right) + i\sqrt{3}\sin\left(\frac{\theta_{\mathrm{JT}}}{2}\right)\right)}{E_+^0 - E_{zx}^0} \left\langle d_+^0\middle|L_i\middle|d_{zx}^0\right\rangle + c.c. \\
&- \left(\frac{\zeta}{2}\right) \frac{2i\cos\theta\cos\left(\frac{\theta_{\mathrm{JT}}}{2}\right)}{E_+^0 - E_{xy}^0} \left\langle d_+^0\middle|L_i\middle|d_{xy}^0\right\rangle + c.c.
\end{aligned}
\tag{5.23}
$$

Matrix elements $\langle d_n^0 | L_i | d_m^0 \rangle$ are given by Eq. (5.16)-(5.18). As a result, the orbital angular momenta of the d^4 configuration are

$$\begin{aligned}
\langle L_x \rangle_{d^4} &= -\zeta \frac{\left(\cos\left(\frac{\theta_{\mathrm{JT}}}{2}\right) + \sqrt{3}\sin\left(\frac{\theta_{\mathrm{JT}}}{2}\right)\right)^2}{E_+^0 - E_{yz}^0} s_x \\
\langle L_y \rangle_{d^4} &= -\zeta \frac{\left(\cos\left(\frac{\theta_{\mathrm{JT}}}{2}\right) - \sqrt{3}\sin\left(\frac{\theta_{\mathrm{JT}}}{2}\right)\right)^2}{E_+^0 - E_{zx}^0} s_y \\
\langle L_z \rangle_{d^4} &= -\zeta \frac{\left(2\cos\left(\frac{\theta_{\mathrm{JT}}}{2}\right)\right)^2}{E_+^0 - E_{xy}^0} s_z
\end{aligned} \tag{5.24}$$

for each x, y, z component, where $\hat{\mathbf{s}} = (s_x, s_y, s_z)$ is the local spin direction defined by (θ,ϕ) with respect to the local orbital coordinates, not the spin operators. Note that we adopt the atomic units in which $\hbar = 1$. For d^9 configuration, $\langle L_i \rangle_{d^9} = -\langle L_i \rangle_{d^4}$. It is noteworthy that the resultant local orbital moment is not parallel to $\hat{\mathbf{s}}$. The deviation is explicitly determined by θ_{JT}.

5.2.3 Model analysis for Cr-/Cu-MOF

The results of the previous section are applied to the orbital magnetic moment in the Cr-/Cu-MOF. The angular momentum in Eq. (5.24) is simply replaced with the magnetic moment in Bohr magneton μ_{B} unit for both the spin and orbital. As discussed in Sec. 5.1.1, the magnetic space group $Pna'2_1'$ (A_c and M_a) and $Pn'a'2_1$ (A_a and M_c) that are compatible with the AFM-A order will be considered. The formulation will be shown in both magnetic group cases for both Cr- and Cu-MOFs. For simplicity, we will ignore the spin canting in the following analysis, i.e., a perfect AFM-A spin configuration.

In order to apply Eq. (5.24) to the Cr-/Cu-MOF, we take one out of four Cr/Cu ions in a unit cell of MOF, say Cr/Cu1, as a reference to describe

the system [Cu1 is labeled in Fig. 3.1 (a-c)]. If we know the local MO_6 structure and the local moment of the Cr/Cu ion at one site, those of other sites are determined by the space group and magnetic group symmetry. The transformation rules of the magnetic moment and the corresponding Cr/Cu site numbers with respect to Cr/Cu1 by each symmetry operation are listed in Table. 5.3.

Let us consider the O_6 octahedron of the reference Cr/Cu1 ion. The local coordinate $(\mathbf{x}, \mathbf{y}, \mathbf{z})$ of the orbital magnetic moment is aligned to its O-M bond directions. The local coordinate system is determined by the following steps. First, put the octahedron in the way that the local coordinates $(\mathbf{x}, \mathbf{y}, \mathbf{z})$ are aligned with crystallographic $(\hat{\mathbf{a}}, \hat{\mathbf{b}}, \hat{\mathbf{c}})$ direction. Next, rotate the octahedron by $-\pi/4$ around the c axis, then by octahedral tilting angle $-\theta_{\mathrm{t}}$ around the a axis consecutively. As a result, $(\mathbf{x}, \mathbf{y}, \mathbf{z})$ can be written as follows.

$$\begin{aligned}
\mathbf{x} &= \tfrac{1}{\sqrt{2}}\hat{\mathbf{a}} - \tfrac{1}{\sqrt{2}}\cos\theta_{\mathrm{t}}\hat{\mathbf{b}} + \tfrac{1}{\sqrt{2}}\sin\theta_{\mathrm{t}}\hat{\mathbf{c}} \\
\mathbf{y} &= \tfrac{1}{\sqrt{2}}\hat{\mathbf{a}} + \tfrac{1}{\sqrt{2}}\cos\theta_{\mathrm{t}}\hat{\mathbf{b}} - \tfrac{1}{\sqrt{2}}\sin\theta_{\mathrm{t}}\hat{\mathbf{c}} \\
\mathbf{z} &= \sin\theta_{\mathrm{t}}\hat{\mathbf{b}} + \cos\theta_{\mathrm{t}}\hat{\mathbf{c}}
\end{aligned} \tag{5.25}$$

The direction of the local spin magnetic moment of Cr/Cu1 is expressed in terms of the spherical coordinates θ_{spin} and ϕ_{spin} with respect to the local

Cr/Cu	$Pna'2'_1$		$Pn'a'2_1$	
	op.	$\mathbf{L}$	op.	$\mathbf{L}$
1	1	(L_a, L_b, L_c)	1	(L_a, L_b, L_c)
2	n	$(L_a, -L_b, -L_c)$	n'	$(-L_a, L_b, L_c)$
3	a'	$(L_a, -L_b, L_c)$	a'	$(L_a, -L_b, L_c)$
4	$2'_1$	$(L_a, L_b, -L_c)$	2_1	$(-L_a, -L_b, L_c)$

Table 5.3 Labels of Cr/Cu ions, corresponding symmetry operations, and the transformation rules of the magnetic moment by them in the magnetic space group $Pna'2'_1$ and $Pn'a'2_1$. 1 means the identity operation.

coordinate. If we ignore a small spin canting, the direction of spin is exactly c-direction in $Pna'2'_1$. It correspond to $\theta_{\text{spin}} = \theta_{\text{t}}$ and $\phi_{\text{spin}} = -\frac{\pi}{4}$. For $Pn'a'2_1$, spin direction is a and corresponding angles are $\theta_{\text{spin}} = \frac{\pi}{2}$ and $\phi_{\text{spin}} = \frac{\pi}{4}$.

For the $Pna'2'_1$ symmetry, the total moment is four times the a-component of the moment of the reference Cr/Cu1. By using the above relations,

$$\langle L\rangle_{\text{total}}^{Pna'2'_1} = 4\,\langle L\rangle_a = 4(\tfrac{1}{\sqrt{2}}\,\langle L_x\rangle + \tfrac{1}{\sqrt{2}}\,\langle L_y\rangle) \tag{5.26}$$

Likewise, for the $Pn'a'2_1$ symmetry, the total moment is four times the c-component of the moment of the reference Cr/Cu1.

$$\langle L\rangle_{\text{total}}^{Pn'a'2_1} = 4\,\langle L\rangle_c = 4(\tfrac{1}{\sqrt{2}}\sin\theta_{\text{t}}\,\langle L_x\rangle - \tfrac{1}{\sqrt{2}}\sin\theta_{\text{t}}\,\langle L_y\rangle + \cos\theta_{\text{t}}\,\langle L_z\rangle) \tag{5.27}$$

Now we can obtain the net orbital magnetic moment per unit cell from the local orbital magnetic moments Eq. (5.24) for each symmetry. For the d^4 configuration (Cr^{2+}) with $Pna'2'_1$ symmetry, the total orbital moment is

$$\begin{aligned}\langle L\rangle_{\text{total}}^{Pna'2'_1} = &-2\left(\frac{\zeta}{E_+^0-E_{yz}^0} - \frac{\zeta}{E_+^0-E_{zx}^0}\right)\sin\theta_{\text{t}}(2-\cos\theta_{\text{JT}}) \\ &-2\sqrt{3}\left(\frac{\zeta}{E_+^0-E_{yz}^0} + \frac{\zeta}{E_+^0-E_{zx}^0}\right)\sin\theta_{\text{t}}\sin\theta_{\text{JT}}\end{aligned} \tag{5.28}$$

along the a-axis. Since the difference between E_{yz}^0 and E_{zx}^0 is small, the first term is small compared to the second term. Moreover, $\langle L\rangle_{\text{total}}$ vanishes when $\theta_{\text{JT}} = \pi$, since $l_x \approx l_y$ leads to $E_{yz}^0 \approx E_{zx}^0$. This situation corresponds to $\mathbf{r}_1(0)$ in the $Pnan$-path or $\lambda_{X_4^+} = 0$ in the $Imam$-path, where the net magnetic moment actually vanishes in the DFT results. By introducing the approximation $E_{yz}^0 = E_{zx}^0 = E_{xy}^0 \equiv E_{t_{2g}}^0$, the orbital magnetic moment can be simplified as

$$\langle L\rangle_{\text{total}}^{Pna'2'_1} = -4\sqrt{3}\left(\frac{\zeta}{E_+^0-E_{t_{2g}}^0}\right)\sin\theta_{\text{t}}\sin\theta_{\text{JT}}. \tag{5.29}$$

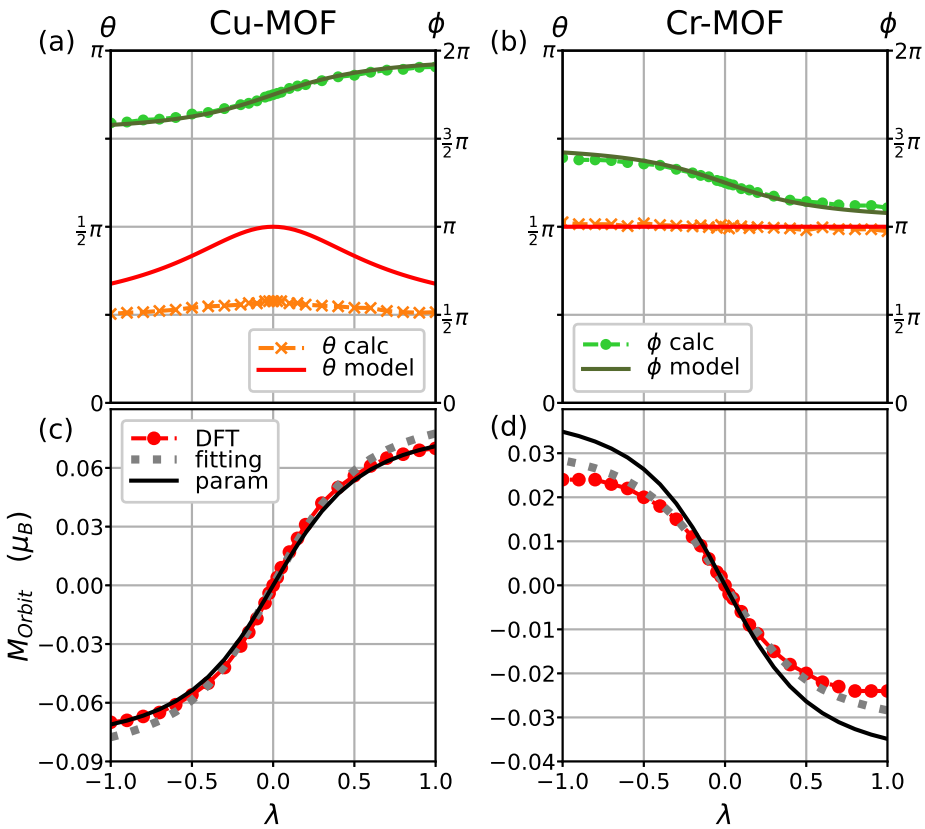

Figure 5.2 The direction of the local orbital magnetic moment of reference ions of (a) Cu-MOF and (b) Cr-MOF in their local spherical coordinates (θ: polar/ ϕ: azimuthal) obtained from DFT and the model. The total orbital magnetic moment per unit cell of (c) Cu-MOF and (d) Cr-MOF obtained from DFT and model. Model values in (c) and (d) are fitted to the DFT results (gray dotted line) and evaluated from reasonable physical parameters (black solid line).

For the d^4 with $Pn'a'2_1$ symmetry, interestingly, the same total orbital magnetic moment formula is obtained, $\langle L\rangle_{\text{total}}^{Pn'a'2_1} = \langle L\rangle_{\text{total}}^{Pna'2'_1}$, except that the direction is along the c-axis. Therefore, the same arguments are also valid leading to the same simplified form of Eq. (5.29). For the d^9 configuration (Cu^{2+}), the sign of the orbital magnetic moment is inverted in both magnetic groups.

As a preliminary for the comparison between the DFT results and the predictions from the model, we parametrize the JT phase θ_{JT} of the reference Cr/Cu1 ion as a function of λ of the *Pnan*-path. In the Cu-MOF, as the λ increases from 0 to 1, JT mode Q_2 changes linearly from 0 to 0.288, as shown in Fig. 3.1 (e). Meanwhile, Q_3 changes very little, so it can be considered a constant [Fig. 3.1 (f)]. $\lambda = 0$ and $\lambda = 1$ correspond to $\theta_{\mathrm{JT}} = \pi$ and $\theta_{\mathrm{JT}} = 1.934 \approx 0.616\pi$, respectively [Fig. 3.1 (g)]. This situation can be said that $\tan(\pi - \theta_{\mathrm{JT}})$ is proportional to Q_2. This leads to $\tan(\pi - \theta_{\mathrm{JT}})/\tan\big(\pi - \theta_{\mathrm{JT},\lambda=1}\big) = \lambda$, where $\theta_{\mathrm{JT},\lambda=1}$ is the JT phase at $\lambda = 1$. For simplicity, let us assume $\theta_{\mathrm{JT},\lambda=1} = 2\pi/3$ instead of the actual value, which corresponds to $\left|d^0_-\right\rangle = -\left|x^2\right\rangle$ and $\left|d^0_+\right\rangle = -\left|y^2 - z^2\right\rangle$. The JT phase becomes $\theta_{\mathrm{JT}} = \pi - \tan^{-1}(\sqrt{3}\lambda)$. As a result, the simplified orbital magnetic moment Eq. (5.29) can be written in terms of the λ,

$$\langle L_{\mathrm{total}}\rangle_{d^4/d^9} = \mp 4\sqrt{3}\left(\frac{\zeta}{E^0_+ - E^0_{t_{2g}}}\right)\sin\theta_{\mathrm{t}}\frac{\sqrt{3}\lambda}{\sqrt{3\lambda^2+1}}. \tag{5.30}$$

Ignoring the JT phase dependency of E^0_i's, we define the λ independent factor of this expression as $A = \mp 4\sqrt{3}(\zeta/(E^0_+ - E^0_{t_{2g}}))\sin\theta_{\mathrm{t}}$. To check the validity of the model, we compare the model with the DFT values by fitting the single parameter A. Fitted A values are 0.090 for Cu-MOF and -0.033 for Cr-MOF.

In addition, the A values can be estimated from reasonable physical parameters. We adopted the SOC parameter $\zeta = 56.54$ meV for Cu and $\zeta = 27.52$ meV for Cr [73], $\Delta E = E^0_+ - E^0_{t_{2g}} = 2.5$ eV for both of the Cu-MOF and Cr-MOF. ΔE is roughly chosen from the projected density of states obtained from the DFT calculation. The tilting angles of MO_6 octahedron extracted from the structures are $\theta_{\mathrm{t}} = 31.61°$ for Cu-MOF and $\theta_{\mathrm{t}} = 31.88°$ for Cr-MOF.

The obtained A values are 0.082 for Cu-MOF and -0.040 for Cr-MOF, which are in good agreement with the fitted values. As shown in Fig. 5.2 (c) and (d), the model with these A values well explains the DFT results.

In addition, let us consider the direction of the local orbital magnetic moment of a reference Cu and Cr ions expected from Eq. (5.24) with the approximation $E^0_{yz} = E^0_{zx} = E^0_{xy}$, as shown in Fig. 5.2 (a) and (b) in their local spherical coordinates, respectively. The directions from the DFT are shown together for comparison. Except for the deviation in the polar angle θ of Cu-MOF, the model predicts the orbital magnetic moment direction well.

Interestingly, the model predicts the finite orbital magnetic moment even though we assumed the uncanted spin configuration in which the total spin moment vanishes. The orbital magnetic moment rotates depending on the JT phase in spite of the fixed spin direction. The inclusion of the small spin canting ($\epsilon < 1°$) would not significantly alter the predicted orbital magnetic moment. For example, the canting of 1° changes only about a factor of 0.0175 (1° in radians) of the results. Moreover, the orbital magnetic moment is linear to the SOC strength ζ, whereas the MSIA is second order. These properties provide a robust justification of WFM in terms of the total magnetic moment (spin + orbital) for Cu-MOF and also emphasize the role of the JT effect on it. Finally, we remark that the orbital magnetic moment can be measured by means of x-ray magnetic circular dichroism [74].

5.2.4 Second order energy corrections

In this section, we will calculate the energy correction by the SOC in the perturbation approach, which gives rise to the MSIA. In the previous study [26], only the fixed JT phase and the same-spin contribution are considered for the

MSIA. We improve the formulation by including the general JT phase and the opposite spin contribution. The first order energy correction $\left\langle d^0_{n\sigma}\middle|H_{\mathrm{SOC}}\middle|d^0_{n\sigma}\right\rangle$ vanishes because the diagonal components of L^d_i are 0. The lowest order energy correction is the second order correction term,

$$\Delta E^2_\alpha = \sum_{\beta\neq\alpha} \frac{\left|\left\langle d^0_\beta\middle|H_{SOC}\middle|d^0_\alpha\right\rangle\right|^2}{E^0_\alpha - E^0_\beta}. \tag{5.31}$$

It is convenient to separate the H_{SOC} [Eq. (5.12)] into the same-spin block and opposite-spin block.

$$H_{\mathrm{SOC},\uparrow\uparrow} = \frac{\zeta}{2}(\sin\theta\cos\phi L_x + \sin\theta\sin\phi L_y + \cos\theta L_x) = -H_{\mathrm{SOC},\downarrow\downarrow} \tag{5.32}$$

and

$$H_{\mathrm{SOC},\uparrow\downarrow} = \frac{\zeta}{2}\left[(\cos\theta\cos\phi + i\sin\phi)L_x + (\cos\theta\sin\phi - i\cos\phi)L_y + (-\sin\theta)L_z\right] \tag{5.33}$$

Similar to the orbital angular momentum case, the summation of the second-order correction to the energy with the non-degenerate assumption in the half-filling case with only up-spins provides a shortcut for the calculation.

$$\begin{aligned}\sum_{\alpha\in\uparrow}\Delta E^2_\alpha &= \sum_{\alpha\in\uparrow}\sum_{\beta\neq\alpha}\frac{\left|\left\langle d^0_\beta\middle|H_{SOC}\middle|d^0_\alpha\right\rangle\right|^2}{E^0_\alpha - E^0_\beta} \\ &= \sum_n\sum_{m\neq n}\frac{\left|\left\langle d^0_{m\uparrow}\middle|H_{SOC,\uparrow\uparrow}\middle|d^0_{n\uparrow}\right\rangle\right|^2}{E^0_{n\uparrow} - E^0_{m\uparrow}} + \sum_n\sum_m\frac{\left|\left\langle d^0_{m\downarrow}\middle|H_{SOC,\downarrow\uparrow}\middle|d^0_{n\uparrow}\right\rangle\right|^2}{E^0_{n\uparrow} - E^0_{m\downarrow}}\end{aligned} \tag{5.34}$$

The first term of the last line is the summation of the same-spin contribution to energy correction which vanishes. On the other hand, the second term is the summation of the opposite-spin contribution and is non-vanishing in general.

It makes the difference between the expression of the energy correction of the d^4 spin configuration and that of the d^9.

The opposite-spin contributions from each orbital of the d^4 configuration are as follows.

$$
\begin{aligned}
(\Delta E^2_{yz\uparrow})_{\downarrow\uparrow} = \left(\tfrac{\zeta}{2}\right)^2 \Big[& \frac{\sin^2\theta}{E^0_{yz\uparrow} - E^0_{zx\downarrow}} + \frac{\cos^2\theta\sin^2\phi + \cos^2\phi}{E^0_{yz\uparrow} - E^0_{xy\downarrow}} \\
& + \frac{\Big(-\sin\big(\theta_{\mathrm{JT}}/2\big) + \sqrt{3}\cos\big(\theta_{\mathrm{JT}}/2\big)\Big)^2 (\cos^2\theta\cos^2\phi + \sin^2\phi)}{E^0_{yz\uparrow} - E^0_{-\downarrow}} \\
& + \frac{\Big(\cos\big(\theta_{\mathrm{JT}}/2\big) + \sqrt{3}\sin\big(\theta_{\mathrm{JT}}/2\big)\Big)^2 (\cos^2\theta\cos^2\phi + \sin^2\phi)}{E^0_{yz\uparrow} - E^0_{+\downarrow}} \Big]
\end{aligned}
\tag{5.35}
$$

$$
\begin{aligned}
(\Delta E^2_{zx\uparrow})_{\downarrow\uparrow} = \left(\tfrac{\zeta}{2}\right)^2 \Big[& \frac{\sin^2\theta}{E^0_{zx\uparrow} - E^0_{yz\downarrow}} + \frac{\cos^2\theta\cos^2\phi + \sin^2\phi}{E^0_{zx\uparrow} - E^0_{xy\downarrow}} \\
& + \frac{\Big(\sin\big(\theta_{\mathrm{JT}}/2\big) + \sqrt{3}\cos\big(\theta_{\mathrm{JT}}/2\big)\Big)^2 (\cos^2\theta\sin^2\phi + \cos^2\phi)}{E^0_{zx\uparrow} - E^0_{-\downarrow}} \\
& + \frac{\Big(\cos\big(\theta_{\mathrm{JT}}/2\big) - \sqrt{3}\sin\big(\theta_{\mathrm{JT}}/2\big)\Big)^2 (\cos^2\theta\sin^2\phi + \cos^2\phi)}{E^0_{zx\uparrow} - E^0_{+\downarrow}} \Big]
\end{aligned}
\tag{5.36}
$$

$$
\begin{aligned}
(\Delta E^2_{xy\uparrow})_{\downarrow\uparrow} = \left(\tfrac{\zeta}{2}\right)^2 \Big[& \frac{\cos^2\theta\sin^2\phi + \cos^2\phi}{E^0_{xy\uparrow} - E^0_{yz\downarrow}} + \frac{\cos^2\theta\cos^2\phi + \sin^2\phi}{E^0_{xy\uparrow} - E^0_{zx\downarrow}} \\
& + \frac{4\sin^2(\theta_{\mathrm{JT}}/2)\sin^2\theta}{E^0_{xy\uparrow} - E^0_{-\downarrow}} + \frac{4\cos^2(\theta_{\mathrm{JT}}/2)\sin^2\theta}{E^0_{xy\uparrow} - E^0_{+\downarrow}} \Big]
\end{aligned}
\tag{5.37}
$$

$$
\begin{aligned}
(\Delta E^2_{-\uparrow})_{\downarrow\uparrow} = \left(\tfrac{\zeta}{2}\right)^2 \Big[& \frac{\Big(-\sin\big(\theta_{\mathrm{JT}}/2\big) + \sqrt{3}\cos\big(\theta_{\mathrm{JT}}/2\big)\Big)^2 (\cos^2\theta\cos^2\phi + \sin^2\phi)}{E^0_{-\uparrow} - E^0_{yz\downarrow}} \\
& + \frac{\Big(\sin\big(\theta_{\mathrm{JT}}/2\big) + \sqrt{3}\cos\big(\theta_{\mathrm{JT}}/2\big)\Big)^2 (\cos^2\theta\sin^2\phi + \cos^2\phi)}{E^0_{-\uparrow} - E^0_{zx\downarrow}} \\
& + \frac{4\sin^2(\theta_{\mathrm{JT}}/2)\sin^2\theta}{E^0_{-\uparrow} - E^0_{xy\downarrow}} \Big]
\end{aligned}
\tag{5.38}
$$

The spin direction-dependent terms including θ and ϕ can be rewritten in physically intuitive expressions,

$$\begin{aligned}
&\cos^2\theta\cos^2\phi + \sin^2\phi = 1 - \sin^2\theta\cos^2\phi = 1 - (\hat{\mathbf{s}}\cdot\mathbf{x})^2 \\
&\cos^2\theta\sin^2\phi + \cos^2\phi = 1 - \sin^2\theta\sin^2\phi = 1 - (\hat{\mathbf{s}}\cdot\mathbf{y})^2 \\
&\sin^2\theta = 1 - \cos^2\theta = 1 - (\hat{\mathbf{s}}\cdot\mathbf{z})^2,
\end{aligned} \tag{5.39}$$

where $\hat{\mathbf{s}} = \mathbf{s}/|\mathbf{s}|$ is the unit vector indicating the spin direction. Meanwhile, it implies the existence of the spin direction independent contribution to the energy correction.

The same-spin contribution to the energy correction is simply $(\Delta E^2_{d^4})_{\uparrow\uparrow} = -(\Delta E^2_{+\uparrow})_{\uparrow\uparrow}$ because the first term of the Eq. (5.34) vanishes.

$$\begin{aligned}
(\Delta E^2_{d^4})_{\uparrow\uparrow} = -\left(\tfrac{\zeta}{2}\right)^2 \Bigg[& \frac{\Big(\cos\big(\theta_{\mathrm{JT}}/2\big) + \sqrt{3}\sin\big(\theta_{\mathrm{JT}}/2\big)\Big)^2 (\sin^2\theta\cos^2\phi)}{E^0_{+\uparrow} - E^0_{yz\uparrow}} \\
& + \frac{\Big(\cos\big(\theta_{\mathrm{JT}}/2\big) - \sqrt{3}\sin\big(\theta_{\mathrm{JT}}/2\big)\Big)^2 (\sin^2\theta\sin^2\phi)}{E^0_{+\uparrow} - E^0_{zx\uparrow}} \\
& + \frac{4\cos^2(\theta_{\mathrm{JT}}/2)\cos^2\theta}{E^0_{+\uparrow} - E^0_{xy\uparrow}} \Bigg]
\end{aligned} \tag{5.40}$$

By summing up these terms, the spin direction-dependent part of the second-order correction to the energy in d^4 configuration is

$$
\begin{aligned}
&\Delta E^2_{d^4}(\mathbf{S}) \\
&= \left(\tfrac{\zeta}{2}\right)^2 (\hat{\mathbf{s}}\cdot\mathbf{x})^2 \Big[\Big(\frac{-1}{E^0_{+\uparrow}-E^0_{yz\uparrow}} + \frac{1}{E^0_{+\downarrow}-E^0_{yz\uparrow}}\Big)\Big(\cos\big(\theta_{\mathrm{JT}}/2\big)+\sqrt{3}\sin\big(\theta_{\mathrm{JT}}/2\big)\Big)^2 \\
&+ \Big(\frac{1}{E^0_{-\downarrow}-E^0_{yz\uparrow}} + \frac{1}{E^0_{yz\downarrow}-E^0_{-\uparrow}}\Big)\Big(\sin\big(\theta_{\mathrm{JT}}/2\big)-\sqrt{3}\cos\big(\theta_{\mathrm{JT}}/2\big)\Big)^2 \\
&+ \frac{1}{E^0_{xy\downarrow}-E^0_{zx\uparrow}} + \frac{1}{E^0_{zx\downarrow}-E^0_{xy\uparrow}}\Big] \\
&+ \left(\tfrac{\zeta}{2}\right)^2 (\hat{\mathbf{s}}\cdot\mathbf{y})^2 \Big[\Big(\frac{-1}{E^0_{+\uparrow}-E^0_{zx\uparrow}} + \frac{1}{E^0_{+\downarrow}-E^0_{zx\uparrow}}\Big)\Big(\cos\big(\theta_{\mathrm{JT}}/2\big)-\sqrt{3}\sin\big(\theta_{\mathrm{JT}}/2\big)\Big)^2 \\
&+ \Big(\frac{1}{E^0_{-\downarrow}-E^0_{zx\uparrow}} + \frac{1}{E^0_{zx\downarrow}-E^0_{-\uparrow}}\Big)\Big(\sin\big(\theta_{\mathrm{JT}}/2\big)+\sqrt{3}\cos\big(\theta_{\mathrm{JT}}/2\big)\Big)^2 \\
&+ \frac{1}{E^0_{xy\downarrow}-E^0_{yz\uparrow}} + \frac{1}{E^0_{yz\downarrow}-E^0_{xy\uparrow}}\Big] \\
&+ \left(\tfrac{\zeta}{2}\right)^2 (\hat{\mathbf{s}}\cdot\mathbf{z})^2 \Big[\Big(\frac{-1}{E^0_{+\uparrow}-E^0_{xy\uparrow}} + \frac{1}{E^0_{+\downarrow}-E^0_{xy\uparrow}}\Big) 4\cos^2(\theta_{\mathrm{JT}}/2) \\
&+ \Big(\frac{1}{E^0_{-\downarrow}-E^0_{xy\uparrow}} + \frac{1}{E^0_{xy\downarrow}-E^0_{-\uparrow}}\Big) 4\sin^2(\theta_{\mathrm{JT}}/2) + \frac{1}{E^0_{zx\downarrow}-E^0_{yz\uparrow}} + \frac{1}{E^0_{yz\downarrow}-E^0_{zx\uparrow}}\Big]
\end{aligned}
\tag{5.41}
$$

For the d^9 spin configuration, the second-order correction to the energy can be obtained simply.

$$
\begin{aligned}
\Delta E^2_{d^9} &= \sum_{n=\text{occupied}} \Delta E^2_n = -\Delta E^2_{+\downarrow} \\
&= -\left(\tfrac{\zeta}{2}\right)^2 \Bigg[\frac{\Big(\cos\big(\theta_{\mathrm{JT}}/2\big) + \sqrt{3}\sin\big(\theta_{\mathrm{JT}}/2\big)\Big)^2 (\cos^2\theta\cos^2\phi + \sin^2\phi)}{E^0_{+\downarrow} - E^0_{yz\uparrow}} \\
&+ \frac{\Big(\cos\big(\theta_{\mathrm{JT}}/2\big) - \sqrt{3}\sin\big(\theta_{\mathrm{JT}}/2\big)\Big)^2 (\cos^2\theta\sin^2\phi + \cos^2\phi)}{E^0_{+\downarrow} - E^0_{zx\uparrow}} \\
&+ \frac{4\cos^2(\theta_{\mathrm{JT}}/2)\sin^2\theta}{E^0_{+\downarrow} - E^0_{xy\uparrow}} \\
&+ \frac{\Big(\cos\big(\theta_{\mathrm{JT}}/2\big) + \sqrt{3}\sin\big(\theta_{\mathrm{JT}}/2\big)\Big)^2 (\sin^2\theta\cos^2\phi)}{E^0_{+\downarrow} - E^0_{yz\downarrow}} \\
&+ \frac{\Big(\cos\big(\theta_{\mathrm{JT}}/2\big) - \sqrt{3}\sin\big(\theta_{\mathrm{JT}}/2\big)\Big)^2 (\sin^2\theta\sin^2\phi)}{E^0_{+\downarrow} - E^0_{zx\downarrow}} + \frac{4\cos^2(\theta_{\mathrm{JT}}/2)\cos^2\theta}{E^0_{+\downarrow} - E^0_{xy\downarrow}} \Bigg]
\end{aligned}
\tag{5.42}
$$

The spin direction-dependent part is

$$
\begin{aligned}
&\Delta E^2_{d^9}(\mathbf{S}) \\
&= \left(\tfrac{\zeta}{2}\right)^2 (\hat{\mathbf{s}}\cdot\mathbf{x})^2 \Bigg[\left(\frac{-1}{E^0_{+\downarrow} - E^0_{yz\downarrow}} + \frac{1}{E^0_{+\downarrow} - E^0_{yz\uparrow}} \right) \Big(\cos\big(\theta_{\mathrm{JT}}/2\big) + \sqrt{3}\sin\big(\theta_{\mathrm{JT}}/2\big)\Big)^2 \Bigg] \\
&+ \left(\tfrac{\zeta}{2}\right)^2 (\hat{\mathbf{s}}\cdot\mathbf{y})^2 \Bigg[\left(\frac{-1}{E^0_{+\downarrow} - E^0_{zx\downarrow}} + \frac{1}{E^0_{+\downarrow} - E^0_{zx\uparrow}} \right) \Big(\cos\big(\theta_{\mathrm{JT}}/2\big) - \sqrt{3}\sin\big(\theta_{\mathrm{JT}}/2\big)\Big)^2 \Bigg] \\
&+ \left(\tfrac{\zeta}{2}\right)^2 (\hat{\mathbf{s}}\cdot\mathbf{z})^2 \Bigg[\left(\frac{-1}{E^0_{+\downarrow} - E^0_{xy\downarrow}} + \frac{1}{E^0_{+\downarrow} - E^0_{xy\uparrow}} \right) 4\cos^2(\theta_{\mathrm{JT}}/2) \Bigg]
\end{aligned}
\tag{5.43}
$$

The terms in the spin direction-dependent part of the second-order energy corrections are divided into three parts corresponding to the local coordinate components, (x, y, z). Each directional part is again divided according to the dependency on the JT phase. Orbital ordering following the JT distortion

	$\Delta E < 0$	$\Delta E > 0$
$(\hat{\mathbf{s}} \cdot \mathbf{x})^2$	$(\cos(\theta_{\mathrm{JT}}/2) + \sqrt{3}\sin(\theta_{\mathrm{JT}}/2))^2$	$(\sin(\theta_{\mathrm{JT}}/2) - \sqrt{3}\cos(\theta_{\mathrm{JT}}/2))^2$
$(\hat{\mathbf{s}} \cdot \mathbf{y})^2$	$(\cos(\theta_{\mathrm{JT}}/2) - \sqrt{3}\sin(\theta_{\mathrm{JT}}/2))^2$	$(\sin(\theta_{\mathrm{JT}}/2) + \sqrt{3}\cos(\theta_{\mathrm{JT}}/2))^2$
$(\hat{\mathbf{s}} \cdot \mathbf{z})^2$	$4\cos^2(\theta_{\mathrm{JT}}/2)$	$4\sin^2(\theta_{\mathrm{JT}}/2)$

Table 5.4 Classification of the JT phase dependence according to the energy lowering and raising. $\Delta E < (>)\ 0$ means that the factor in energies multiplied by the listed JT phase-dependent factor is negative (positive).

affects the energy correction in two ways. One is the JT transformation of the e_g orbitals, which is explicitly expressed by the JT phase in Eq. (5.41) and Eq. (5.43). The other is the changes in the SOC-unperturbed orbital energies E_i^0 which is implicit in the expressions Eq. (5.41) and Eq. (5.43). Because the crystal field splitting is larger than the changes by the JT effect, we can consider that the factors in the trigonometric functions of the JT phase in the Eq. (5.41) and Eq. (5.43) are leading factors to determine the MSIA direction. We can ignore the JT dependency of E_i^0's for simplicity. Note that the difference between the d^4 [Eq. (5.41)] and d^9 [Eq. (5.43)] cases rationalizes the difference in the favored AFM axis between Cr- (a) and Cu-MOF (c), although a comparison by evaluating all those terms is too complicated.

In $\Delta E^2_{d^4}(\mathbf{S})$, each directional part is composed of three sub-parts. Two of them are JT phase dependent and one is JT phase independent. Because we assumed $E^0_{e_g\uparrow} - E^0_{t_{2g}\uparrow} < E^0_{e_g\downarrow} - E^0_{t_{2g}\uparrow}$ and $E^0_{e_g\downarrow} - E^0_{t_{2g}\uparrow} > E^0_{t_{2g}\downarrow} - E^0_{e_g\uparrow} > 0$, we can determine whether each of the JT phase dependent sub-part is the energy-lowering or -raising term according to the sign of these energy-related factors. They are classified in Table. 5.4. JT phase independent terms are always energy-raising terms. Due to the phase difference by π of the JT phase dependent factors, the energy-lowering and -raising terms result in the same

tendencies of the favored spin direction at a given θ_{JT}. On the other hand, $\Delta E^2_{d^9}(\mathbf{S})$ has only the energy-lowering terms.

5.3 Spin and Orbital Textures

The spin texture in the k-space of the Cr-/Cu-MOF shows interesting features. The spin texture is defined as $\mathbf{s_k} = \langle \psi_{\mathbf{k}n} | \mathbf{S} | \psi_{\mathbf{k}n} \rangle$ for a specific band n. In this work, the spin expectation values are extracted from the projected values to each atomic state, which are stored in the output file PROCAR of VASP. The spin texture of the highest occupied band of each MOF at $k_z = 0$ and $k_z = \pi/c$ planes are shown in Fig. 5.3. In the Cu-MOF, a 'curly' in-plane texture appears around the center at $k_z = 0$ plane. On the other hand, an irregular texture mostly aligned to z-direction can be seen at $k_z = \pi/c$ plane. In the Cr-MOF, persistent type spin textures [75] appear over the considered region for both the $k_z = 0$ and $k_z = \pi/c$ planes.

Since we observed that the orbital magnetic moment is a dominant contribution to the magnetic moment of the Cu-MOF and a local orbital magnetic moment is not parallel to the local spin moment in both Cr-/Cu-MOFs, it is interesting to investigate the orbital texture. In our context, the orbital texture is the orbital angular momentum texture defined as $\mathbf{l}_{\mathbf{k}n} = \langle \psi_{\mathbf{k}n} | \mathbf{L} | \psi_{\mathbf{k}n} \rangle$. For this purpose, we adopted another first-principles calculation package OpenMX [76], which adopts the linear combination of the pseudo atomic orbital (LCPAO) method. Therefore, orbital angular momentum can be calculated at an atomic orbital angular momentum operator level. As a LCPAO basis, we adopted `H6.0-s2p2`, `C6.0-s2p2`, `N6.0-s2p2`, `O6.0-s2p2d1`, `Cu6.0H-s2p2d2f1`, and `Cr6.0-s2p2d2f1`, which indicate the number of the set of each s, p, d, and f orbital

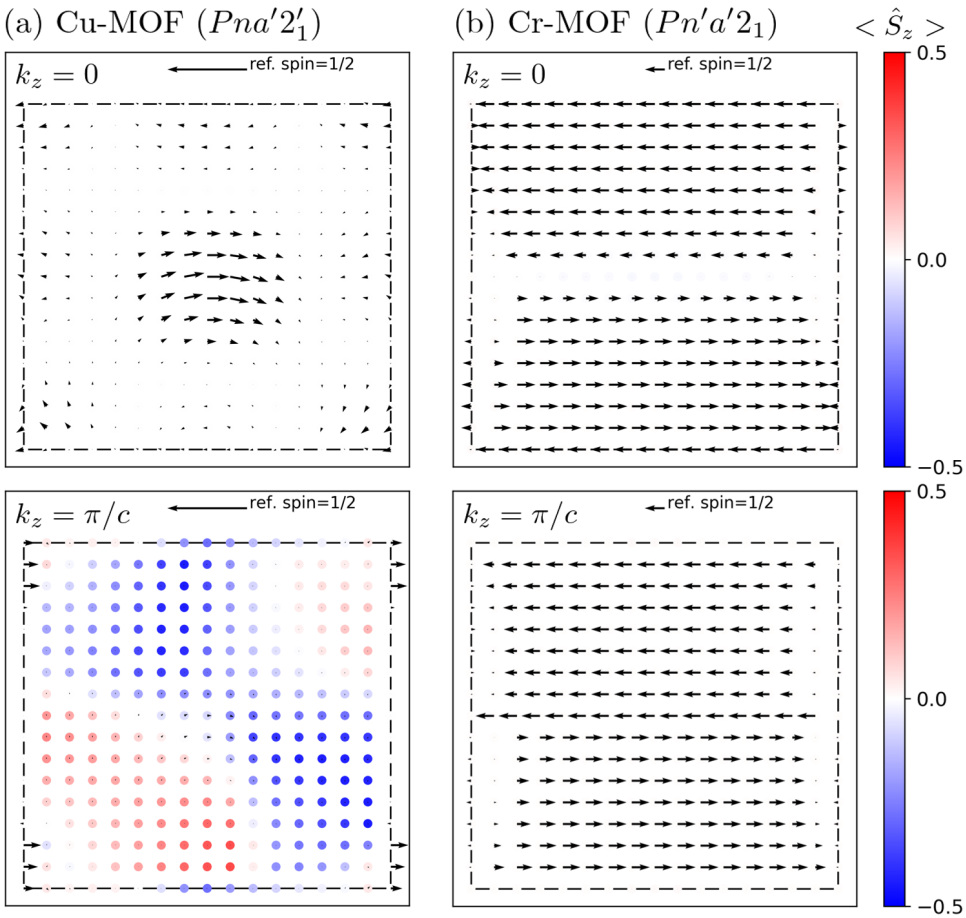

Figure 5.3 The spin textures of (a) Cu-MOF and (b) Cr-MOF, at the $k_z = 0$ (upper panels) and $k_z = \pi/c$ (lower panels) planes. The in-plane x and y components are represented by arrows, of which the length is the in-plane magnitude with respect to the reference spin 1/2 above the figure. The z components are represented by a colormap of dots. The inner boundary of each figure coincides with the Brillouin zone boundary.

sets for each atomic species. Other computational settings are compatible with the setting for the VASP package.

As a preliminary step, we calculated the spin texture using OpenMX [77] to check if the two software packages give compatible results. As shown in Fig. 5.4, the main features of the spin textures are consistent: In the Cu-MOF, the curly in-plane texture at $k_z = 0$ and the alignment to z-direction at $k_z = \pi/c$ [Fig. 5.4

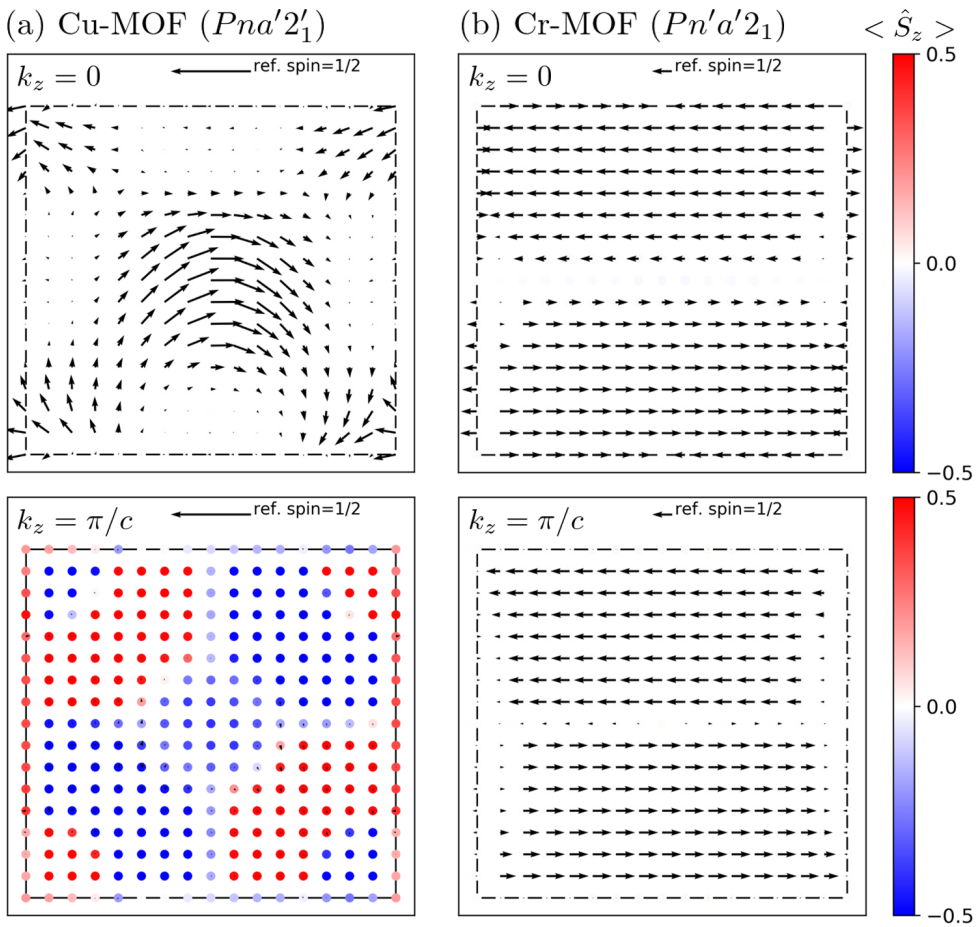

Figure 5.4 The spin textures calculated by using OpenMX. (a) Cu-MOF and (b) Cr-MOF, at the $k_z = 0$ (upper panels) and $k_z = \pi/c$ (lower panels) planes. The in-plane x and y components are represented by arrows of which the length is the in-plane magnitude with respect to the reference spin 1/2 above the figure. The z components are represented by colormap of dots. The inner boundary of each figure coincides with the Brillouin zone boundary.

(a)]; In the Cr-MOF, the persistent type spin textures [Fig. 5.4 (b)]. On the other hand, there are some differences in the case of Cu-MOF. The magnitude of the spins are larger in the OpenMX data at $k_z = 0$, and the signs of the z components at $k_z = \pi/c$ show a different pattern. Nevertheless, we can expect that primary features will be shared in the OpenMX results.

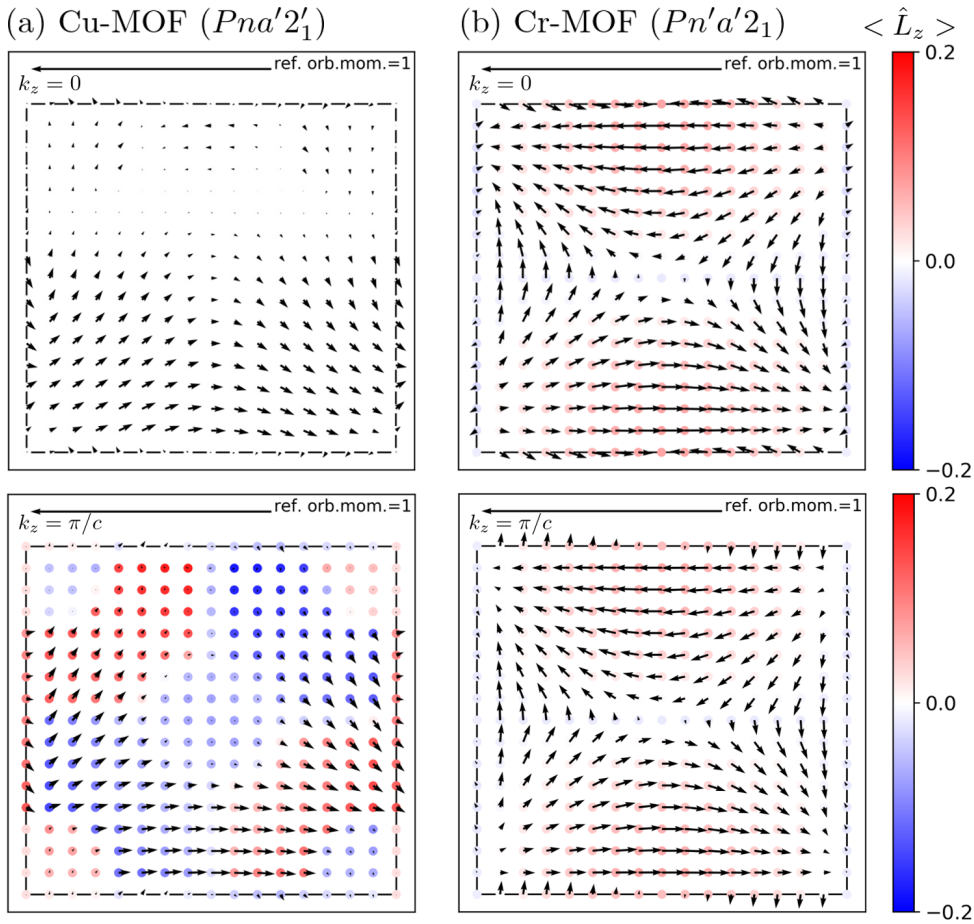

Figure 5.5 The orbital angular momentum textures calculated by using OpenMX. (a) Cu-MOF and (b) Cr-MOF, at the $k_z = 0$ (upper panels) and $k_z = \pi/c$ (lower panels) planes. The in-plane x and y components are represented by arrows of which the length is the in-plane magnitude with respect to the reference orbital angular momentum 1 above the figure. The z components are represented by colormap of dots. The inner boundary of each figure coincides with the Brillouin zone boundary.

The orbital textures calculated by OpenMX are shown in Fig. 5.5. The orbital angular momenta are calculated using an in-house post-processing program for OpenMX. Interestingly, the orbital textures are not parallel to the spin textures at all k-points. In the Cu-MOF [Fig. 5.5 (a)], there are no out-of-plane components at $k_z = 0$ plane, and their in-plane components show

a different pattern from the spin texture. At $k_z = \pi/c$, the out-of-plane orbital texture shows a similar texture with the spin besides their magnitude. However, there are also in-plane components in the orbital texture. In the Cr-MOF [Fig. 5.5 (b)], interestingly, the in-plane orbital texture shows a Dresselhaus-type texture [78] at both $k_z = 0$ and $k_z = \pi/c$ planes, *i.e.*, the coexistence of the persistent spin texture and the Dresselhaus orbital texture. Also, there are small out-of-plane components in the orbital texture.

6 Summary and Perspectives

In this thesis, we discussed the theoretical approaches for the multiferroics based on the density functional theory (DFT) and investigated the multiferroic properties of the perovskite-type metal-organic frameworks (MOFs) metal guanidinium formates $[C(NH_2)_3]M(HCOO)_3$ (M = Cr, Cu; Cr-MOF and Cu-MOF) via the DFT and various physical models.

In the Cr-/Cu-MOFs, the cooperative Jahn-Teller (JT) effect deforms the MO_6 octahedra so that the antiferro-distortive orbital ordering arises. This give rises to weak ferromagnetism in addition to the A-type antiferromagnetism. On the other hand, it has been known that spontaneous electric polarization appears via the hybrid improper ferroelectricity (HIFE) mechanism in the Cr-/Cu-MOFs. In this thesis, we further revealed the unexplored electronic and magnetic properties of the Cr-/Cu-MOFs by the first-principles calculation.

First, we found a counterintuitive electronic property. In the HIFE mechanism, the polar distortion mode is induced by two non-polar modes, of which the combined mode is referred to as the hybrid mode. In an intuitive picture, only the polar mode can induce polarization. However, in Cr-/Cu-MOFs, the hybrid mode induces a dominant purely electronic polarization even without the polar mode. This is a distinctive feature that can not be seen in inorganic HIFE materials. On the microscopic scale, this originates from the asymmetry in the A-site guanidinium ions. Contrary to common sense, the polar mode rather

compensates for the polarization stabilizing the structure. We constructed a macroscopic model via the Landau free energy theory, where the polarization and polar distortion mode order parameters are treated separately. As a result, the model could deal with these unusual properties.

Even though the comparison to the inorganic HIFE material $Ca_3Mn_2O_7$ implies that the large purely electronic polarization in HIFE is a distinct feature in MOFs, there is still room for different interpretations. For example, one can classify these two cases as the polarization from covalence bonds for Cr-/Cu-MOF and ionic bonds for $Ca_3Mn_2O_7$. Therefore, it is desirable to investigate if the inorganic HIFE material with a strong covalence bond character induces a large purely electronic polarization. On the other hand, since the Gua ion is non-polar when there is no bond-length asymmetry, it is interesting to investigate the HIFE MOF in which the polarization originates from the polar molecules.

Second, we provided revised descriptions of the magnetic properties of the Cr-/Cu-MOFs. For the Cr-MOF, we found the more reasonable ground state and enhanced the accuracy of the critical temperature prediction of the magnetic ordering by including the on-site Coulomb energy corrections in DFT. For the Cu-MOF, we found that the orbital magnetic moment is a more significant contribution to the total magnetic moment than the spin contribution. We revealed that the orbital magnetic moment is explicitly coupled with the JT distortion via the model study based on the JT effective Hamiltonian, thus showing the robustness of the orbital magnetic moment in the Cu-MOF.

Since the model for the orbital magnetic moment established in this thesis is based on the single ion picture, a similar analysis is possible for the inorganic

analog of the MOFs. For example, $KCuF_3$ [79] is an inorganic analog of the Cu-MOF. Therefore, it will be interesting to check whether these two show the same magnetic properties or not. It may reveal a specific role of the organic constituents in magnetism. On the other hand, how the organic linkers affect the exchange interactions in MOFs can also be worth examining. For this purpose, the magnetic force theorem can be a useful theoretical framework.

Although our study focused on $[C(NH_2)_3]M(HCOO)_3$ series, it will be interesting to apply the viewpoint demonstrated in this thesis to other families of the perovskite-type multiferroic MOFs. Recently, not only three-dimensional MOFs but also two-dimensional MOFs [80–82] have been drawing attention from the condensed matter physics and material science communities. Likewise our study on the Cr-MOF and Cu-MOF, we anticipate that more and more novel properties that cannot be found in purely inorganic materials appear in the three- and two-dimensional MOFs.

Bibliography

[1] Akihiro Kojima, Kenjiro Teshima, Yasuo Shirai, and Tsutomu Miyasaka. Organometal halide perovskites as visible-light sensitizers for photovoltaic cells. *Journal of the American Chemical Society*, **131** (2009), 6050–6051.

[2] Martin A. Green, Ewan D. Dunlop, Jochen Hohl-Ebinger, Masahiro Yoshita, Nikos Kopidakis, and Xiaojing Hao. Solar cell efficiency tables (version 59). *Progress in Photovoltaics: Research and Applications*, **30** (2022), 3–12.

[3] Alessandro Stroppa, Claudio Quarti, Filippo De Angelis, and Silvia Picozzi. Ferroelectric polarization of $CH_3NH_3PbI_3$: a detailed study based on density functional theory and symmetry mode analysis. *The Journal of Physical Chemistry Letters*, **6** (2015), 2223–2231.

[4] Keith T. Butler, Katrine Svane, Gregor Kieslich, Anthony K. Cheetham, and Aron Walsh. Microscopic origin of entropy-driven polymorphism in hybrid organic-inorganic perovskite materials. *Physical Review B*, **94** (2016), 180103.

[5] Minsung Kim, Jino Im, Arthur J. Freeman, Jisoon Ihm, and Hosub Jin. Switchable $S = 1/2$ and $J = 1/2$ rashba bands in ferroelectric halide perovskites. *Proceedings of the National Academy of Sciences*, **111** (2014), 6900–6904.

[6] Claudio Quarti, Edoardo Mosconi, and Filippo De Angelis. Interplay of orientational order and electronic structure in methylammonium lead iodide: implications for solar cell operation. *Chemistry of Materials*, **26** (2014), 6557–6569.

[7] Hiroyasu Furukawa, Kyle E. Cordova, Michael O'Keeffe, and Omar M. Yaghi. The chemistry and applications of metal-organic frameworks. *Science*, **341** (2013), 1230444.

[8] Myunghyun Paik Suh, Hye Jeong Park, Thazhe Kootteri Prasad, and Dae-Woon Lim. Hydrogen storage in metal–organic frameworks. *Chemical Reviews*, **112** (2012), 782–835.

[9] A. K. Cheetham, and C. N. R. Rao. There's room in the middle. *Science*, **318** (2007), 58–59.

[10] Xin-Yi Wang, Lin Gan, Shi-Wei Zhang, and Song Gao. Perovskite-like metal formates with weak ferromagnetism and as precursors to amorphous materials. *Inorganic Chemistry*, **43** (2004), 4615–4625.

[11] Qiong Ye, Yu-Mei Song, Guo-Xi Wang, Kai Chen, Da-Wei Fu, Philip Wai Hong Chan, Jin-Song Zhu, Songping D. Huang, and Ren-Gen Xiong. Ferroelectric metalorganic framework with a high dielectric constant. *Journal of the American Chemical Society*, **128** (2006), 6554–6555.

[12] T. Kimura, T. Goto, H. Shintani, K. Ishizaka, T. Arima, and Y. Tokura. Magnetic control of ferroelectric polarization. *Nature*, **426** (2003), 55–58.

[13] Bas B. Van Aken, Thomas T.M. Palstra, Alessio Filippetti, and Nicola A. Spaldin. The origin of ferroelectricity in magnetoelectric $YMnO_3$. *Nature Materials*, **3** (2004), 164–170.

[14] Sang-Wook Cheong, and Maxim Mostovoy. Multiferroics: a magnetic twist for ferroelectricity. *Nature Materials*, **6** (2007), 13–20.

[15] Andrei Malashevich, and David Vanderbilt. First principles study of improper ferroelectricity in $TbMnO_3$. *Physical Review Letters*, **101** (2008), 037210.

[16] Daniel Khomskii. Classifying multiferroics: mechanisms and effects. *Physics*, **2** (2009), 20.

[17] Alessandro Stroppa, Prashant Jain, Paolo Barone, Martijn Marsman, Juan Manuel Perez-Mato, Anthony K. Cheetham, Harold W. Kroto, and Silvia Picozzi. Electric control of magnetization and interplay between orbital ordering and ferroelectricity in a multiferroic metal-organic framework. *Angewandte Chemie International Edition*, **50** (2011), 5847–5850.

[18] Maciej Ptak, Mirosław Mączka, Anna Gągor, Adam Sieradzki, Alessandro Stroppa, Domenico Di Sante, Juan Manuel Perez-Mato, and Lucyna Macalik. Experimental and theoretical studies of structural phase transition in a novel polar perovskite-like $[C_2H_5NH_3][Na_{0.5}Fe_{0.5}(HCOO)_3]$ formate. *Dalton Transactions*, **45** (2016), 2574–2583.

[19] L. Claudia Gómez-Aguirre, Breogán Pato-Doldán, Alessandro Stroppa, Li-Ming Yang, Thomas Frauenheim, Jorge Mira, Susana Yáñez-Vilar, Ramón Artiaga, Socorro Castro-García, Manuel Sánchez-Andújar, and María Antonia Señarís-Rodríguez. Coexistence of three ferroic orders in the multiferroic compound $[(CH_3)_4N][Mn(N_3)_3]$ with perovskite-like structure. *Chemistry - A European Journal*, **22** (2016), 7863–7870.

[20] Feng-Ren Fan, Hua Wu, Dmitrii Nabok, Shunbo Hu, Wei Ren, Claudia Draxl, and Alessandro Stroppa. Electric-magneto-optical kerr effect in a hybrid organic–inorganic perovskite. *Journal of the American Chemical Society*, **139** (2017), 12883–12886.

[21] Paul J. Saines, and Nicholas C. Bristowe. Probing magnetic interactions in metal–organic frameworks and coordination polymers microscopically. *Dalton Transactions*, **47** (2018), 13257–13280.

[22] Yinina Ma, and Young Sun. Multiferroic and thermal expansion properties of metal-organic frameworks. *Journal of Applied Physics*, **127** (2020), 080901.

[23] P.S. Ghosh, D. DeTellem, J. Ren, S. Witanachchi, S. Ma, S. Lisenkov, and I. Ponomareva. Unusual properties of hydrogen-bonded ferroelectrics: the case of cobalt formate. *Physical Review Letters*, **128** (2022), 077601.

[24] S. Picozzi, and A. Stroppa. Advances in ab-initio theory of multiferroics: materials and mechanisms: modelling and understanding. *The European Physical Journal B*, **85** (2012), 240.

[25] Wen Zhang, and Ren-Gen Xiong. Ferroelectric metal–organic frameworks. *Chemical Reviews*, **112** (2012), 1163–1195.

[26] A. Stroppa, P. Barone, P. Jain, J. M. Perez-Mato, and S. Picozzi. Hybrid improper ferroelectricity in a multiferroic and magnetoelectric metal-organic framework. *Advanced Materials*, **25** (2013), 2284–2290.

[27] Domenico Di Sante, Alessandro Stroppa, Prashant Jain, and Silvia Picozzi. Tuning the ferroelectric polarization in a multiferroic metal–organic framework. *Journal of the American Chemical Society*, **135** (2013), 18126–18130.

[28] Saurabh Ghosh, Domenico Di Sante, and Alessandro Stroppa. Strain tuning of ferroelectric polarization in hybrid organic inorganic perovskite compounds. *The Journal of Physical Chemistry Letters*, **6** (2015), 4553–4559.

[29] Ying Tian, Alessandro Stroppa, Yi-Sheng Chai, Paolo Barone, Manuel Perez-Mato, Silvia Picozzi, and Young Sun. High-temperature ferroelectricity and strong magnetoelectric effects in a hybrid organic-inorganic perovskite framework: high-temperature ferroelectricity and strong magnetoelectric effects in a hybrid organic-inorganic perovskite framework. *physica status solidi (RRL) - Rapid Research Letters*, **9** (2015), 62–67.

[30] L. C. Gómez-Aguirre, B. Pato-Doldán, A. Stroppa, S. Yáñez-Vilar, L. Bayarjargal, B. Winkler, S. Castro-García, J. Mira, M. Sánchez-Andújar, and M. A. Señarís-Rodríguez. Room-temperature polar order in $[NH_4][Cd(HCOO)_3]$ - a hybrid inorganic–organic compound with a unique perovskite architecture. *Inorganic Chemistry*, **54** (2015), 2109–2116.

[31] Prashant Jain, Alessandro Stroppa, Dmitrii Nabok, Antigone Marino, Andrea Rubano, Domenico Paparo, Masakazu Matsubara, Heinz Nakotte, Manfred Fiebig, Silvia Picozzi, Eun Sang Choi, Anthony K Cheetham, Claudia Draxl, Naresh S Dalal, and Vivien S Zapf. Switchable electric polarization and ferroelectric domains in a metal-organic-framework. *npj Quantum Materials*, **1** (2016).

[32] A. P. Levanyuk, and Daniil G. Sannikov. Improper ferroelectrics. *Soviet Physics Uspekhi*, **17** (1974), 199–214.

[33] V. Dvořák. Improper ferroelectrics. *Ferroelectrics*, **7** (1974), 1–9.

[34] Nicole A. Benedek, and Craig J. Fennie. Hybrid improper ferroelectricity: a mechanism for controllable polarization-magnetization coupling. *Physical Review Letters*, **106** (2011), 107204.

[35] James M. Rondinelli, and Craig J. Fennie. Octahedral rotation-induced ferroelectricity in cation ordered perovskites. *Advanced Materials*, **24** (2012), 1961–1968.

[36] Nicole A. Benedek, James M. Rondinelli, Hania Djani, Philippe Ghosez, and Philip Lightfoot. Understanding ferroelectricity in layered perovskites: new ideas and insights from theory and experiments. *Dalton Transactions*, **44** (2015), 10543–10558.

[37] Hanna L. B. Boström, Mark S. Senn, and Andrew L. Goodwin. Recipes for improper ferroelectricity in molecular perovskites. *Nature Communications*, **9** (2018), 2380.

[38] Ke-Li Hu, Mohamedally Kurmoo, Zheming Wang, and Song Gao. Metal-organic perovskites: synthesis, structures, and magnetic properties of $[C(NH_2)_3][M^{II}(HCOO)_3]$ (M=Mn, Fe, Co, Ni, Cu, and Zn; $C(NH_2)_3$ = guanidinium). *Chemistry - A European Journal*, **15** (2009), 12050–12064.

[39] P. Hohenberg, and W. Kohn. Inhomogeneous electron gas. *Physical Review*, **136** (1964), B864–B871.

[40] Jorge Kohanoff. *Electronic Structure Calculations for Solids and Molecules: Theory and Computational Methods*. 1st edition. Cambridge University Press, 2006.

[41] W. Kohn, and L. J. Sham. Self-consistent equations including exchange and correlation effects. *Physical Review*, **140** (1965), A1133–A1138.

[42] D. M. Ceperley, and B. J. Alder. Ground state of the electron gas by a stochastic method. *Physical Review Letters*, **45** (1980), 566–569.

[43] John P. Perdew, Kieron Burke, and Matthias Ernzerhof. Generalized gradient approximation made simple. *Physical Review Letters*, **77** (1996), 3865–3868.

[44] S. L. Dudarev, G. A. Botton, S. Y. Savrasov, C. J. Humphreys, and A. P. Sutton. Electron-energy-loss spectra and the structural stability of nickel oxide: an LSDA+U study. *Physical Review B*, **57** (1998), 1505–1509.

[45] A. I. Liechtenstein, V. I. Anisimov, and J. Zaanen. Density-functional theory and strong interactions: orbital ordering in mott-hubbard insulators. *Physical Review B*, **52** (1995), R5467–R5470.

[46] Jochen Heyd, Gustavo E. Scuseria, and Matthias Ernzerhof. Hybrid functionals based on a screened coulomb potential. *The Journal of Chemical Physics*, **118** (2003), 8207–8215.

[47] Lev Davidovich Landau, and Evgeny Mikhailovich Lifshitz. *Statistical physics, Part 1.* 3. ed. Course of theoretical physics, Vol. 5. Amsterdam: Elsevier, 1980. 544 pages.

[48] Premi Chandra, and Peter B. Littlewood. "A landau primer for ferroelectrics". *Physics of Ferroelectrics: A Modern Perspective.* Berlin, Heidelberg: Springer, 2007. Chapter 3, 69–116 pp.

[49] J. M. Igartua, M. I. Aroyo, and J. M. Perez-Mato. Systematic search of materials with high-temperature structural phase transitions: application to space group $P2_12_12_1$. *Physical Review B*, **54** (1996), 12744–12752.

[50] Cesar Capillas, Emre Sururi Tasci, Gemma de la Flor, Danel Orobengoa, Juan Manuel Perez-Mato, and Mois Ilia Aroyo. A new computer tool at the bilbao crystallographic server to detect and characterize pseudosymmetry. *Zeitschrift für Kristallographie - Crystalline Materials*, **226** (2011), 186–196.

[51] Mildred S. Dresselhaus, Gene Dresselhaus, and Ado Jorio. *Group Theory: Application to the Physics of Condensed Matter*. Berlin, Heidelberg: Springer Berlin Heidelberg, 2008.

[52] R. D. King-Smith, and David Vanderbilt. Theory of polarization of crystalline solids. *Physical Review B*, **47** (1993), 1651–1654.

[53] Raffaele Resta, and David Vanderbilt. "Theory of polarization: a modern approach". *Physics of Ferroelectrics: A Modern Perspective*. Berlin, Heidelberg: Springer, 2007. Chapter 2, 31–68 pp.

[54] J. Zak. Berry's phase for energy bands in solids. *Physical Review Letters*, **62** (1989), 2747–2750.

[55] Kunihiro Yananose, Paolo G. Radaelli, Mario Cuoco, Jaejun Yu, and Alessandro Stroppa. Activating magnetoelectric optical properties by twisting antiferromagnetic bilayers. *Physical Review B*, **106** (2022), 184408.

[56] H.A. Jahn, and E. Teller. Stability of polyatomic molecules in degenerate electronic states-i orbital degeneracy. *Proceedings of the Royal Society of London. Series A - Mathematical and Physical Sciences*, **161** (1937), 220–235.

[57] Daniel I. Khomskii. *Transition Metal Compounds*. Cambridge Core. Cambridge University Press, 2014.

[58] John B. Goodenough. *Magnetism and the chemical bond*. Huntington, N.Y: R. E. Krieger Pub. Co, 1976. 393 pages.

[59] I. Dzyaloshinsky. A thermodynamic theory of "weak" ferromagnetism of antiferromagnetics. *Journal of Physics and Chemistry of Solids*, **4** (1958), 241–255.

[60] Tôru Moriya. Anisotropic superexchange interaction and weak ferromagnetism. *Physical Review*, **120** (1960), 91–98.

[61] G. Kresse, and J. Furthmüller. Efficient iterative schemes for *ab initio* total-energy calculations using a plane-wave basis set. *Physical Review B*, **54** (1996), 11169–11186.

[62] G. Kresse, and D. Joubert. From ultrasoft pseudopotentials to the projector augmented-wave method. *Physical Review B*, **59** (1999), 1758–1775.

[63] J.-P. Hanke, F. Freimuth, A. K. Nandy, H. Zhang, S. Blügel, and Y. Mokrousov. Role of berry phase theory for describing orbital magnetism: from magnetic heterostructures to topological orbital ferromagnets. *Physical Review B*, **94** (2016), 121114.

[64] T. Thonhauser, Davide Ceresoli, David Vanderbilt, and R. Resta. Orbital magnetization in periodic insulators. *Physical Review Letters*, **95** (2005), 137205.

[65] D. Orobengoa, C. Capillas, M. I. Aroyo, and J. M. Perez-Mato. AMPLIMODES: symmetry-mode analysis on the bilbao crystallographic server. *Journal of Applied Crystallography*, **42** (2009), 820–833.

[66] Kunihiro Yananose, Ewan R. Clark, Paul Saines, Paolo Barone, Alessandro Stroppa, and Jaejun Yu. Synthesis and magnetic properties of the hybrid perovskite $[C(NH_2)_3]Cr(HCOO)_3$: key role of spin-orbit coupling in jahn-teller distorted frameworks (). *in preparation.*

[67] N. Guiblin, D. Grebille, H. Leligny, and C. Martin. $Ca_3Mn_2O_7$. *Acta Crystallographica Section C: Crystal Structure Communications*, **58** (2002), i3–i5.

[68] R. W. Nunes, and Xavier Gonze. Berry-phase treatment of the homogeneous electric field perturbation in insulators. *Physical Review B*, **63** (2001), 155107.

[69] Patrick Bruno. Tight-binding approach to the orbital magnetic moment and magnetocrystalline anisotropy of transition-metal monolayers. *Physical Review B*, **39** (1989), 865–868.

[70] M. Blanco-Rey, J. I. Cerdá, and A. Arnau. Validity of perturbative methods to treat the spin–orbit interaction: application to magnetocrystalline anisotropy. *New Journal of Physics*, **21** (2019), 073054.

[71] H. Takayama, Klaus-Peter Bohnen, and Peter Fulde. Magnetic surface anisotropy of transition metals. *Physical Review B*, **14** (1976), 2287–2295.

[72] Alessandro Stroppa, Paolo Barone, Domenico Di Sante, Mario Cuoco, Silvia Picozzi, and Myung-Hwan Whangbo. Analogies between jahn-teller and rashba spin physics. *International Journal of Quantum Chemistry*, **116** (2016), 1442–1450.

[73] John Stanley Griffith. *The theory of transition-metal ions*. Cambridge: Cambridge University Press, 1971. 455 pages.

[74] B. T. Thole, P. Carra, F. Sette, and G. van der Laan. X-ray circular dichroism as a probe of orbital magnetization. *Physical Review Letters*, **68** (1992), 1943–1946.

[75] L. L. Tao, and Evgeny Y. Tsymbal. Persistent spin texture enforced by symmetry. *Nature Communications*, **9** (2018), 2763.

[76] T. Ozaki. Variationally optimized atomic orbitals for large-scale electronic structures. *Physical Review B*, **67** (2003). website: openmx-square.org, 155108.

[77] Hiroki Kotaka, Fumiyuki Ishii, and Mineo Saito. Rashba effect on the structure of the bi one-bilayer film: fully relativistic first-principles calculation. *Japanese Journal of Applied Physics*, **52** (2013), 035204.

[78] Roland Winkler. Inversion-asymmetry-induced spin splitting. *Spin-Orbit Coupling Effects in Two-Dimensional Electron and Hole Systems*. Edited by Roland Winkler. Springer Tracts in Modern Physics. Berlin, Heidelberg: Springer, 2003, 69–129.

[79] N. Binggeli, and M. Altarelli. Orbital ordering, jahn-teller distortion, and resonant x-ray scattering in $KCuF_3$. *Physical Review B*, **70** (2004), 085117.

[80] Yong Ai, Rong Sun, Wei-Qiang Liao, Xian-Jiang Song, Yuan-Yuan Tang, Bing-Wu Wang, Zhe-Ming Wang, Song Gao, and Ren-Gen Xiong. Unprecedented ferroelectricity and ferromagnetism in a Cr^{2+} based two-dimensional hybrid perovskite. *Angewandte Chemie International Edition*, **61** (2022).

[81] Yali Yang, Junyi Ji, Junsheng Feng, Shiyou Chen, Laurent Bellaiche, and Hongjun Xiang. Two-dimensional organic-inorganic room-temperature multiferroics. *Journal of the American Chemical Society*, **144** (2022), 14907–14914.

[82] Seungjin Kang, and Jaejun Yu. Electronic structure and magnetic properties of transition metal kagome metal-organic frameworks. *Physical Chemistry Chemical Physics*, **24** (2022), 22168–22180.

초 록

하이브리드 물질은 무기물과 유기물을 모두 구성 요소로 가지고 있기 때문에 이들 양쪽의 성질을 모두 보이며, 때로는 그 둘의 협력적인 작용을 보인다. 그렇기에 하이브리드 물질에서는 통상적인 무기물과는 구분되는 성질을 기대할 수 있다. 예를 들어, 하이브리드 유기-무기 페로브스카이트는 ABX_3 페로브스카이트 구조에서 A- 또는 X-이온이 분자 이온으로 되어있는 물질이다. 이 물질들은 태양전지 소재로 주목받고 있다. 한편, 금속-유기 골격체(Metal-Organic Framework; MOF)는 유기 링커가 금속 이온들을 서로 연결하여 이루어진 결정이다. MOF는 다공성, 층상, 페로브스카이트 등 다양한 종류의 구조를 가질 수 있다. 본 학위논문은 다강성 페로브스카이트형 MOF인 금속 구아니디늄 포메이트 $[C(NH_2)_3]M(HCOO)_3(M = Cr, Cu)$를 주로 살피고 있다. 우리는 밀도 범함수 이론에 기반을 둔 제일원리 계산으로 $[C(NH_2)_3]M(HCOO)_3$의 다강성 특성 즉, 전기 및 자기적 성질과 이들의 구조적 성질과의 상호작용을 탐구하였다. 특히, 구조적 변형을 분석하기 위해서는 군론적 방법을 이용하였다. $[C(NH_2)_3]M(HCOO)_3$는 극성 모드가 두 비극성 모드의 결합(하이브리드 모드)에 의해 유도되는 하이브리드 부적절(improper) 강유전성을 보이는 것으로 알려져 있다. 그러나 우리는 $[C(NH_2)_3]M(HCOO)_3$에서 하이브리드 모드가 순수 전자 분극을 크게 유도함을 확인하였다. 직관적인 생각과는 다르게, 극성 모드는 오히려 이런 순수 전자 분극을 상쇄한다. 우리는 이 성질에 대한 미시적인 원인과 거시적인 분석을 보인다. 한편, 우리는 $[C(NH_2)_3]Cu(HCOO)_3$의 자성에서 궤도 자기 모멘트가 주된 기여

임을 발견하였다. 우리는 섭동 이론과 얀-텔러 유효 해밀토니안을 결합하여 궤도 자기 모멘트를 설명하는 모델을 세웠으며, 이는 얀-텔러 효과의 역할을 보여준다.

주요어: 밀도범함수이론, 금속-유기 골격체, 전기분극, 자성,
얀-텔러 효과, 하이브리드 부적절 강유전성, 궤도 자성

학 번: 2016-20299